

Short Reports 2016 of IKP, Forschungszentrum Jülich.
Use bookmarks for navigation.

Further Contributions

1. Drift chamber calibration in the P-349 Antiproton Polarization Experiment
2. Analyzing power of hard bremsstrahlung $pp \rightarrow \{pp\}_s + \gamma$ in the $\Delta(1232)$ region
3. Estimation of the ANKE STT tracking efficiency from experimental data
4. Towards an upper limit for the decay $\eta \rightarrow \pi^0 e^+ e^-$ using $pd \rightarrow {}^3\text{He}\eta$ data from WASA-at-COSY
5. Hardware Development for a new Stochastic Cooling System dedicated to EDM Experiments
6. Towards a new Tune Meter for COSY
7. Studies on CP violation in the decay $\eta \rightarrow \pi^0 e^+ e^-$ in pp scattering experiments with WASA-at-COSY
8. Synchronous sampling device for the parametric current transformer
9. Analytic Model of in-Plane Depolarization and Phase Drift of the Spin Tune
10. Dalitz plot of $\eta' \rightarrow \eta\pi^+\pi^-$ using CLAS g12 data
11. Study of the electromagnetic transition form factor of the η meson with WASA-at-COSY
12. Electrostatic deflector development
13. Progress with the model development for the 2 MeV electron cooler
14. Theoretical Development of a Beam Position Independent Capacitive Quadrupole Pickup
15. Analysis of Feedback System Data
16. Lyapunov Analysis of Particle Tracking for the HESR
17. Theoretical Limits of Closed Orbit Corrections
18. Studies on η production in pd fusion to ${}^3\text{He}\eta$ with WASA-at-COSY
19. Development of a Track Reconstruction Algorithm for the Panda Forward Tracking System
20. Study of dp breakup reaction in the Forward Detector
21. A read-out system for the PANDA MVD prototypes: development and results
22. Dalitz Plot Analysis of $\eta \rightarrow \pi^+\pi^-\pi^0$ with CLAS
23. Low-noise BPM preamplifier for the HESR

24. The EDM polarimetry detector development
25. Automated Measurement of the COSY Injection Energy
26. Simulations on Ion Clearing for the HESR using COMSOL Multiphysics®
27. Reconstruction efficiency for Forward-Central coincidences
28. Amplitude estimation of a sine function based on confidence intervals and Bayes' theorem
29. Study of Excited Xi Baryons in $\bar{p}p$ -Collisions with the PANDA Detector
30. Searching for η -mesic ^3He with WASA-at-COSY facility
31. Systematic effects of orbit excursions in the spin tune mapping with solenoids
32. Simulation of closed orbit influencing effects at COSY
33. Production of eta-mesons in pn-collisions at ANKE
34. Quasi-Frozen spin concept of deuteron storage ring as an instrument to search electric dipole moment
35. Developments for the EDM polarimeter at COSY
36. Measurements of the new HESR pick-up at COSY
37. Search for η -mesic ^4He in the $dd \rightarrow ^3\text{He} n \pi^0$ and $dd \rightarrow ^3\text{He} p \pi^-$ reactions with the WASA-at-COSY facility
38. Search for box anomaly via $\eta' \rightarrow \gamma \pi^+ \pi^-$ with CLAS
39. Search for light dark bosons in η decays
40. Executive Summary of Theoretical Developments in Electron Cooling and Stochastic Cooling
41. FairMQ for the PANDA Experiment
42. Comparison of the theoretical higher order Rogowski coil BPM model with a simulation
43. Elastic $d+^{12}\text{C}$ scattering within the Glauber approach
44. Measurement of the spatial and energy loss resolution for the STT flash ADC readout for the PANDA experiment
45. Simulation for the FToF detector in Panda experiment
46. Calibration of linear optics of COSY using LOCO analysis

Drift chamber calibration in the P-349 Antiproton Polarization Experiment

Dominika Alfs*, Dieter Grzonka, Thomas Sefzick, Marcin Zieliński*
for the P349 collaboration

The goal of the P-349 experiment performed at the CERN/PS is to test whether antiprotons produced in high-energy proton-proton collisions are polarized [1], [2]. The experiment measured the elastic scattering of antiprotons, produced in interactions of 24 GeV protons with a liquid hydrogen target in the Coulomb-Nuclear interference region where the analyzing power is rather well known. The determination of the polarization requires the knowledge of the left-right asymmetry in the secondary scattering of these antiprotons for which a precise track reconstruction is needed.

The tracking in the P-349 experiment was based on a set of three drift chambers: two with rectangular cells (D1, D2) and one with hexagonal cells (HEX). In this report we present the current status of the iterative algorithm for the drift chamber calibration and the resulting position resolution for the D1 and D2 chambers. The discussed method considers only the information from one orientation of the wire planes but it can be easily extended to all wire planes orientations.

The D1 (D2) drift chamber contains eight (six) wire planes: 4 (2) with vertical wires, 2 with inclined wires at $+31^\circ$ and 2 inclined at -31° . The gas mixture consisted of Argon and CO_2 and the observed drift time range was of about 600 ns. In a first step the starting point of the drift time spectrum for each wire was determined and the spectrum was shifted by the appropriate offset (see Fig. 1 left). Drift time spectra for all wires in a certain wire plane were added and used for the determination of the initial calibration curve by the homogeneous irradiation method (see Fig. 1 right).

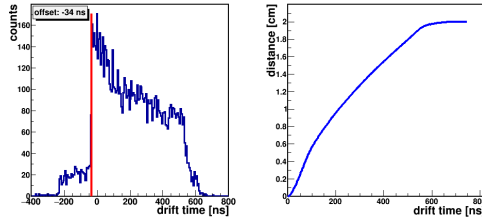


Fig. 1: *Left*: Drift time spectrum from a single wire in the D1 drift chamber. The red line indicates the start point of the spectrum. *Right*: Initial calibration curve obtained by the homogeneous irradiation method. The maximum drift time is equal to about 600 ns which corresponds to half of the drift cell width of 4 cm.

For the calibration procedure of D1 events with a clear single track signature were used, i.e. events which were registered in both START and STOP scintillators and exactly one hit in each of the vertical wire planes of D1. The wire planes are configured as double planes with the same wire orientation but shifted by half a cell width to allow for an easy resolving of the left-right ambiguity.

The calibration is an iterative procedure. At the beginning of each iteration the positions of the hits in all vertical wire planes are calculated based on the current calibration and straight tracks for all events are fitted. Track parameters (a - slope, b - constant) are determined by minimization of the sum $\sum_{i=1}^4 \frac{d_i(a,b)^2}{\sigma_i^2}$ (see Fig. 2 left) where $d_i(a,b)$ is the resid-

ual, the distance between the fitted track and hit position in the i -th wire plane and σ_i is the uncertainty of the position determination (in the first iteration all $\sigma_i = 1$). In order to extract the corrections for the calibration curves histograms of the residuals as a function of drift time are built separately for all wire planes (see Fig. 2 right) and for each time bin the calibration curve is shifted by the mean value obtained from gaussian fits to the distributions. The corrected calibration curve is used as starting point for the next iteration.

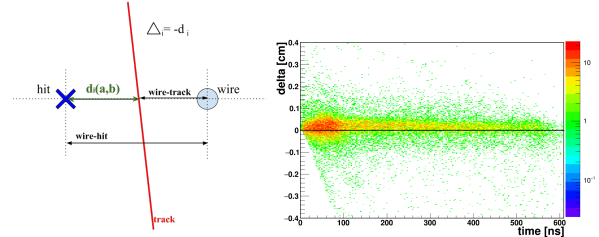


Fig. 2: *Left*: An example of the distances defined for single wire plane which are used for track fitting and Δ_i calculation. The description is given in the text. *Right*: Histogram of distances Δ_i vs. drift time.

The procedure is repeated until the corrections are below the uncertainties. The position resolution depends on the drift time range as can be seen in Fig.2. For drift times in the range of 200 - 400 ns σ -values are in the order of 200 μm . Similar results were achieved for all vertical wire planes of D1 and D2 by including hits in all these wire planes in the track fitting. Fig. 3 shows the corresponding residual distributions for the vertical wire planes of D1 and D2 after adjusting the position of D2 relative to D1.

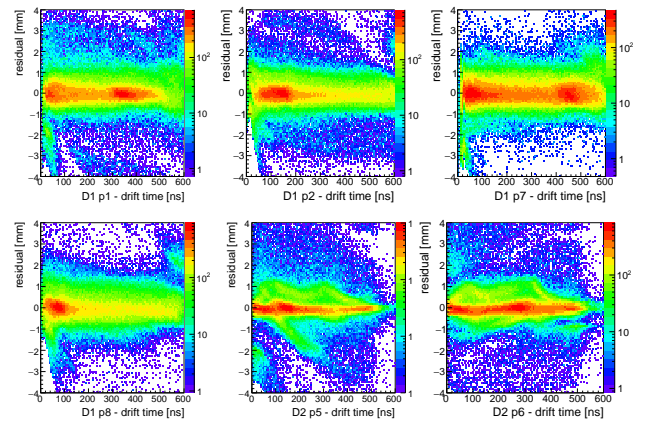


Fig. 3: Residual distribution for the vertical wire planes of D1 and D2.

The σ -values over the full drift time range are in the range of 200 - 300 μm . This results in a track reconstruction uncertainty of below 1 mrad which is consistent with the expected precision achievable for the detection setup. A further reduction of the residuals will be achieved by taking into account the drift time dependence on the track angle which is not

included up to now. In the ongoing analysis the calibration will be completed for all wire planes including the angular dependence followed by a 3D-track fitting to reconstruct the scattering events.

References:

- [1] D. Grzonka et al., Acta Phys. Pol., **B(46)** 191 (2015).
- [2] D. Alfs et al., EPJ Web Conf., **130** 07002 (2016) .

* Institute of Physics, Jagiellonian University, 30-348 Krakow, Poland

Analyzing power of hard bremsstrahlung $pp \rightarrow \{pp\}_s \gamma$ in the $\Delta(1232)$ region

B. Baimurzinova¹, D. Tsirkov¹ for the ANKE collaboration

The reaction $\gamma + \{pp\}_s \rightarrow p + p$, where diproton $\{pp\}_s$ is a proton pair in 1S_0 state, is a spin-isospin partner of the fundamental reaction of deuteron photodisintegration. The inverse reaction, the hard bremsstrahlung $p + p \rightarrow \gamma + \{pp\}_s$, has been observed with the ANKE spectrometer [1] at COSY-Jülich. In addition to differential cross section measured earlier [2, 3], in this work its analyzing power has been measured at forward angles in the region of $\Delta(1232)$ isobar excitation at beam energies $T_p = 500, 550, 700$ MeV.

Histograms for missing mass squared show a clear visible γ peak (Fig. 1) that could be separated from the pion peak associated with the $pp \rightarrow pp\pi^0$ reaction. The peak shapes were obtained by a detailed Monte Carlo simulation at each energy, which took into account all the known features of the setup. The free parameters of interest used to fit the missing-mass spectra were the number of events in the γ peak and the number of events in the pion peak. In order to compensate for the lack of knowledge of the beam spatial distribution, additional parameters were inserted into the fits: a shift of the pion peak position and correction factors for the γ and pion peak widths. The results of the fit can be seen in Fig. 1.

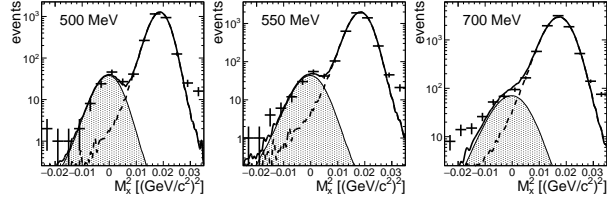


Fig. 1: Distribution of the missing mass squared in the $p + p \rightarrow \{pp\}_s + X$

We started with finding polarization asymmetry given by equation (1),

$$\varepsilon = \frac{N_{\uparrow}/L_{\uparrow} - N_{\downarrow}/L_{\downarrow}}{N_{\uparrow}/L_{\uparrow} + N_{\downarrow}/L_{\downarrow}}, \quad (1)$$

where N_{\uparrow} and N_{\downarrow} are the numbers of $\{pp\}_s \gamma$ events with beam proton spin up and down, obtained from the fit, and L_{\uparrow} and L_{\downarrow} are the corresponding luminosities. It is needed to calculate the analyzing power using equation (2),

$$A_y = \frac{\varepsilon}{P \langle \cos \phi_{pp} \rangle}, \quad (2)$$

where P is the transverse polarisation of the beam and $\langle \cos \phi_{pp} \rangle$ the average over the diproton azimuthal angular distribution. Polarization P was estimated using the known values of A_y for elastic pp and $pp \rightarrow d\pi^+$ reactions, registered in parallel with our reaction.

Different approaches were applied to obtain the analyzing power. The numbers of events can be determined either by fitting separately N_{\uparrow} and N_{\downarrow} , or directly $N_{\uparrow} - N_{\downarrow}$ and $N_{\uparrow} + N_{\downarrow}$ histograms. Concerning $\cos \phi_{pp}$ there are two possibilities, either to divide by the average value of $\cos \phi_{pp}$ distribution or to correct by $\cos \phi_{pp}$ event-by-event. Hence, four approaches were applied, each repeated for fine and gross histogram binning. These 8 values with errors were averaged. The dispersion of the values was considered as a systematic error.

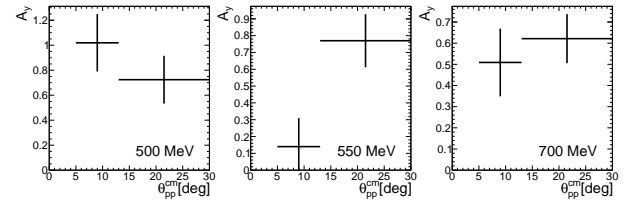


Fig. 2: Analyzing power for reaction $p + p \rightarrow \gamma + \{pp\}_s$, preliminary results.

In Fig. 2 and Table 1 the preliminary results are shown for analyzing power of the $pp \rightarrow \gamma\{pp\}_s$ reaction at $T_p = 500, 550, 700$ MeV. These results might be useful to extract additional information on the contributions of various multipoles to the reaction mechanism.

References:

- [1] S. Barsov *et al.*, Nucl. Instrum. Methods Phys. Res. **462**, 354 (2001).
- [2] V. Komarov *et al.*, Phys. Rev. Lett. **101**, 102501 (2008).
- [3] D. Tsirkov *et al.*, J. Phys. G: Nucl. Part. Phys. **37**, 105005 (2010).

¹ DLNP JINR, RU-141980 Dubna, Russia

Table 1: Numerical values of analyzing power with statistical and systematical errors, preliminary results.

	500 MeV	550 MeV	700 MeV
5°–13°	$1.02 \pm 0.22_{\text{st}} \pm 0.05_{\text{sys}}$	$0.14 \pm 0.14_{\text{st}} \pm 0.10_{\text{sys}}$	$0.51 \pm 0.15_{\text{st}} \pm 0.05_{\text{sys}}$
13°–30°	$0.72 \pm 0.18_{\text{st}} \pm 0.06_{\text{sys}}$	$0.77 \pm 0.15_{\text{st}} \pm 0.04_{\text{sys}}$	$0.62 \pm 0.11_{\text{st}} \pm 0.01_{\text{sys}}$

Estimation of the ANKE STT tracking efficiency from experimental data*

S. Barsov¹, S. Dymov³, A. Kacharava², R. Schleichert², S. Trusov² for the ANKE collaboration.

During the last decade two Silicon Tracking Telescopes (STT) designed for the detection of low energetic particles have been successfully exploited as a polarimeter in several experiments carried out by the ANKE and the PAX collaborations. In contrast to this application, the use of STTs as the detector of “spectator” protons in experiments aimed to study a process in the quasi-free kinematics requires more accurate quantitative understanding of the STT acceptance.

Results presented below were obtained from experimental data taken at ANKE using the proton beam and the deuterium cluster target. Two STTs were installed at 3cm distance to the left and to the right from the beam axis. The self-trigger from STT detectors was used to record the data. Since each STT consists of 3 position-sensitive (segmented) detectors, the self-triggering option allows to reconstruct the track in one STT using information from 2 detectors only, one of which must be the detector generating the self-trigger signal. This one was recognized from the time information recorded in the TDC. Finally, events with 1 track reconstructed per one pair of detectors were selected and used in further analysis.

Now, the efficiency of detector which was not involved into the track reconstruction can be investigated if one makes sure that the reconstructed track hits this detector. The last requirement is automatically fulfilled when the track is produced by a particle stopped in the last 3d (5mm thick) detector of STT. Moreover, in this case the expected energy loss in the 1st (70 μm thick) or in the 2nd (300 μm thick) detectors can be calculated as well as the expected position of the track intersection point. However, to be sure that the selected track hits the 3d detector, energy losses in the 1st and in the 2nd detectors have to be limited within such intervals where the particle identification is not possible.

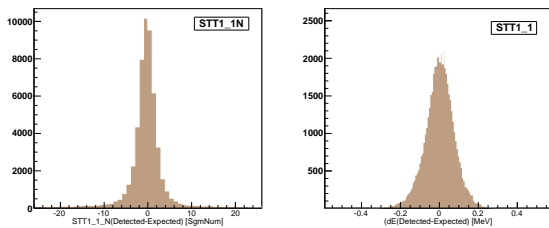


Fig. 1: Distributions of positions (left panel) and energy losses (right panel) of clusters found in the 1st detector of STT1 with respect to the intersection position and expected energy loss calculated for tracks reconstructed using the 2nd and the 3d detectors.

The accuracy of calculated intersection point position and the expected energy loss was verified by the comparison with positions and energy losses of clusters found in the detector under test in the same event. All distributions of differences between calculated and corresponding measured values were found to be similar to ones presented in Fig. 1. The uncertainty of intersection point calculation in other detectors is smaller because the distance between the 2nd and the 3d detectors is about 10mm while it is about 20mm between the 1st and the 2nd ones. However, the FWHM of similar position difference distributions were not less than 2.5 segments, anyway. Therefore, the detector under test was considered to be effective when the appropriate cluster was found within some area in vicinity of the calculated intersection point. This area

have been chosen for each detector from distributions similar to ones shown in Fig. 1.

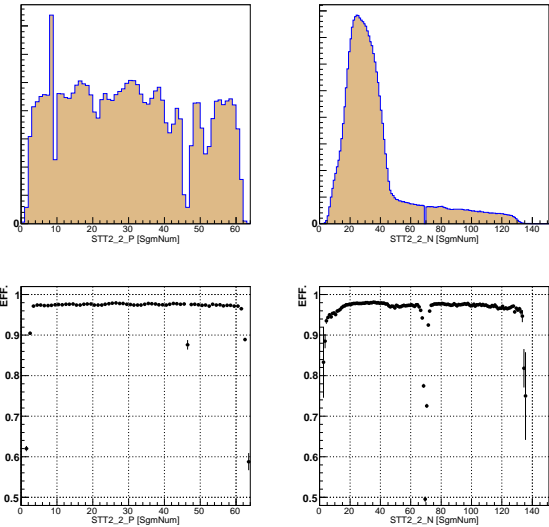


Fig. 2: Distributions of clusters found in the 2nd detector of STT2 along segments on different surfaces are shown in upper panels. Segments on the N-side are vertical while on the P-side they goes along the beam direction. Efficiency distributions along the detector surfaces are presented in lower panels. Note that the efficiency determined for one segment in the P-side (or in the N-side) is integrated over all segments on the opposite detector surface. In addition, the efficiency is integrated over total available energy loss range.

Despite the efficiency defined in such manner is convoluted over several neighboring segments, it is not crucial for the analysis of a process measured in quasi-free kinematics when the efficiency is smoothly changing over detector acceptance. As one can see from Fig. 2, the efficiency of properly operating detector remains nearly constant even when the count rate is strongly varying across the acceptance. However, near detector edges and in vicinity of broken segments the efficiency turns to be underestimated. In the simple case when one broken segment is surrounded by fully operating ones (see, for example, the segment 69 in the right column of Fig. 2) the efficiency of neighboring segments can be partially corrected taking into account that the broken segment must not respond. Excluding segments near detector edges and non-working segments, average efficiencies of 2nd and 3d detectors in both the STTs were found to be about 97%. However, efficiencies of the 1st (70 μm thick) detectors, where the dE-range below 1 MeV could be only tested with particles stopped in the 3d detector, did not exceed 87%. In summary, the procedure which can be used as an effective tool for an estimation of the STT acceptance performance was developed though some improvement is still required to investigate the efficiency of the 1st detectors.

- 1 PNPI, 188350 Gatchina, Russia
- 2 IKP, FZ Jülich, 52425 Jülich, Germany
- 3 JINR, 141980 Dubna, Russia

* supported by COSY-FFE

Towards an upper limit for the decay $\eta \rightarrow \pi^0 e^+ e^-$ using $pd \rightarrow {}^3\text{He} \eta$ data from WASA-at-COSY*

F. Bergmann[†], K. Demmich[†], N. Hüsken[†] and A. Khoukaz[†]

The η meson decay $\eta \rightarrow \pi^0 e^+ e^-$ is well suited for the search for a C parity violation in the electromagnetic interaction. While the C parity is conserved in the decay process $\eta \rightarrow \pi^0 \gamma^* \gamma^* \rightarrow \pi^0 e^+ e^-$, it is violated in the reaction $\eta \rightarrow \pi^0 \gamma^* \rightarrow \pi^0 e^+ e^-$. According to theoretical calculations the C conserving process via two virtual photons has an expected branching ratio in the range of 10^{-11} to 10^{-8} [1]. Since the current upper limit for the branching ratio of the decay $\eta \rightarrow \pi^0 e^+ e^-$ is 4×10^{-5} [2], there are three orders of magnitude room to search for a possible C violating decay. The analysis presented in this report is based on data collected in 2008 and 2009 at WASA-at-COSY using the reaction $pd \rightarrow {}^3\text{He} \eta$. Here, approximately 3×10^7 η events have been recorded. In a first analysis step the data were preselected on a ${}^3\text{He}$ nucleus detected in the WASA forward detector and the signature of the decay of interest, namely at least two neutral particles, one positively charged and one negatively charged particle detected in the WASA central detector. Furthermore, cuts to reject electrons and positrons from conversion at the COSY beam pipe and split off events were applied. Afterwards the preselected data were fitted by a complete cocktail of Monte Carlo simulations including contributions from random coincidences. Fig. 1 shows an example fit for the invariant mass of two neutral particles and two oppositely charged particles assuming an electron mass for the charged particles. The prominent peak at about $420 \text{ MeV } c^{-2}$ originates from the decay $\eta \rightarrow \pi^+ \pi^-$ ($\pi^0 \rightarrow \gamma \gamma$). Due to the wrongly assumed mass of the charged particles the peak is shifted to a mass below the η mass.

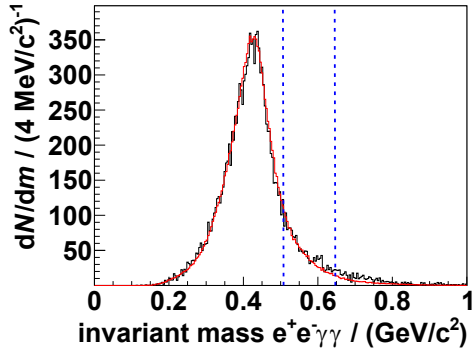


Figure 1: Invariant mass of $e^+e^-\gamma\gamma$ for the angular range $0.2 < \cos \vartheta_{\text{cms}}^{\text{He}} \leq 0.4$. The data sample from the 2008 beam time is shown in black, and the fit using Monte Carlo simulations is shown in red. The selection condition used in the analysis are indicated by blue dashed lines. Adapted from [3].

The information about the contributions of the various reactions to the data obtained by the Monte Carlo cocktail fit were used for the optimization of selection conditions for the decay $\eta \rightarrow (\pi^0 \rightarrow \gamma \gamma) e^+ e^-$. For the event selection various quantities were used: The ${}^3\text{He}$ missing mass, the invari-

ant mass of $e^+e^-\gamma\gamma$, the invariant mass of $\gamma\gamma$, the invariant mass of e^+e^- , the χ^2 probability of a kinematic fit with the hypothesis $pd \rightarrow {}^3\text{He} \gamma \gamma e^+ e^-$, and a cut for the e^+e^- identification based on the momenta and energy losses. The selection conditions for these quantities were optimized by an algorithm purely based on Monte Carlo simulations of the signal decay and all simulated background reactions scaled according to the fit to the measured data. This algorithm maximizes the signal efficiency while suppressing events from background reactions. As an example for the event selection the cut obtained for the invariant mass of two photons and two oppositely charged particles is indicated by blue dashed lines in Fig. 1.

After all selection conditions were applied there are 3 events left in the combined 2008 and 2009 data sets. According to Monte Carlo simulations about 2 events are expected to remain. Fig. 2 shows the ${}^3\text{He}$ missing mass for the data and weighted Monte Carlo simulations after all cuts.

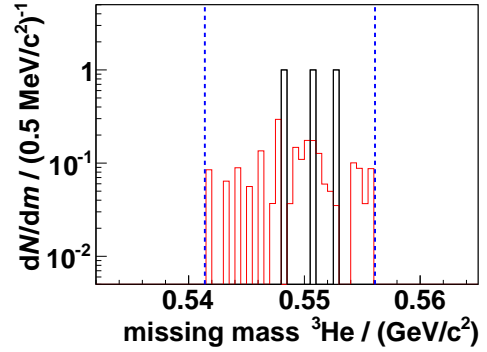


Figure 2: ${}^3\text{He}$ missing mass for the data collected in 2008 and 2009 (black) and for Monte Carlo simulations (red) [3]. The selection conditions utilized in the analysis are indicated by blue dashed lines.

The efficiency for the signal decay depends on the decay process. For a decay according to three-particle phase space an efficiency of $\varepsilon_S^{\text{phase}} = 1.84\%$ was determined, while the efficiency for a decay via one virtual photon is $\varepsilon_S^{\text{virtual}} = 2.4\%$. In order to determine an upper limit for the branching ratio, the decay channel $\eta \rightarrow \pi^+ \pi^-$ ($\pi^0 \rightarrow \gamma \gamma$) is used for normalization. According to the MC fit there were about 6.5×10^6 events of this reaction in data after efficiency correction.

For a final upper limit determination all uncertainties of the experiment and the analysis need to be considered, which is currently in process. However, it is expected that a new upper limit for the branching ratio of the decay $\eta \rightarrow \pi^0 e^+ e^-$ will be obtained, which is about one order of magnitude below the current upper limit.

References

- [1] C. Jarlskog and E. Shabalin, Phys. Scripta **T99**, 23-33 (2002).
- [2] M.R. Jane *et al.*, Phys. Lett. B **59**, 99-102 (1975).
- [3] F.S. Bergmann, PhD thesis in preparation (2017).

*Supported by COSY-FFE

[†]Institut für Kernphysik Westfälische Wilhelms-Universität, 48149 Münster, Germany

Hardware Development for a new Stochastic Cooling System dedicated to EDM Experiments

B. Breikreutz, N. Shurkhno, R. Stassen, H. Stockhorst

Introduction

One of the main users of the COSY facility nowadays is the JEDI (Jülich Electric Dipole moment Investigations) collaboration. The accelerator is used to store polarized deuteron beams at comparatively low momentum of 970 MeV/c [1]. A long beam lifetime and small momentum spread are crucial to examine the spin coherence time. Therefore, beam cooling is considered. COSY provides two electron coolers as well as a stochastic cooling (SC) system. The 100 kV electron cooler is already used for low energy polarized beams. Unfortunately, the existing stochastic cooling system is not sensitive to slow particles. Therefore, an additional stochastic cooling system dedicated to EDM (electrostatic dipole moment) experiments was considered. Hardware was optimized for the given energy by numeric field simulations, and the expected system performance was calculated. It was found out that a low energy SC system could be implemented with off-the-shelf RF-equipment, and thus at low cost.

Hardware positioning

In the past, COSY was equipped with a SC system consisting of four tanks. The horizontal pickup (PU) was positioned at the beginning of the first telescope and the vertical pickup at its end. The kickers (KI) were placed at the second telescope accordingly (Fig. 1).

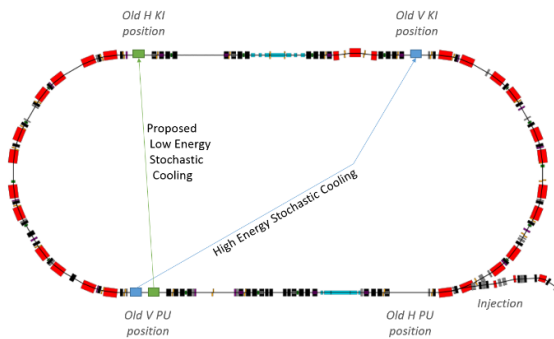


Fig. 1. Floor plan of COSY with the favored location for the new SC system.

The old vertical system was replaced by the new HESR high energy system for testing purposes. It combines all three planes (horizontal, vertical, and longitudinal) in one tank, therefore the old horizontal system becomes obsolete as well and makes space for the new system. Unfortunately, the aperture at the position of the old horizontal PU is crucial, since it is located directly behind the point of injection. We prefer a device with a small aperture because this leads to a much higher sensitivity. Therefore, we consider to place the new PU next to the HESR PU. It is much shorter than the old device, leaving sufficient space for a second tank. The new KI can stay at the position of the old horizontal KI. Then the phase advance between PU and KI is almost the same, since the telescopes are one-to-one projectors. The reduced distance between the devices and the low velocity of the particles roughly cancel out, so the time available for signal processing stays almost the same as well.

Frequency Band

The initial momentum spread of the deuterons is assumed to be about $2 \cdot 10^{-4}$, with a frequency slip factor of $\eta=0.6$. This results in a band overlap of the Schottky bands at frequencies above approximately 1 GHz. Since separated bands are needed to tune the system, the used frequency band should stop below this frequency. Furthermore, the high frequency of the old system is the main reason for its low sensitivity for slow particles. Therefore, a range of 400 to 800 MHz was chosen.

PU / KI type

Many different concepts are used for high frequency pickups and kickers for stochastic cooling. For HESR a new type, consisting of a stack of slot-rings, was developed [2]. It unites different advantages. It has a static aperture instead of movable electrodes, which simplifies the operation and reduces possible error sources. All three planes are cooled at the same time in one single device with a reasonable performance. Furthermore, since it was developed in-house and built by ZEA, we have some experience with its properties. Therefore, it was decided to take the HESR hardware as a basis and optimize it for low frequencies and particle velocities.

Achievable Sensitivity

In a first step, three major features of the HESR unit cell have been parametrized, i.e. the slot width, the cell height, and the width of the gap to the beam pipe. Those parameters have been optimized regarding the longitudinal shunt impedance of the kicker. A geometry with a considerably high impedance and a symmetric course was found (Fig. 2):

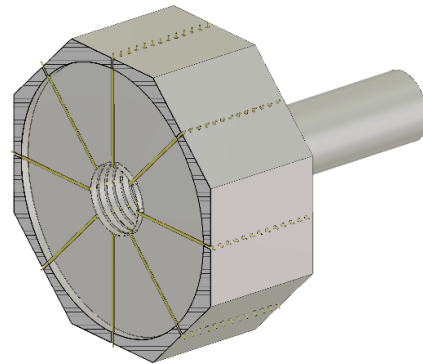


Fig. 2. Optimization result for an eight-electrode kicker in CST Microwave Studio. The structure is cut across one cell, between the stripline electrodes and the base plate of the next cell. The beam axis is along the center perpendicular to the cells.

Due to the low frequencies, a much larger slot width (115 mm) compared to the HESR kicker (13 mm) is needed to tune the cell to the desired frequency. A small cell height is beneficial, but very slim cells should be avoided because of the electrodes. Furthermore, a combiner board gets much more complicated if the

number of cells exceeds a reasonable amount. A height of 10 mm was chosen as a compromise. The gap width turned out not to be very sensitive at all and was therefore kept at 4 mm. The resulting impedance can be found in Fig. 3 (blue graph).

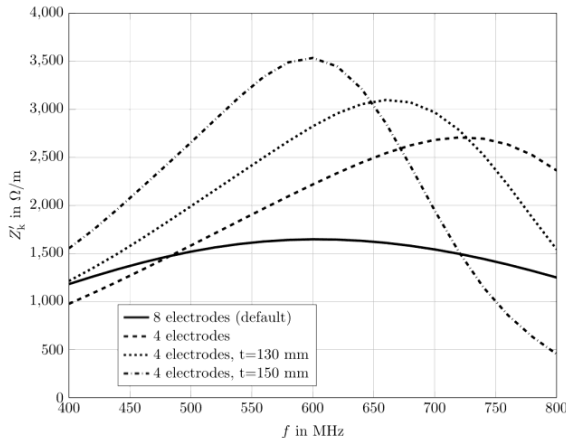


Fig. 3: Longitudinal shunt impedance of the eight-electrode kicker from Fig. 2. In comparison, the results for four-electrode structures of different slot width.

Next, the number of electrodes was varied. Although four electrodes per cell are sufficient to measure the two transverse planes separately, the HESR kicker has been designed with eight electrodes to increase its bandwidth. According to Fig. 3, a structure with four electrodes but the same geometry as an optimized eight electrode structure has better properties for most of the frequency band. With some minor optimization, a solution was found that performs better in the whole bandwidth.

Transverse Impedance

Since the optimization was done only regarding the longitudinal shunt impedance, the transverse performance had to be checked afterwards. With approximately 2.5 k Ω per meter of structure length, the transverse shunt impedance should be sufficiently large as well. A variation of the parameters showed that the points of optimum longitudinal and transverse impedance are not the same, consequently one may sacrifice some longitudinal impedance to increase the transverse one.

Mechanical considerations

Although the new design is similar to the one of the HESR structures, new challenges occurred to the constructors, simply because of the far bigger size. The single cell cannot be clamped any more for milling, but must be fixated on a vacuum table. Furthermore, the stiffness of the base plates is much smaller, probably leading to a deformation of the cells. Simulations showed

that an increase of the thickness of the plate and the collar decrease the impedance only by a few percent, thus this problem will be faced with a thickness of 2 mm instead of 1 mm, and the tolerances will be softened in a reasonable range. Since the electrodes are very long as well and may skew, a sleeve in the coaxial outlet is foreseen to center the electrode.

Anticipated cooling performance

Pick-up and kicker impedances have different impacts on cooling performance. Pick-up impedance determines the system initial signal-to-noise ratio and eventually the final momentum spread or betatron oscillations amplitudes. For EDM it is favorable to have the smallest possible beam. Simulations show that pick-up length of 1 m provides sufficient sensitivity while emittances and momentum spread could be reduced by at least ten times, which seems good enough. The overall kicker impedance determines the required amplifier power for cooling. Due to narrow bandwidth and relatively small intensities the needed power is quite low, and the 0.5 m length kicker requires less than 1 W input power for optimum gain (filter cooling), which is around 120 dB. Thus, even considering a big safety margin, a simple 10 W amplifier should be enough for optimum cooling performance. This is very beneficial for the total cost of the system since such amplifiers are very common. In other SC systems, a large part of the budget is used for the high-power amplifiers.

The cooling time (to achieve 2.7 times reduction) for optimum gain is an order of 10 s for both transverse and longitudinal systems.

The frequency response behavior of the pick-up and kicker shunt impedances seems to have minor effects on cooling performance, thus structure with four electrodes (Fig. 3) is advantageous.

Outlook

The simulations show good performance for stochastic cooling of 970 MeV/c beam at COSY with the new developed pick-up and kicker, while technical requirements are easily feasible. This turns the project to the next step – prototype development and construction.

References

- [1] Z. Bagdasarian et al., Measuring the polarization of a rapidly precessing deuteron beam, Physical Review Special Topics - Accelerators and Beams 17, 2014
- [2] R. Stassen et al., COSY as ideal Test Facility for HESR RF and Stochastic Cooling Hardware, 23th Particle Accelerator Conference, 2009

Towards a new Tune Meter for COSY

B. Breitzkreutz, C. Böhme, V. Kamerdzhev, R. Stassen

Introduction

One of the most important operational parameters of a synchrotron is its working point i.e. the tune. The particles perform betatron oscillations around the ideal orbit in the horizontal and vertical plane. The number of oscillations per revolution is called the tune of the machine. For machine operation, it is crucial to measure the tune with a sufficiently high precision, because a poorly tuned machine may lead to resonant behavior of the betatron oscillations followed by the beam blow up and eventually beam loss.

This paper presents ongoing development of a new, automated, and integrated tune measurement system for COSY.

Current System

Today, the tune of COSY is measured with a network analyzer (NA). The output of the NA is connected to the amplifiers of a transverse beam exciter – the stripline unit [1]. The two inputs of the NA are fed with the horizontal and vertical difference signals from a beam position monitor (BPM). During the frequency sweep, the beam particles experience transverse kicks increasing the amplitude of the betatron oscillation. The BPM measures those beam oscillations, and the tune can simply be read from the position of the peak on the NA in relation to the revolution frequency.

This method is very robust due to its simplicity, but lacks some important features. First, it is not applicable during the acceleration ramp. This is because the revolution frequency changes continuously, therefore the tune cannot be calculated from the betatron frequency. Second, the sweep time must be long enough for sufficient excitation, therefore the measurement time is roughly 0.3 seconds. Third, the system has no logging capabilities.

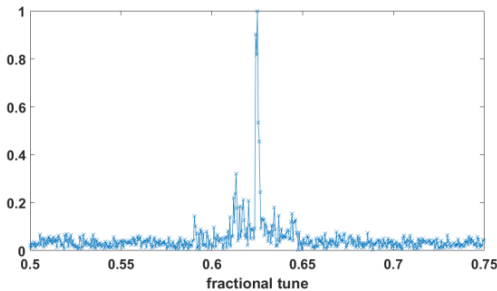


Fig. 1: FFT of a test measurement at COSY of the y-Position of a bunched beam for 1024 revolutions, as provided by a Libera Hadron BPM system.

Dynamic Tune Measurement

In the past, a system for dynamic tune measurement was additionally installed at COSY [2]. It could measure the tune during the acceleration ramps. A noise source did the beam excitation, all frequencies in the desired band at the same time. A specially developed system with a phase locked loop (PLL) recorded the position of the bunch at each revolution, therefore the coherent bunch oscillation could be analyzed. Unfortunately, the dynamic tune meter has reached end of life and is not available for the measurements.

A new Tune Meter

To overcome the drawbacks of the system still in use, a software is in development that is capable to measure the tune of coasting beams as well as beams during the acceleration ramp, perform measurements in short time, and to write the results to a permanent log.

The beam excitation is performed with the same noise source that was used for dynamic tune measurement in the past.

The tune of the coasting beam will be measured with two spectrum analyzers connected to a BPM, one for each plane. Due to the noise excitation, the whole band is excited at once, leading to shorter measurement times than with a network analyzer.

The measurement of a bunched beam will be performed with the new Libera Hadron devices from Instrumentation Technologies. They perform a digital signal processing of the BPM data. The single bunches are automatically recognized, and their positions computed. Furthermore, an internal FPGA calculates the frequency spectrum on the fly, and therefore directly provides the tune (see Fig. 1).

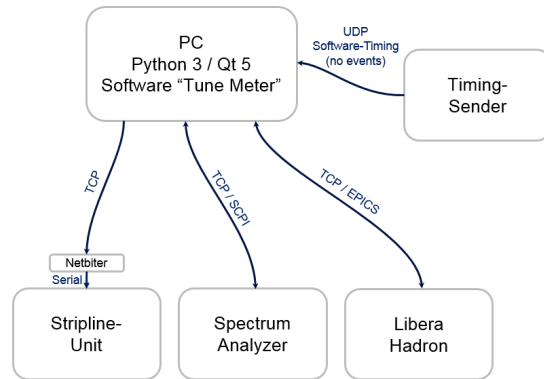


Fig. 2: Hardware setup for the automatic tune measurement system.

A diagram of the measurement system is shown in figure 2. The application is implemented in Python 3 and has a graphical user interface written in Qt. The spectrum analyzers are read out via SCPI over a TCP connection. The EPICS server of the Libera Hadron is used to read out the bunched beam spectra.

The timing will not be event driven. Instead, the Tune Meter listens to the time in cycle via a UDP service of the timing sender, and the points of time for the single measurements are defined in the software. This reduces the number of events that must be defined to trigger the single instruments.

References

- [1] J. Bojowald et al., Stripline Unit, JÜL-2590, 1992
- [2] J. Dietrich, I. Mohos, Real-Time Betatron Tune Measurement in the Acceleration Ramp at COSY-Jülich, Proceedings DIPAC, 1999

The Lagrangian densities of the QED and of the QCD are invariant under charge symmetry operations. Consequently, the C -parity is expected to be conserved in electromagnetic and strong processes, e.g. in electromagnetic meson decays, and in fact no violation has been observed in experiments so far. The electromagnetic decay of the pseudoscalar η -meson $\eta \rightarrow \pi^0 e^+ e^-$ is a very good candidate to further test the C -parity conservation and even gives access to physics beyond the standard model. The decay with one virtual photon as an intermediate particle would violate the C -parity and is therefore forbidden within the standard model, whereas the allowed process via two virtual photons is expected to have a relative branching ratio between 10^{-11} and 10^{-8} [1]. The decay has not been observed yet and the current experimental upper limit for the relative branching ratio of 5×10^{-4} [2] gives room of several orders of magnitude to search for C -violating processes like non-standard particles in intermediate states.

The high statistic data set collected with WASA-at-COSY in a large η -production campaign using proton-proton-scattering allows for studies on such rare and forbidden η -decays in exclusive measurements. The search for a very rare decay relies on the good understanding of the data composition based on all contributing processes (other η -decays as well as (multi-)pion-productions) and an efficient background suppression. An important tool to identify the η -production and to distinguish it from (multi-)pion-productions are cuts on the missing mass of the protons. A high signal-to-background ratio can only be achieved with a high missing mass resolution and an accurate detector calibration. For that purpose, the peak position of the missing mass was corrected de-

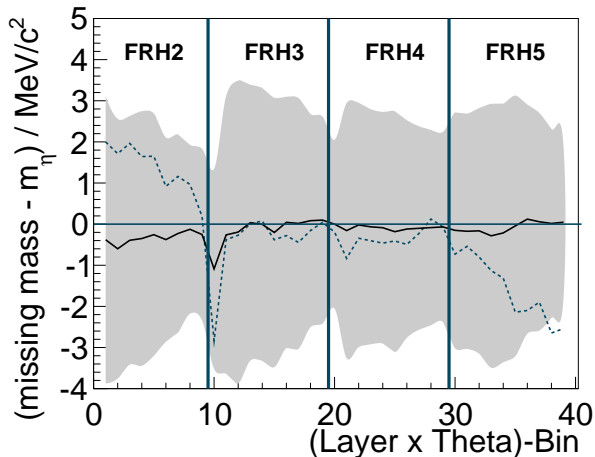


Figure 1: Deviation of the missing mass peak position from the η -mass depending on stopping plane and scattering angle before (dashed line) and after the correction (solid line). The shaded area denotes the standard deviation of the missing mass after the correction.

pending on the polar angle ϑ , the deposited energy E_{dep} , and the last reached detector layer of each proton. In order to suppress the multi-pion-background, six photons are demanded in the central detector originating from $\eta \rightarrow 3\pi^0$. As shown in fig. 1 deviations of up to 2 MeV have to be corrected for. Fig. 2 compares the missing mass spectra before and after this correction showing a resulting resolution of $\sigma \approx 2.5$ MeV being among the best missing mass resolutions ever achieved with WASA.

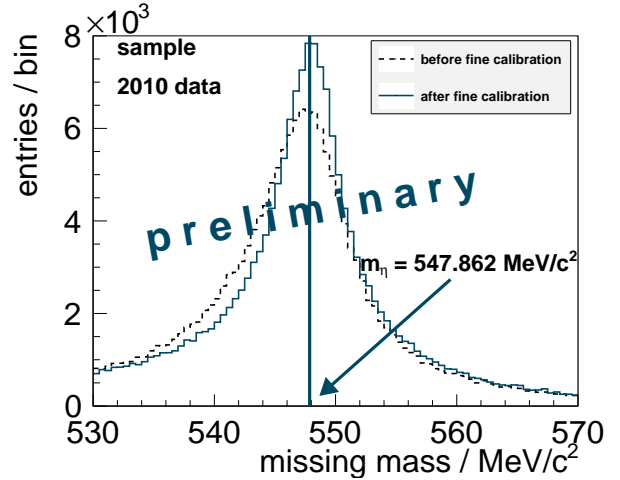


Figure 2: Comparison of the missing mass distribution before (dashed) and after (solid line) the correction revealing a significant improvement of the resolution.

One limitation for the achievable missing mass resolution are interactions between COSY beam particles and residual gas molecules in the interaction chamber resulting in vertices distributed around the nominal interaction point. This distribution has to be determined and reproduced by simulations. Moreover, the energy resolution (smearing parameters) of the individual detector planes has to be adjusted in simulation to reproduce the observed missing mass resolution in data.

After applying all these adjustments, the measured missing mass spectrum just after basic selection conditions can be fitted by a cocktail of simulated reactions including (multi-)pion- and η -production with several decay modes. This simulations will be the base for the upcoming cut optimizations and efficiency determinations. The recent status of the analysis already promises a higher sensitivity for the decay of interest compared to the current upper limit.

References

- [1] C. Jarlskog and E. Shabalin, Phys. Scripta **T99**, 23-33 (2002)
- [2] M. R. Jane *et al.*, Phys. Lett. B **59**, 99 (1975)

*Supported by COSY-FFE.

Synchronous Sampling Device for the Parametric Current Transformer

Leonid Eltcov, Sergey Mikirtychiants, and Yuri Valdau

Beam current is one of the main parameters of any particle accelerator. Principle of operation of commonly used non-intercepting beam current sensors (current transformers) is based on detection of electromagnetic field produced by the charged moving particles [1]. In case of continuous beam stored in the accelerator very low constant magnetic field has to be measured (e.g. magnetic field carried by 1 mA beam in 10 cm distance is about 1 nT while the Earth magnetic field, for comparison, is as large as 50 μ T). Such a small magnetic fields can be measured using so-called fluxgate magnetometer, operation principle of this device is well-known and can be found in Refs. [1, 2]. These devices are widely used for small (up to 10 pT) magnetic fields measurements (instead of Hall and MR sensors) in different fields of science and technology [3, 4].

The Parametric "Current Transformer" (PCT) from Bergoz Instrumentation, installed at COSY, belongs to such type of magnetometers. Its construction consists of two modulation cores and feedback current loop [1]. Despite of all the advantages of the device, a small difference in magnetic properties of two cores leads to undesirable AC component in the feedback current loop and, therefore, in the output signal. Such a ripple with the excitation frequency of 7 kHz can be easily dumped by an analogue filter, which, of course, will decrease band width of the output signal.

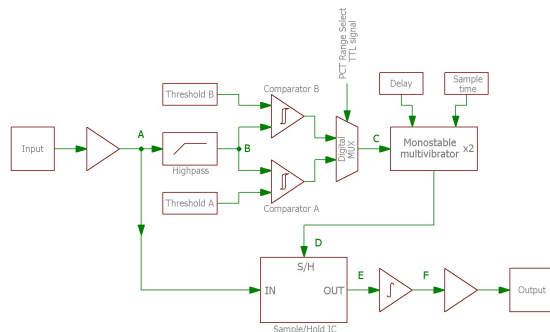


Fig. 1: Block diagram of the synchronous sampling device installed at COSY PCT.

Alternative method to extract DC component from PCT output signal is to read this signal in-phase with excitation frequency. Block diagram of a synchronous sampling system, designed and build to improve PCT performance, is presented in Fig. 1. Locked digital signal for sampling system is generated from the "Full Bandwidth" signal of the current transformer using a high pass filter, to extract the AC component of the signal, which is later fed into a logical comparator. Since amplitude of the ripple in the PCT output signal can differ depending on PCT operation range (0-10 mA or 0-100 mA) two different comparators have been used. Switching between comparators is done using digital multiplexer controlled by the TTL signal generated in PCT electronics to switch operation range. Falling edge of the comparator signal starts the first of two monostable timers connected in serial. The first timer is allows to set sampling delay (0-140 μ s), while the second one is used to set sampling gate

(8-22 μ s), necessary to charge the hold capacitor inside the sampling and hold (SH) chip. This timing scheme drives SH chip which synchronously reads the PCT output signal and holds the value until next period. Phase shift for the output signal can be adjusted using trimmer. On the final stage, ripple from the sample and hold chip is smoothed with a simple RC circuit.

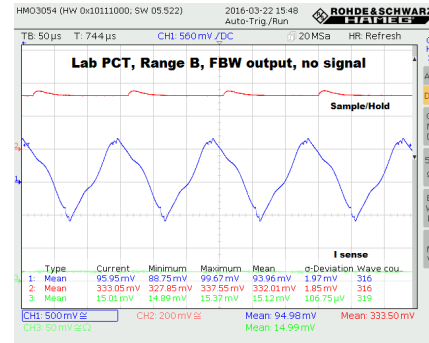


Fig. 2: Laboratory PCT "Full Bandwidth" output waveform (blue) and signal obtained from synchronous sampling device (red).

Due to minor differences between current transformers at COSY and in the laboratory two different devices have been produced. Waveforms obtained with the lab PCT are shown on the Fig. 2. Attenuation of -33 dB for the PCT modulator ripple can be reached using constructed sample and hold system without additional limitations on the output signal bandwidth. Similar kind of attenuation can be reached with the help of first or second order low pass filters with cut off frequencies of 160 and 400 Hz, respectively.

References:

- [1] P. Forck, "Lecture Notes on Beam Instrumentation and Diagnostics", 2011, available via http://www-bd.gsi.de/conf/juas/juas_script.pdf
- [2] K. Oyama and C. Cheng, "An Introduction to Space Instrumentation", (2013), available via <http://www.terrapub.co.jp/onlineproceedings/ste/aisi/>
- [3] G. Musmann and Yu. Afanassiev, "Fluxgate Magnetometers for Space Research", 2010.
- [4] W. Telford et al., "Applied Geophysics", Cambridge University Press (1990).

Analytic Model of in-Plane Depolarization and Phase Drift of the Spin Tune

D. Eversmann^a, Joerg Pretz^b

In this report an analytic model of the in-plane depolarization process of the spin ensemble and the corresponding phase drift is discussed. Therefore, a turn discrete Fourier transform of the events detected in the EDDA polarimeter is performed. Furthermore, the probability density functions of the amplitude ε and phase φ are identified based on the estimated ones $\tilde{\varepsilon}$ and $\tilde{\varphi}$.

Given the beam momentum of $p_d = 0.97 \text{ GeV}/c$ the bunch frequency yields approximately $f_b \approx 750 \text{ kHz}$. This corresponds to a spin precession frequency of

$$f_{v_s} = v_s f_b = \gamma G_d f_b \approx 120 \text{ kHz}, \quad (1)$$

where $\gamma = 1.125$ is the relativistic Lorentz factor and $G_d \approx -0.143$ denotes the anomalous magnetic moment of deuteron. The relation $v_s = \gamma G$ is only valid for a particle on the reference orbit circulating in horizontal plane of a pure magnetic ring.

Amplitude and Phase Estimation In 2015 a method was presented to determine the spin tune phase with high precision [1]. In the following, a more sophisticated technique is discussed in order to estimate the phase of the spin ensemble and its amplitude.

The turn discrete Fourier transform provides one amplitude respectively one phase estimator for each macroscopic turn interval of $\Delta n = 4 \times 10^6$ turns ($\approx 5.3 \text{ s}$)

$$\tilde{\varepsilon} = \frac{1}{N_{\text{ev}}} \sqrt{\tilde{a}^2 + \tilde{b}^2}, \quad \tilde{\varphi} = \arctan\left(\frac{\tilde{b}}{\tilde{a}}\right), \quad (2)$$

with $\tilde{\varepsilon} \in (0, 1]$ and $\tilde{\varphi} \in (0, 2\pi]$. The Fourier coefficients are given by the summation over all detected events N_{ev} within Δn

$$\tilde{a} = \sum_{i=1}^{N_{\text{ev}}} \cos(2\pi v_s n_{\text{ev}}^i), \quad \tilde{b} = \sum_{i=1}^{N_{\text{ev}}} -\sin(2\pi v_s n_{\text{ev}}^i), \quad (3)$$

where n_{ev}^i denotes the turn number of event $i \in [1, N_{\text{ev}}]$.

For a large number of events the estimators of the Fourier coefficients are Normal distributed random variables with mean μ_a, μ_b and standard deviation $\sigma_a = \sigma_b = \sigma = 1/(\sqrt{2}N_{\text{ev}})$. It can be shown that the joint bivariate probability density function (PDF) of the estimated amplitude and phase yields

$$p_{\tilde{\varepsilon}, \tilde{\varphi}}(\tilde{\varepsilon}, \tilde{\varphi} | \varepsilon, \varphi) = \frac{\tilde{\varepsilon}}{2\pi\sigma^2} e^{-\frac{\tilde{\varepsilon}^2 + \varepsilon^2}{2\sigma^2}} \cdot e^{-\frac{2\tilde{\varepsilon}\varepsilon \cos(\Delta\varphi)}{2\sigma^2}}, \quad (4)$$

where the difference between the estimated and the true phase is given by $\Delta\varphi = \varphi - \tilde{\varphi}$. This indicates that the PDF is invariant (symmetric) under the transformation $\varphi \rightarrow \tilde{\varphi}$.

For further analysis it is of fundamental interest to identify the PDF of the true values based on the estimated ones. Defining the variables $\tilde{\xi} = \tilde{\varepsilon}/\sigma$ respectively $\xi = \varepsilon/\sigma$ and

making use of the Bayes' theorem leads to the bivariate PDF of the true variables

$$\begin{aligned} p_{\varepsilon, \varphi}(\xi, \varphi | \tilde{\xi}, \tilde{\varphi}) &= \frac{p_{\tilde{\varepsilon}, \tilde{\varphi}}(\tilde{\xi}, \tilde{\varphi} | \xi, \varphi) p(\xi) p(\varphi)}{p(\tilde{\xi}) p(\tilde{\varphi})} \\ &= \frac{p_{\tilde{\varepsilon}, \tilde{\varphi}}(\tilde{\xi}, \tilde{\varphi} | \xi, \varphi) p_{\varepsilon}(\xi | \tilde{\xi})}{p_{\tilde{\varepsilon}}(\tilde{\xi} | \xi)}, \end{aligned} \quad (5)$$

with the constant priors $p(\xi)$ and $p(\varphi)$. Here the univariate Bayes probabilities

$$\frac{p_{\varepsilon}(\xi | \tilde{\xi})}{p_{\tilde{\varepsilon}}(\tilde{\xi} | \xi)} = \frac{p(\xi)}{p(\tilde{\xi})}, \quad \text{and} \quad \frac{p_{\varphi}(\varphi | \tilde{\varphi})}{p_{\tilde{\varphi}}(\tilde{\varphi} | \varphi)} = \frac{p(\varphi)}{p(\tilde{\varphi})} = 1, \quad (6)$$

are used. The conditional PDFs of the amplitude are independent of the phase, but not identical $p_{\varepsilon} \neq p_{\tilde{\varepsilon}}$ like the conditional PDFs of the phase variable $p_{\varphi} = p_{\tilde{\varphi}}$, which depends on the amplitude. The denominator in equation 5 corresponds to the integral of 4 with respect to the estimated phase

$$\begin{aligned} p_{\tilde{\varepsilon}}(\tilde{\xi} | \xi) &= \int_0^{2\pi} p_{\tilde{\varepsilon}, \tilde{\varphi}} d\tilde{\varphi} \\ &= \tilde{\xi} e^{-\frac{1}{2}(\tilde{\xi}^2 + \xi^2)} I_0\left(\tilde{\xi}\xi\right), \end{aligned} \quad (7)$$

which is also known as the Rice distribution with the Bessel function of first kind and zeroth order I_0 . Consequently, the univariate conditional PDFs of the true amplitude and phase yield

$$\begin{aligned} p_{\varepsilon}(\xi | \tilde{\xi}) &= \int_0^{2\pi} p_{\varepsilon, \varphi} d\varphi = \frac{p(\xi)}{p(\tilde{\xi})} \int_0^{2\pi} p_{\tilde{\varepsilon}, \tilde{\varphi}} d\varphi \\ &= \frac{p_{\tilde{\varepsilon}}(\tilde{\xi} | \xi) p(\xi)}{\int p_{\tilde{\varepsilon}}(\tilde{\xi} | \xi) d\tilde{\xi}}, \end{aligned} \quad (8)$$

$$\begin{aligned} p_{\varphi}(\varphi | \tilde{\varphi}) &= \int_0^1 p_{\varepsilon, \varphi} d\varepsilon = \int_0^1 \frac{p_{\tilde{\varepsilon}, \tilde{\varphi}} p_{\varepsilon}(\xi | \tilde{\xi})}{p_{\tilde{\varepsilon}}(\tilde{\xi} | \xi)} d\varepsilon \\ &= \frac{1}{2\pi} \int_0^1 \frac{p_{\varepsilon}(\xi | \tilde{\xi})}{e^{\tilde{\xi}\xi \cos(\Delta\varphi)} I_0(\tilde{\xi}\xi)} d\varepsilon. \end{aligned} \quad (9)$$

Analytic Model of Depolarization The generic model to describe the in-plane depolarization is based on the assumption that the individual spin tunes v_s of the ensemble follow a probability distribution. Latter strongly depends on the emittances of the beam. In the following only a decoupled vertical phase space motion is taken into account since the longitudinal and radial ones are substantially smaller. Thus, the two dimensional vertical phase space can be specified by the vertical position x of the particle and its momentum x' . Assuming that both quantities correspond to Gaussian distributed random variables the spin tunes are distributed according to

$$p_{v_s}(v_s | v_s^{\text{ref}}, \sigma_R) = \frac{v_s - v_s^{\text{ref}}}{\sigma_R^2} e^{-\frac{(v_s - v_s^{\text{ref}})^2}{2\sigma_R^2}}, \quad v_s \geq v_s^{\text{ref}}, \quad (10)$$

which is also known as the Rayleigh distribution with shape parameter σ_R . Latter defines the width of the spin tune distribution and it is indicated by the subscript R (Rayleigh). The spin tune of the particle on the reference orbit is given by ν_s^{ref} . The turn depending spin phase of each particle i yields

$$\varphi_{s,i}(n) = 2\pi(\nu_{s,i} - \nu_s^{\text{ref}})n, \text{ for } \varphi_{s,i} \in (0, 2\pi]. \quad (11)$$

Thus, the spin phase is described by a wrapped PDF, which can be written in terms of the characteristic function of the Rayleigh distribution ϕ_{φ_s}

$$p_{\varphi_s}^w(\varphi_s | \sigma_R, n) = \sum_{k=0}^{\infty} \frac{1}{4\pi^2 n^2 \sigma_R^2} (\varphi_s + 2\pi k) \times \exp\left(-\frac{1}{4\pi^2 n^2 2\sigma_R^2} (\varphi_s + 2\pi k)^2\right), \quad (12)$$

$$= \frac{1}{2\pi} \sum_{k=0}^{\infty} \phi_{\varphi_s}(k | n\sigma_R) e^{-ik\varphi_s}, \quad (13)$$

where the substitution $n\sigma_R = \sqrt{2}\pi n\sigma_R$ is used. The first circular moment of a wrapped PDF is simply given by its characteristic function evaluated at the integer argument $k = 1$

$$\langle z \rangle = \int_0^{2\pi} p_{\varphi_s}^w(\varphi_s | n\sigma_R) e^{i\varphi_s} d\varphi_s \quad (14)$$

$$= \phi_{\varphi_s}(k = 1 | n\sigma_R) \quad (15)$$

$$= 1 - \sqrt{\pi} n\sigma_R e^{-(n\sigma_R)^2} [\text{erfi}(n\sigma_R) - i], \quad (16)$$

where erfi represents the imaginary error function. The length of the mean resultant and the mean phase correspond to the turn depending amplitude and the phase of the spin ensemble

$$\varepsilon(n\sigma_R) = |\langle z \rangle| \quad (17)$$

$$= \left(\left[1 - \sqrt{\pi} n\sigma_R e^{-(n\sigma_R)^2} \text{erfi}(n\sigma_R) \right]^2 + \pi(n\sigma_R)^2 e^{-2(n\sigma_R)^2} \right)^{\frac{1}{2}}, \quad (18)$$

$$\varphi(n\sigma_R) = \arg(\langle z \rangle) \quad (19)$$

$$= \frac{\pi}{2} - \arctan\left(\frac{1}{\sqrt{\pi}} \frac{e^{(n\sigma_R)^2}}{n\sigma_R} - \text{erfi}(n\sigma_R)\right). \quad (20)$$

Results As soon as the polarization is tilted into the horizontal plane by means of an RF-solenoid the analysis starts to assign a turn number to each detected event. In the beamtime May/June 2015 it was shown that the phases of the spin ensemble persisted coherently for more than 1000s in the case of optimized settings of the sextupole magnets [2]. In this report the data is reanalyzed based on the new analytic model, which depends just on one parameter σ_R .

An example of a long and of a short spin coherence time are given in Fig. 1. The left hand side shows the amplitude and on the right hand side the phase spectrum is presented. The black data points are the estimated values $\tilde{\varepsilon}$ and $\tilde{\varphi}_s$ obtained by the turn discrete Fourier transform. In addition, the

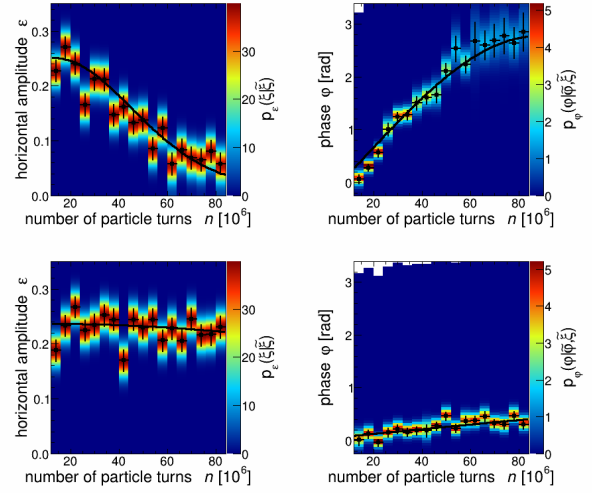


Fig. 1: The black data points represent the estimated values obtained by the turn discrete Fourier transform. The color scheme indicates the respective PDF based on $\tilde{\varepsilon}$ and $\tilde{\varphi}$. The black curves correspond to a maximum likelihood fit based on the turn depending functions 18 and 20 with the PDFs given in 8 and 9.

corresponding true probability density functions p_ε and p_{φ_s} are indicated by the color scheme for each macroscopic turn interval. The black curves correspond to a maximum likelihood fit with the turn depending model functions derived in 18 and 20 and based on the PDFs in equation 8 and 9.

$$\sigma_R^{\text{short}} = (7.26 \pm 0.18) \times 10^{-9} \text{ turns}^{-1}, \quad (21)$$

$$\sigma_R^{\text{long}} = (1.23 \pm 0.19) \times 10^{-9} \text{ turns}^{-1}. \quad (22)$$

Defining the spin coherence time τ_{SCT} as the moment in time where the polarization is decreased to $\varepsilon(\tau_{\text{SCT}}) = \varepsilon_0/e$ of the initial value, one gets

$$\Rightarrow \tau_{\text{SCT}}^{\text{short}} = \frac{0.3536}{\sigma_R^{\text{short}}} = (49.1 \pm 1.2) \times 10^6 \text{ turns}, \quad (23)$$

$$\Rightarrow \tau_{\text{SCT}}^{\text{long}} = \frac{0.3536}{\sigma_R^{\text{long}}} = (287.1 \pm 44.4) \times 10^6 \text{ turns}. \quad (24)$$

^a RWTH Aachen University, Germany, ^b Forschungszentrum Juelich, Germany

References:

- [1] D. Eversmann, V. Hejny, and Hinder et al. New method for a continuous determination of the spin tune in storage rings and implications for precision experiments. *Phys. Rev. Lett.*, 115:094801, Aug 2015.
- [2] G. Guidoboni and Stephenson et al. How to reach a thousand-second in-plane polarization lifetime with 0.97-GeV/c deuterons in a storage ring. *Phys. Rev. Lett.*, 117:054801, Jul 2016.

Dalitz plot of $\eta' \rightarrow \eta \pi^+ \pi^-$ using CLAS g12 data

Sudeep Ghosh

The three body decay of the η' meson has two degrees of freedom, so one can define a Dalitz plot with two variables X and Y for the decay $\eta' \rightarrow \eta \pi^+ \pi^-$, which is defined as follows:

$$X = \frac{\sqrt{3}(T_{\pi^+} - T_{\pi^-})}{Q} \quad (1)$$

$$Y = \frac{(m_\eta + 2m_\pi)}{m_\pi} \cdot \frac{T_\eta}{Q} - 1. \quad (2)$$

Where T_η , T_{π^+} and T_{π^-} are the kinetic energy of a given particles η , π^+ and π^- respectively in the rest frame of η' and $Q = T_{\pi^+} + T_{\pi^-} + T_\eta$. The m_η and m_π are the mass of η and π mesons respectively.

The general parametrization function in Equation. 3 is used to fit a Dalitz plot. The square of the decay amplitude,

$$f(X, Y) = M^2 = A(1 + aY + bY^2 + cX + dX^2). \quad (3)$$

Where a , b , c , and d are the Dalitz plot parameters of the decay and A is the normalization constant.

The Dalitz plot(DP) provides pure kinematic information of a three body decay and also helps to understand the correct input to theoretical distribution of the effective chiral Lagrangian. A Dalitz plot study for the η' meson for the $\eta \pi^+ \pi^-$ decay channel will help to study effective chiral perturbation theory at a low Q limit.

The VES Collaboration has reported the Dalitz plot parameters of $\eta' \rightarrow \eta \pi^+ \pi^-$ with 14.6×10^3 events in charge exchange and 7×10^3 events in diffraction like production [1]. The BESIII Collaboration has also reported $\eta' \rightarrow \eta \pi^+ \pi^-$ decay parameters with 43826 ± 211 events with better precision [2]. The two measurements has disagreement among them and also to the theoretical calculation of the parameters [3].

The report presents a status of Dalitz plot parameters of $\eta' \rightarrow \eta \pi^+ \pi^-$ decay study with CLAS g12 data set, which has the competitive statistics to give the parameters with low statistical errors. It is yet another independent measurement with different systematic errors to cross-check the parameters.

g12 Data Set The g12 experiment ran during March - June 2008 with 26×10^9 recorded production triggers [4]. The fixed target g12 experiment, has an energy of the photon beam ranging from 1.142 GeV to 5.425 GeV. The current analysis uses the 1.45 to 3.60 GeV of the photon beam and used in total 660 runs out of the recorded 626 production runs, 37 single-prong runs and 3 special calibration runs. A step wise corrections and calibration were done accordingly mentioned in the g12 analysis procedure [4].

Simulation The Pluto [v5.42] developed by the HADES collaboration [5], an event generator is used for this analysis. It uses ROOT based programs and it is very commonly used in Hadron Physics experiments to generate hadronic production and decay of mesons. It gives user the freedom to include physics models with simple C++ based codes and to obtain outputs in any desired format. The simulated events in the

analysis are modelled with bremsstrahlung photon, differential cross-section of η' [6] and an input Dalitz plot parameters of $\eta' \rightarrow \eta \pi^+ \pi^-$ decay ($a = -0.150$, $b = -0.100$, $c = 0.000$ and $d = -0.080$).

Reconstruction and event selection To reconstruct the events from the g12 dataset, the following selection, cuts and conditions are used :

1. Events with multiple beam photon within 1.2 ns window are considered as individual events.
2. CLAS g12 Kinematic Fitter is tuned to fit the $M_x(p\pi^+\pi^-)$ as η meson.
3. Vertex cut imposed on event production vertex to be inside the g12 target region.
4. Timing cut of 1 ns on the final state π^+ , π^- and p is applied for improvement on the particle identification.
5. A cut $|\cos\theta_{center-of-mass}$ of $\eta'| \leq 0.85$ is applied to remove events from dead region.
6. Another cut on $|M_x(p\pi^+\pi^-) - 0.547| \leq 0.015$ GeV is also applied.

The events surviving after the conditions goes to the Dalitz plot of 30 x 30 bins in X and Y. A symmetric Dalitz plot is selected as the resolution of X and Y are similar. A bin-wise non-resonant background subtraction is performed to the $M_x(p)$ distribution. All the bins with more 100 events in the 3σ of $M_x(p)$ distribution is fitted with a Voigt function and background is fitted with a Polynomial of order 3. In addition to the non-resonant smooth background, an in peak contribution is also subtracted. A calculation of the in peak contribution in each Dalitz plot bin is done by generating all the in peak background modes with production cross section of η' , relative branching ratio and input Dalitz plot parameters from BESIII measurement [2]. The bins completely inside the Dalitz plot boundary are considered for the analysis. The boundary of the $\eta' \rightarrow \eta \pi^+ \pi^-$ decay is calculated from the MC generator. In order to reject very low acceptance region, an acceptance cut is also placed on the bins which excludes all bins with an efficiency of less than 0.5%.

Fit to the Dalitz plot The Dalitz plot parameters are calculated with two methods:

- Acceptance correction method
- Smearing matrix method

In the first method an acceptance correction is made to the every individual bin, the Dalitz plot parameters are calculated without considering the migration of events from one bin to the other. The second method also takes care of the migrated events using a smearing matrix and finally parameterized to give the Dalitz plot parameters. A χ^2/ndf minimization is performed to fit the bins of the Dalitz plot with MINUIT package available in ROOT. The Dalitz plot parameters obtained from both the methods are consistent.

Systematic study, result and conclusion A detailed study of possible sources of systematics is studied for the cuts mentioned above in addition to the bin width and six different CLAS sectors. The systematic errors obtained from studies are considered only when it cannot be explained from the statistical errors on the parameters. The final Dalitz plot parameters are in reasonable agreement to both published results from theory and experiments. The obtained parameters are with 160090 events which is more than three times the highest statistics reported BESIII Collaboration [2]. This makes the measurement of Dalitz plot parameters in the present analysis more precise with low statistical error.

References:

- [1] V. Dorofeev *et al.*, Phys. Lett. B **651**, 22 (2007)
- [2] M. Ablikim *et al.* [BESIII Collaboration], Phys. Rev. D **83**, 012003 (2011)
- [3] B. Borasoy and R. Nissler, Eur. Phys. J. A **26**, 383 (2005)
- [4] Z. Akbar *et al.* g12 Analysis Procedures, Statistics and Systematics. Technical report, CLAS Technical Note, 2016.
- [5] I. Froehlich, Lorenzo Cazon, T. Galatyuk, V. Hejny, *et al.* Pluto: A Monte Carlo Simulation Tool for Hadronic Physics. PoS, ACAT2007:076, (2007)
- [6] M. Williams *et al.* [CLAS Collaboration], Phys. Rev. C **80**, 045213 (2009)

Electromagnetic transition form factor of the η meson with WASA-at-COSY

Ankita Goswami

In this work, the Dalitz decay $\eta \rightarrow \gamma e^+ e^-$ has been studied in order to measure the electromagnetic transition form factor of the η meson. The electromagnetic transition form factor of the η meson describes the electromagnetic structure of this particle at $\eta \rightarrow \gamma \gamma^*$ vertex. This γ^* decays into di-lepton pair. Here, the momentum transfer squared by γ^* is equal to the invariant mass squared of the di-lepton. For a point-like particle, decay rate can be measured using QED calculations. However, the complex structure of the particle modifies its decay rate. By comparing the experimentally measured decay rate with QED calculation, transition form factor is deduced.

$$\frac{d\Gamma}{dq^2} = \left[\frac{d\Gamma}{dq^2} \right]_{pointlike} [F(q^2)]^2 \quad (1)$$

where function $\frac{d\Gamma}{dq^2}$ is the experimentally measured decay rate, $\left[\frac{d\Gamma}{dq^2} \right]_{pointlike}$ is the theoretically calculated decay rate for a point like particle, $F(q^2)$ is the form factor of the particle and q^2 is the squared four-momentum of $e^+ e^-$.

The slope of the transition form factor is a very important quantity as it is related with the radius of spatial charge distribution. Most recently, CB/TAPS at MAMI collaboration has reported the value of the slope of the form factor $\Lambda^{-2} = (1.95 \pm 0.15_{stat} \pm 0.10_{syst}) GeV^{-2}$. This result is already in very good agreement with theoretical calculations and Vector Meson Dominance Model. We expect to contribute to the result with our high statistics dataset. Transition form factor is also important in the study of the anomalous magnetic moment ($g-2$) of the muon, which is a precise test of the standard model.

The data analyzed in this work has been collected in 2010 using proton-proton reaction at a beam kinetic energy of 1.4 GeV. The η meson are produced in the proton-proton reaction. The recoil protons are identified in the layers of Forward Range Hodoscope whereas the charged decay products are identified in the central part of the detector and photons are identified with the help of the electromagnetic calorimeter. The signal events $\eta \rightarrow \gamma e^+ e^-$ are enfolded with the multipion background, which is produced in the proton-proton reaction. In order to extract clean signal $\eta \rightarrow \gamma e^+ e^-$, certain kinematical conditions have been implemented. Events are passed through the criteria of energy-momentum conservation to suppress multipion background. When the photons coming from other sources than the signal interact with the beam-pipe material, converts into $e^+ e^-$ pair, which has different four-vectors than the $e^+ e^-$ coming from γ at the vertex. The conversion background originates at the radius of the beam-pipe. This information is used to reject such type of background. Pho-

tons and electrons produce electromagnetic shower in the calorimeter. Discontinuous shower is called split-offs. The angle between the photon candidate and the split-off should be very small. Split-offs are rejected utilizing this property. After all these conditions implemented to reduce background, the η meson is reconstructed using the missing mass technique. The Fig. 1 shows the missing mass of protons.

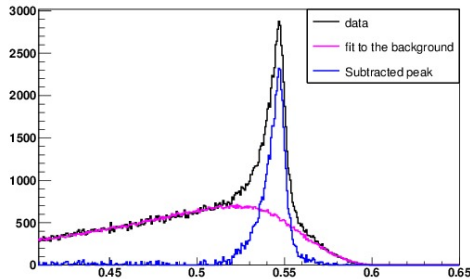


Fig. 1: Missing mass plot of two protons after all kinematic conditions used for obtaining the η signal.

In this figure, we can clearly see that the signal is sitting over the multipion background. In a detailed simulation study of background channels, it is seen that $pp \rightarrow pp\pi^0\pi^0$ is the main source of the background. Hence, in the missing mass distribution, the background is fitted with a 4th order polynomial multiplied with the phase-space of $pp \rightarrow pp\pi^0\pi^0$ excluding the peak region (0.53–0.57). After fitting, the background is subtracted. The remaining signal peak is integrated. A total of approximately 43k $\eta \rightarrow \gamma e^+ e^-$ event candidates are reconstructed. However, 8.4% background is still contributing inside the peak region from $\eta \rightarrow \gamma\gamma$, $\eta \rightarrow \gamma\pi^+\pi^-$, $\eta \rightarrow \pi^+\pi^-\pi^0$ channels. We have calculated the relative branching ratio ($\eta \rightarrow \gamma e^+ e^- / \eta \rightarrow \gamma\gamma$). The value of relative branching ratio is 0.019 ± 0.0001 . We have a plan to use another technique, called Kinematic Fit in order to suppress background. The error parameterization is in progress to do a kinematic fit. With the signal events, remaining after background subtraction using kinematic fit, we will finally go for the further transition form factor studies.

Electrostatic deflector development

K. Grigoryev^a for the JEDI collaboration

The investigation of the permanent electric dipole moment (EDM) of charged particles at COSY requires a new electrostatic storage ring. Precursor experiments can be realized using existing facility with implementation of electric (electrostatic or combined electric and magnetic) elements into the current ring. Ongoing development is carried out in dedicated cleanroom laboratory at RWTH Aachen University with scaled electrode prototypes. Different materials and polishing procedures as well as ultra-high vacuum techniques and the dark current measurement procedure were studied.

Mechanically polished stainless steel electrodes at the distances of a few millimeters demonstrate the high-voltage discharge close to the breakthrough conditions in ultra-high vacuum. Aluminum electrodes machined and polished with the same technique showed smaller values of the electric field strength. Nevertheless, both materials showed electrical field strength above calculated values for deflector prototype (17 MV/m).

Good agreements with theoretical predictions of the breakdown conditions allow to continue investigations at higher voltages and larger distances between the electrodes. It will require 1) radiation protection laboratory, because of higher energy x-rays and much stronger power supplies. All necessary infrastructures for such laboratory are available inside the storage ring building, which may be possible solution for such laboratory.

The existing test bench for experiments with small deflectors (shown in Fig. 1) can be used to develop non destructive measurement technique for electric field measurement in ultra-high vacuum. It can be done with hollow-core photonic crystal fibre developed in Max Planck Institute for the Science of Light, Erlangen¹.



Fig. 1: The test bench for electrostatic deflectors.

The sample of the hollow-core fiber was provided for UHV tests at RWTH Aachen. The existing test stand was equipped with additional heating and the quadruple mass spectrometer². The fiber was stretched between two vacuum flanges and fixed with TorrSeal epoxy³. Heating tests of the fiber and hardened epoxy showed no outgassing. It allows preparing additional electrical tests, which can be performed at MPI Erlangen.

The described method¹ to measure electric field unfortunately is directly applicable only to oscillating voltage. Adding sinusoidal signal with the amplitude of 1% from the main voltage should make these measurements feasible. The discharge protection scheme of the current setup was modified for this purpose. A new signal converter box (see Fig. 2) using external signal generator⁴ will produce a sinusoidal signal in the wide frequency range from 50Hz up to 250kHz. The input voltage of the high-voltage power supply will be taken as reference to define the modulated signal amplitude, which can be varied if necessary.

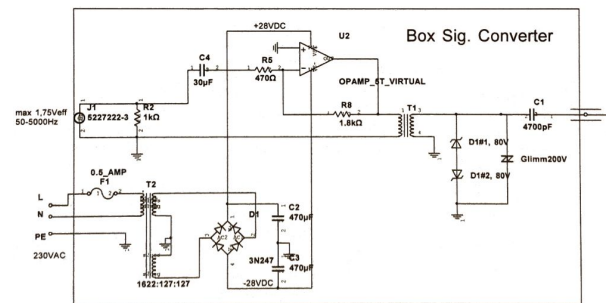


Fig. 2: Signal converter scheme for test stand

New polished stainless steel electrodes (see Fig. 3) with a different surface were produced and at present ready for installation. Special shape of the electrode on the right side of the Figure 3 is made to test uncertainties in electrical field reconstruction.



Fig. 3: New electrodes for testing field measurement technique

First field measurement tests are foreseen to be completed in 2017. The result of these tests will be used to define the electrical field monitoring method during deflector operation.

^a Physikalisches Institut III B, RWTH Aachen University, 52074 Aachen, Germany

¹ Bykov D. et al., Nature Photonics 9, 461–465, (2015).

² Quadrupole mass spectrometers (QMS) PRISMA 200 mass range 1-100 amu, Pfeiffer Vacuum, <http://www.pfeiffer-vacuum.com>

³ Agilent low vapor pressure resin sealant <http://agilent.com>

⁴ Voltcraft signal generator FG250D.

Progress with the model development for the 2 MeV electron cooler

A. Halama

The 2 MeV electron cooler has been installed in the COSY ring to provide e-cooling of p^+ and d^+ beams in the entire energy range of the machine and to study the cooling process in the magnetized regime at high energy.

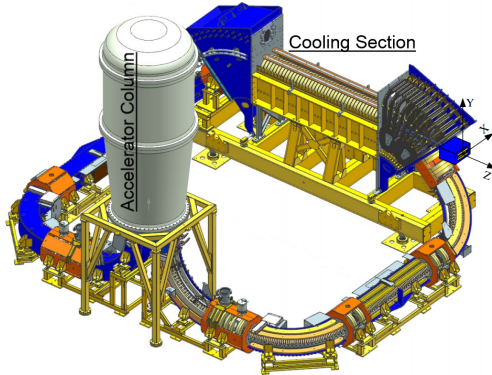


Fig. 1: Cooler magnetic system layout. Edited from [1]

2 MeV electron cooler model introduction

Within the cooling section a velocity-matched electron beam is placed coaxially over the beam circulating in the ring. Coulomb interaction between the beams allows heat transfer analogue to heat exchange of gases. The electron beam is guided by a strong longitudinal magnetic field to preserve its quality. The geometry of the beam line however gives rise to higher order dynamics such as larmor rotation and the so called galloping motion, which must be minimized to yield a cold e-beam. Setting up the electron cooler and delivering a high quality electron beam by adjusting all required parameters manually is a time consuming, demanding task and requires a high level of expertise. Beam properties such as orbit, larmor motion and galloping [2] have to be measured and corrected to a satisfying degree. To ease the beam setup significantly a model for calculations of electron trajectories is under development. This model, embedded in a GUI, will serve as a tool to anticipate beam behavior, perform response calculations and find solutions for suitable magnet settings. Every magnetic ensemble has been simulated in COMSOL, yielding magnetic field maps. These are scaled linearly with the set current for the time being but are prepared to reflect saturation and hysteresis effects at a later stage of the development. Electron trajectories are obtained by integration using the equation of motion in a static electric and magnetic environment. Momentum conservation is taken into account but this requires small time increments over the integration path in the range of picoseconds. This leads to total computational times in the range of tenths of seconds up to several seconds depending on scope and precision of the calculation for one trajectory per used thread. Trajectory information is available as xyz electron path data points, also broken down only to the 12 beam position monitor (BPM) locations and sectionwise as resulting fit coefficients. As the electron beam is affected mainly by the strong longitudinal guiding field and dipole fields for steering, the trajectory fit is described in

the following form:

$$x_i(z) = x_0 + mz + A\sin(\omega z) + B\cos(\omega z)$$

The form is similar for y . m describes the drift ratio, ω is called the magnetic wave number of the larmor motion determined by the average field strength in the section. A and B can be used to represent larmor radius and phase. Larmor rotation is mostly caused by mismatched longitudinal fields in the bending sections, as special requirements for the passage through these have to be met to not excite the beam with a certain larmor stimulus. The galloping effect occurs due to inevitable gradient fields in the magnetic guiding structure of the cooler. In such gradient regions different parts of the beam experience different kicks such that the beam is larmor excited but with increasing phase advance seen tangentially around the center. The excitation is spatially linearly distributed, which means that the individual larmor radii are increasing linearly with increasing distance to the beam center. Therefore it can also be called galloping growth. The galloping effect is quantified by measuring the larmor coefficients of the center of charge and those from at least one part of the beam slightly off-center. This can also be carried out at the cooler, as the gun can separately modulate each quadrant individually [3] to make certain beam parts visible to the BPM system. Thus the individual larmor rotation of the center of charge of these quadrants can be measured respectively. The larmor rotation, which one measures from the center of charge is superimposed on the entire distribution but carries no galloping motion. Therefore the coherent larmor rotation can simply be subtracted from the off-center beam part. This leaves only galloping component of this part of the beam.

$$x(z, \phi, d) = x_0 + mz + A\sin(\omega z) + B\cos(\omega z) + cr(\phi)\sin(\omega z + \phi) + dr(\phi)\cos(\omega z + \phi)$$

Again similar for y . c and d constitute the galloping growth amplitude in $\mu m/mm$. r and ϕ are polar coordinates of the specific beam part. For high cooling efficiency larmor and galloping motion have to be as small as possible in the cooling section and the orbit has to match the trajectory of the COSY beam. To operate at high beam current a high recuperation rate has to be reached, therefore larmor and orbit has to lie within a desired range also on the collector side of the transport channel. With the help of the model, optimizing beam parameters should be manageable in a shorter amount of time compared to manual adjustments.

Relative similarity and status of the model

For beam adjustments from a known initial orbit, one can work with iterative procedures to correct the orbit and larmor motion. Relative changes to the cooler can therefore also be reflected by the model. Response schemes do not have to be measured but can simply be calculated in a much faster fashion. Whereas additionally some beam information is simply not accessible by measurements by the given diagnostics of the electron cooler but can be accessed using an accurate model. The simplest response scheme is that of the orbit with respect to steering magnets, generally called the orbit response matrix (ORM). It is obtained as broad measurement of all orbit displacements at the BPM locations as result of dipole corrector current changes. Such an ORM can be used

for orbit adjustments such as alignments, orbit bumps, feedback and feed forward systems. It has been shown that the calculated orbit response matrix matches the measured one to a satisfying extend. Calculated response data has been used already for a slow feedback system in which a specific beam position was held fixed by automated readings and settings to stabilize the beam while manual changes to the orbit were introduced. The calculated ORM was also used for manual orbit adjustments within the design orbit tool. Within that, a wanted orbit can be chosen for which the necessary currents are calculated automatically and set at the magnets. The bending sections are individually equipped with inner and outer dipole magnets. With the help of these the beam shape can be manipulated as the currents of inner and outer magnet are changed in opposite directs. The orbit is not affected, if the average value of inner and outer coil current remains the same. It could be shown that shaping the beam within the model works as in the electron cooler aside from a specific scaling factor. The larmor rotation is compensated using short dipole kickers that transmit a certain kick with the right strength and phase. The exact setting is a solution using the larmor response that is how the larmor rotation changes relative to certain kicks. Beside the fact, that the model can directly rely on trajectory fits to quantify the larmor rotation instead of an indirect measurement, the compensation procedure works also as expected. Galloping rotation occurs mostly in the junction between the weak magnetic field in the accelerator column and the stronger field in the first bending section. A matching section is installed to shape the magnetic profile to decrease the effect of gradient fields. However finding a solution is only doable with lengthy measurements or with support of the model. The simplest approach therefore is following the negative gradients in small but reasonable current steps iteratively for all 7 magnets of the matching section. [2] This procedure works fine within the model and several solutions can be found depending on the initial setting.

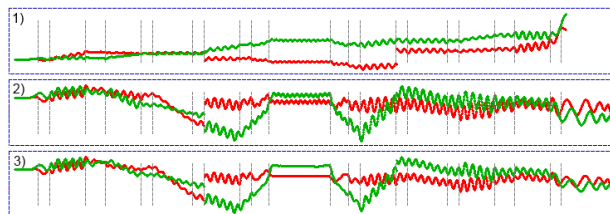


Fig. 2: Trajectory calculations for a single 1000 keV electron with different steps of correction. Red trace represents x-coordinate and green trace y, in the BPM coordinate system

Figure 2 shows samples views of the GUI, which gives access to the model. The first plot shows the trajectory without any corrector magnets turned on. The beam carries a large larmor radius and is lost prior to deceleration. The second plot shows the trajectory for an orbit corrected case. The beam is not lost, however is still incapable of cooling, due to the strong larmor rotation evident in the cooling section (central region of the image). The last image shows the final trajectory with additional larmor correction in the cooling section. The traces were calculated for a single electron representing the center of charge of the beam. Figure 3 shows traces of 5 electrons representing the the distribution. Steps of the gal-

loping correction process are displayed. The first plot shows the initial uncorrected condition. All parts of the beam carry larmor rotation and depending on the location within the distribution a superimposed individual rotation. This leads to the galloping of the envelope for an entire distribution. Thus the radii and phases are different for each trace. The second plot shows the larmor compensated case. The 90° phase relation can be seen. Plot three shows the galloping corrected case without larmor correction. The equalized and now coherent larmor rotation is easily recognized. Image four shows the galloping corrected case with consecutive larmor correction. The beam with such properties is suitable for cooling.

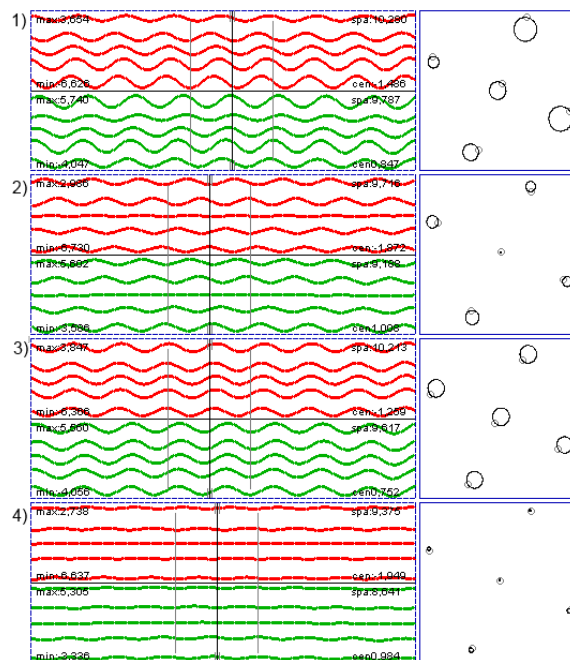


Fig. 3: Further trajectory calculations, now for a beam distribution. In red the x- and in green the y-coordinate within the cooling section. The cross section view at the location of the cursor is next to it

Model discrepancies and next steps

The relative beam behavior within the model is close to that of the electron cooler. However, the model does not describe the electron cooler with an absolute one to one match. This is observed as non-perfect agreement of measured and calculated orbits, larmor and galloping properties. This results most likely from the fact that the model assumes perfect alignment of the beam to the geometric center in the accelerator column at the beginning of the calculation. It is an ongoing effort to compare both systems in detail to find the correct initial conditions and appropriate correcting scaling factors to certain magnetic structures. This presents itself as a complex task, since there is no specific diagnostics available and no space left for any to ease the matching. Similar to a least square approach, one could trace back the electron trajectory from measured beam positions. Larmor phase relation and transverse momentum would be used from larmor radius measurements at three locations of the transport channel. This idea will be investigated and implemented soon. Further model calibration will rely on measurements and procedures that are not part of the routine operation and go beyond com-

paring response functions. Some measurements have already been performed to investigate similarity and the possibility to reduce the discrepancies between the trajectories of the cooler and of the model. The following measurements have been carried out:

- Orbit and Larmor response with respect to main magnets settings
- Larmor and Galloping response of the matching section
- Non-linear orbit shift induced by short dipole corrector
- Larmor kick to orbit shift ratio
- Finding multiple settings for the magnetic system for in depth trajectory comparison
- Analyzing Larmor phase advance propagation due to longitudinal field changes in bend and line sections

A better agreement would allow describing the electron by its entirety through the model. Any setting for a cool and matched beam could be found much faster than by manual means. Any lengthy measurement for response schemes would be carried out by the model. Application of these to set the smooth orbit with a low rms orbit distortion, the matching of the COSY beam that is to be cooled and the electron beam as well as guaranteeing a suitable recuperation rate, which improves reliability by reducing the probability of HV breakdowns, is done numerically. As the trajectory of the electron beam in the cooling section is properly known, one can get a much clearer view on the cooling process, which would also serve well in the fields of cooling theory and cooling simulation. On the way to this point, the GUI, which embeds the model, will become a tool to additionally serve the currently used monitors for the orbit as well as current and voltage settings for various power supplies. Logging and archiving using EPICS through this software is also envisaged.

Conclusion

A model to describe electron trajectories in the 2 MeV electron cooler transport channel is under development. At the current development stage it shows qualitative agreement with the physical and measurable beam behavior. The most important correcting features have been shown to work within the model. It is an ongoing effort to benchmark the model and match it closer to the absolute behavior of the electron cooler and thus match the measured orbit. Monitoring the beam parameters and controlling the cooler will be possible within the same GUI that holds the model. Thus manual changes and adjustments will simultaneously be routed to the cooler and fed into the model. Additionally it allows checking the plausibility of operator inputs to prevent accidental beam losses.

Acknowledgement: The author is thankful for the advice and help from the members of the Budker Institute of Nuclear Physics M. Bryzgunov and V. Reva, Novosibirsk.

References:

- [1] M. Bryzgunov et al., "Magnetic System of Electron Cooler for COSY", BINP, Novosibirsk, Russia
- [2] A. Halama, "Development of an automatic adjustment of the transport channel of the 2 MeV electron cooler at COSY," Forschungszentrum
- [3] M. Bryzgunov et al., "Electron Gun with Variable Beam Profile for COSY Cooler", BINP, Novosibirsk, Russia Jülich, Germany, annual report 2016

Theoretical Considerations of a Beam Position Independent Capacitive Quadrupole Pickup

A. Halama

In the course of investigations towards capacitive Beam Position Monitors (BPM), the idea of a capacitive device capable of measuring more than beam phase, current and position was looked at in more detail. The investigation focused early on a design with eight stripes as electrodes. The presented geometry is capable of measuring the quadrupole moment of a relativistic particle beam. Two such devices at appropriate locations within a ring accelerator could resolve the beam size for a known dispersion.

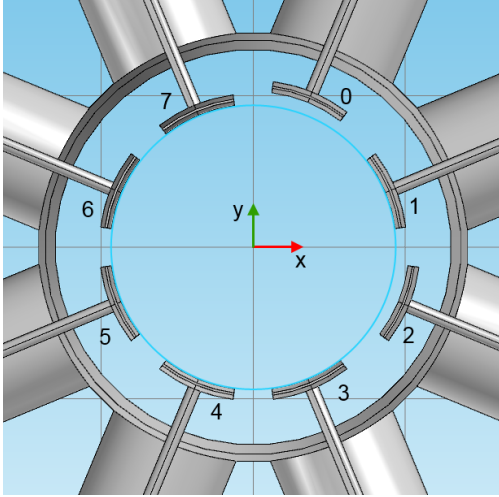


Fig. 1: Simplified model of the quadrupole monitor.

Capacitive beam position monitors

To understand the principle of the here described device, the capacitive pickup for positional measurements has to be laid out first. The used electrodes are stripe shaped, that means that for any positional measurement the non-linearity of the geometry has to be considered. Within the center region such a pickup can be viewed as linear and can be approximated with two dimensional polynomials in the surrounding vicinity. Retrieving the positional information of a pencil beam from integrated or peak electrode voltages can thereby look like this:

$$x = \sum_{i=0}^N \sum_{j=0}^N K_{x,ij} \left(\frac{\Delta x}{\Sigma_x} \right)^i \left(\frac{\Delta y}{\Sigma_y} \right)^j \quad (1)$$

$$y = \sum_{i=0}^N \sum_{j=0}^N K_{y,ij} \left(\frac{\Delta x}{\Sigma_x} \right)^i \left(\frac{\Delta y}{\Sigma_y} \right)^j \quad (2)$$

Where K is the matrix holding the offset, linear sensitivity term, higher order terms, and cross terms also depending on the orthogonal coordinate. The matrix is unique to every configuration of chosen up, down, left, and right groups of electrodes. Δ refers to the difference signal resulting from opposing groups of electrodes and Σ results from their sum, each only for a chosen configuration. Not all combinations one can think of result in stable matrices. However about 50 unique configurations have been found. Some of the more

common ones with the clockwise enumeration are shown here:

Some possible configurations			
Up	Down	Left	Right
6,7,0,1	2,3,4,5	4,5,6,7	0,1,2,3
0,7	5,6	0,7	1,2
0,6,7	4,5,6	0,6,7	1,2,3
0,6,7	2,3,4	5,6	1,2

Table 1. Exemplary summary of capacitance values.

The matrix entries in K can be obtained as fit coefficients by measurement or numerical procedures that reflect the induction of charges by the beam onto the electrodes. Beside the chosen configuration, the matrix is also strongly dependent on the beam size. This means that a set of coefficient matrices can be obtained for various beam sizes. A Gaussian distribution has been assumed for the presented work. One way of representing the beam size dependency is to express each coefficient by another two dimensional polynomial with RMS beam size σ_x and σ_y as input arguments. By this substitution the function looks as follows:

Size dependent response scheme

$$x = \sum_{i=0}^N \sum_{j=0}^N \left(\sum_{l=0}^M \sum_{m=0}^M G_{x,ijml} \sigma_x^l \sigma_y^m \right) \left(\frac{\Delta x}{\Sigma_x} \right)^i \left(\frac{\Delta y}{\Sigma_y} \right)^j \quad (3)$$

$$y = \sum_{i=0}^N \sum_{j=0}^N \left(\sum_{l=0}^M \sum_{m=0}^M G_{y,ijml} \sigma_x^l \sigma_y^m \right) \left(\frac{\Delta x}{\Sigma_x} \right)^i \left(\frac{\Delta y}{\Sigma_y} \right)^j \quad (4)$$

This form would yield the exact beam position for a certain configuration of electrodes with known beam size. For deviating beam size inputs from the actual beam size (or to be more precise; different quadrupole moments without the beam position terms) several configurations will lead to different readings. This deviation expressed as standard deviation can be plotted versus both input beam sizes.

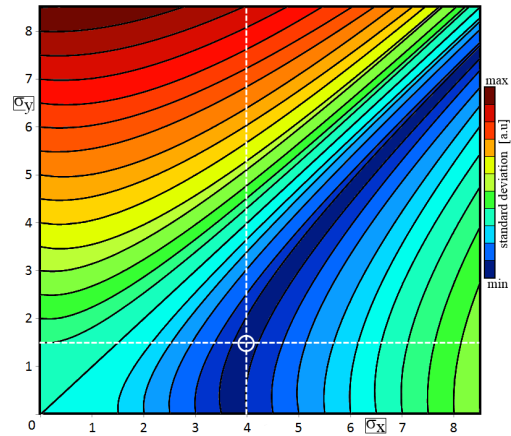


Fig. 2: Intensity plot of the standard deviations as a function of input beam sizes in Eq. 3 and 4. Set beam position for the presented calculation is $\sigma_x = 4mm$ and $\sigma_y = 1.5mm$.

One obtains agreement of the resulting beam position for the different configurations only for a suitable beam size input along the dark blue valley in figure 2, where the standard deviation approaches zero. The valley can be parametrized by the quadrupole moment without the beam position terms as a function of both beam sizes. $\kappa_{postIndep} = \sigma_x^2 - \sigma_y^2$. The solution to κ can quickly be found numerically by sweeping through the larger of both beam sizes and setting the other to zero, as there is an absolute minimum along this axis. The location of the minimum reveals the wanted magnitude: $\sqrt{\kappa_{postIndep}}$. The beam position is automatically obtained as the resulting average beam position of all configuration at the lowest standard deviation. This way the complete quadrupole moment can be reconstructed as:

$\kappa = \kappa_{postIndep} + x^2 - y^2$. For two such devices at dissimilar and known beta function and known dispersion the vertical and horizontal emittance can be calculated. [3]

$$\kappa_1 = \varepsilon_x \beta_{x1} - \varepsilon_y \beta_{y1} + \bar{D}_{x1}^2 \sigma_p^2 \quad (5)$$

$$\kappa_2 = \varepsilon_x \beta_{x2} - \varepsilon_y \beta_{y2} + \bar{D}_{x2}^2 \sigma_p^2 \quad (6)$$

By solving this linear set of equations, as $\kappa_{1,2}$ are known, the emittance and hence the beam size at the location of the pickups can be obtained.

Numerical method

For the investigation eight beam size and position dependent scalars that are linear with the image current have been used as representation of electrode signals. This simplification was implemented, since the voltage signals on the electrodes scale with the image current. Cross talk effects were neglected, as only the sensitivity is damped but this does change the general behavior. The wall current approach has been used to reflect the electrostatic induction. The total influence of the beam as a distribution of particles has been implemented by summing up the influence results of a fine gridded two dimensional gaussian distribution from a linear interpolation in a fine pre-calculated grid of pencil beam inductions. This approach was refined in the code to yield precise results that are close to convergence values. It also proved itself as a faster method compared to the calculation of individual inductions of each gaussian portion. All calculations were carried out in Java code. To look closer at the feasibility of such a device one will have to use a more proper model, that takes also cross talk between the electrodes into account and noise from the input impedance of the preamplifier. The stability of the matrices and the uncertainty of the resulting quadrupole moment are thereby in question.

Conclusion

The concept for a capacitive and thereby non-invasive device that can measure the quadrupole moment has been studied. It could be shown numerically, that a capacitive device with eight electrodes, from which two are shifted slightly, is capable of measuring the quadrupole moment of a particle beam.

Acknowledgement

The author is grateful for the kind support of B. Breitzkreutz, C. Böhme, B. Lorentz, V. Kamerzhiev, B. Nauschütt, P. Niedermayer, R. Stassen, H. Stockhorst

References:

- [1] P. Fork et al., "Beam Position Monitors", CERN Accelerator School 2009, GSI, Germany.
- [2] R. E. Shafer, "Beam Position Monitoring", AIP Conference Proceedings 1989, Los Alamos National Laboratory.
- [3] A. Janson, "Noninvasive single-bunch matching and emittance monitor", Accelerators and Beams, Volume 5, 072803, 2002, CERN, Switzerland.

Analysis of Feedback System Data

N. Hempelmann for the JEDI Collaboration

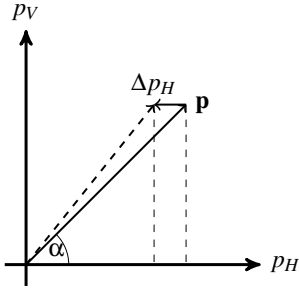


Fig. 1: Effect of decoherence on vertical spin build-up. If the horizontal polarization decreases by Δp_H , the angle α increases.

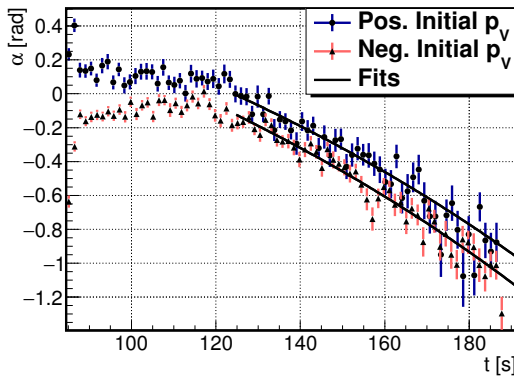


Fig. 2: Gradual tilt of the polarization towards the vertical axis. The blue curve corresponds to positive initial polarization, the red curve to negative polarization

Feedback System The spin feedback system was successfully tested in fall 2015 (see also the corresponding highlight section and the 2015 annual report). The system was used in two distinct experiments: gradual vertical spin build-up using and rf-solenoid while the feedback system is on, and driven spin oscillations in which the feedback system is used to set the initial conditions.

Vertical Spin Build-Up The system was initially tested by switching on the solenoid at low amplitude after the feedback is activated. The solenoid gradually tilts the spin out of the horizontal plane.

The polarimeter measures the vertical and horizontal polarization p_V and p_H . In the analysis, the angle α between the polarization vector and the horizontal plane is used. The rate at which α approaches $\pm\pi/2$ is proportional to the sine of the phase ϕ between the solenoid and the spin tune precession. The experiment can therefore verify that the feedback system works.

The model used to fit the data also accounts for the decay of the horizontal spin component over time, which can fake a spin rotation (Fig. 2). Fig. 2 shows an example of the vertical spin build-up over time for one run. Fig. 3 shows the rate of spin rotation as a function of the nominal phase set in the feedback system. The expected sine shape is found. There is no significant difference between positive and negative initial

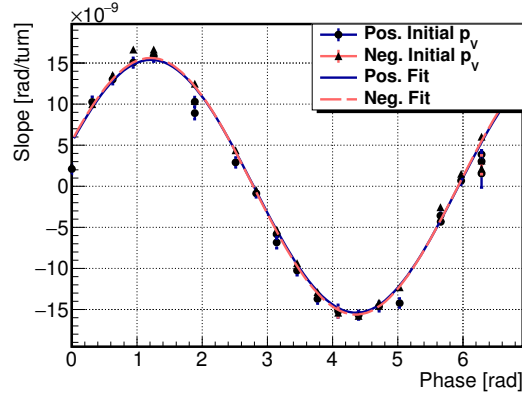


Fig. 3: Spin rotation per turn as a function of the initial phase.

polarization.

The gradual build-up of vertical polarization resembles the expected signal for an electric dipole moment in the precursor experiment. The effects of polarization decay apply in both cases.

Driven Oscillation The feedback system was also used to study driven oscillation of the polarization vector induced by an RF solenoid as a function of the initial phase. For this, the feedback system was first used to set the initial phase difference $\Delta\phi$ between the solenoid and the spin precession, but was then switched off, i.e. $\Delta\phi$ was not controlled while the solenoid was operated.

The spin motion is parametrized using the angle between the spin and the horizontal plane α and the phase difference $\Delta\phi$. The behavior of the spin under the influence of the solenoid can be described using a simple geometrical model that assumes that the spin is rotated by the angle k around the z axis each turn. This leads to the following equation of motion

$$\begin{aligned} \frac{d(\Delta\phi)}{dn} &= \frac{k}{2} (\tan\alpha \sin\Delta\phi + q) \\ \frac{d\alpha}{dn} &= \frac{k}{2} \cos\Delta\phi. \end{aligned} \quad (1)$$

With $q = \frac{4\pi(v_s - v_s^{\text{sol}})}{k}$, where v_s is the actual spin tune and v_s^{sol} is the spin tune to which the solenoid is set. The parameter q is a measure for how far the solenoid is away from the resonance frequency. Figure 4 shows some solutions for $k = 5 \cdot 10^{-7}$ and $q = 0.2\pi$. The oscillations in α and $\Delta\phi$ are typical features. It can be shown analytically that α oscillates around $-\arctan(q)$ and $\Delta\phi$ oscillates around $\pm\pi/2$. The length of one oscillation period is $\frac{4\pi}{k\sqrt{1+q^2}}$. If the amplitude exceeds a critical value depending on q , $\Delta\phi$ no longer oscillates but moves around the complete unit circle.

This behavior was verified by fitting the numerical solution of Eq. (1) to the measured data: Figure 5 shows a run close to $q = 0$, while Fig. 6 is for a run further away from resonance.

The same general rules also apply to a Wien filter that rotates the spin about an axis perpendicular to the beam and the

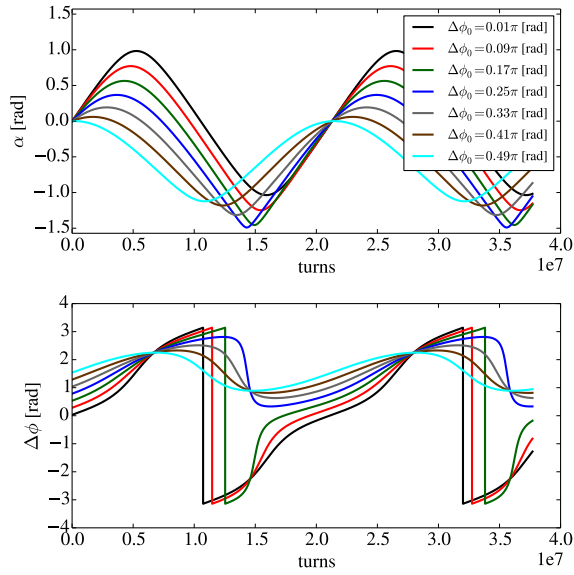


Fig. 4: Numerical solution for (1) for different initial conditions: $k = 5 \cdot 10^{-7}$, $q = 0.2\pi$

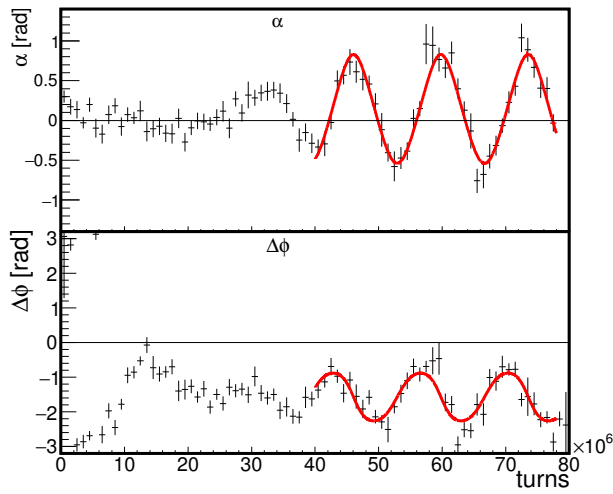


Fig. 5: Example 1: Oscillations close to resonance.

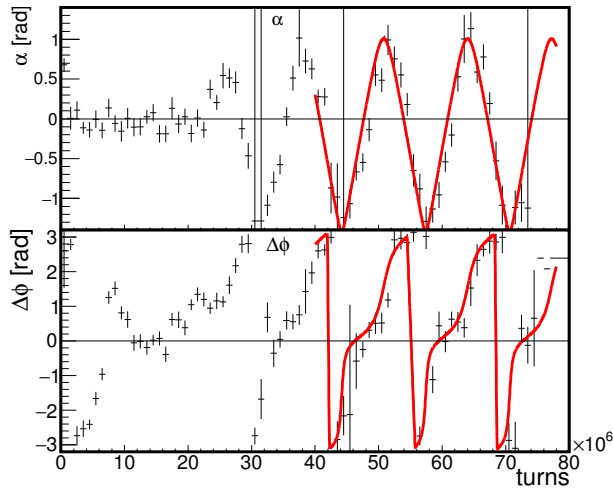


Fig. 6: Example 2: $\Delta\phi$ moves over the complete angular range.

stable spin axis. The equation of motion (1) can also describe the initial spin flip from vertical to horizontal.

Conclusion The analysis proves that the feedback system works and fulfills the conditions for electric dipole measurements in the precursor experiment. The analysis of the driven oscillations shows that it is also useful as a general tool to study spins in storage rings.

Lyapunov Analysis of Particle Tracking for the High Energy Storage Ring (HESR)

J. Hetzel*

For the future Facility of Antiproton and Ion Research (FAIR) in Darmstadt, the IKP is responsible for the construction of the High Energy Storage Ring (HESR) [1]. In December 2014 the series production of the bending sector dipoles and focusing quadrupole magnets has started. In beam dynamics simulations the measured field imperfections of these elements is included as source of non-linear particle motion. The simulations are then used to determine the area of stable motion. Its border marks the transition to chaotic motion and is called Dynamic Aperture. It is estimated from the simulation results using a variant of the Lyapunov exponent. Only below the Dynamic Aperture limit a stable operation of the storage ring can be guaranteed.

The principle of the measurement of the magnetic field of the dipole with hall probes has been described in [2]. The magnetic field of the quadrupole is measured by the manufacturer with a rotating coil, cf. [3]. Both measurements can be expressed through multipole coefficients \mathcal{B}_n and \mathcal{A}_n as defined through[4]:

$$B_\theta(r, \theta) + iB_r(r, \theta) = \sum_{n=1}^{\infty} (\mathcal{B}_n + i\mathcal{A}_n) \left(\frac{r}{r_0}\right)^{n-1} \cdot e^{i\theta}, \quad (1)$$

where B_r and B_θ are the integrated components of the elements' B field in radial and polar direction, r and θ are polar coordinates with origin at the reference trajectory and r_0 is a fixed reference radius. The component \mathcal{B}_1 of the dipole and \mathcal{B}_2 of the quadrupole are called main field components. All other non-vanishing multipole components \mathcal{A}_n (skew multipoles) and \mathcal{B}_n (upright multipoles) contribute to non-linear¹ particle motion. Usually these unwanted components are suppressed through the design of the pole shapes of the magnets, but small contributions in the order of 0.1% of the main field remain. These are considered to be the main source of distortion to the stable particle motion. In the beam dynamics simulation only the multipole components up to order $n = 10$ are included. This is rectified as their contri-

¹except the skew quadrupole component \mathcal{A}_2 which introduces coupling of horizontal and vertical phase space - another unwanted effect.

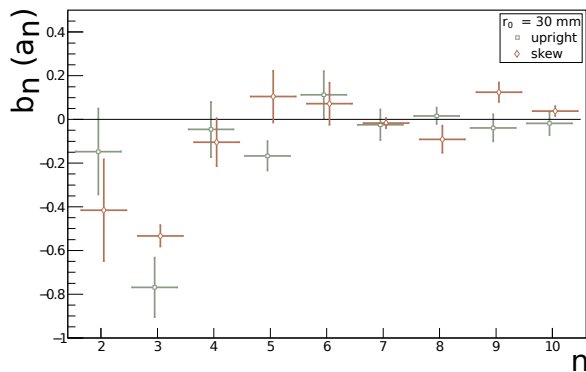


Fig. 1: The measured multipole components of a dipole magnet. The error bars indicate the reproducibility of the results. The measurement is normalized by $b_n = \mathcal{B}_n / (\mathcal{B}_1 \cdot 10^{-4})$ and $a_n = \mathcal{A}_n / (\mathcal{B}_1 \cdot 10^{-4})$.

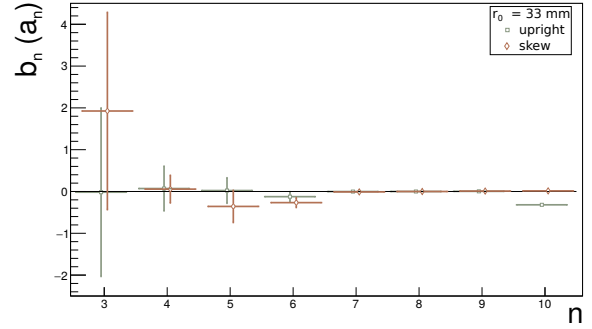


Fig. 2: The measured multipole components of the quadrupole magnets. The error bars indicate the variation of the multipole components within the produced series. The measurement is normalized by $b_n = \mathcal{B}_n / (\mathcal{B}_2 \cdot 10^{-4})$ and $a_n = \mathcal{A}_n / (\mathcal{B}_2 \cdot 10^{-4})$.

bution to the field rises with $\left(\frac{r}{r_0}\right)^{n-1}$ and the path of the particles is usually at $r < r_0$. The results of these measurements are shown in Fig. 1 for the dipole and in Fig. 2 for the quadrupole.

Besides the measured multipoles, the linear lattice for antiprotons at the injection energy of $T = 3$ GeV is basis for the topical studies: The quadrupole strengths and sextupoles strengths are chosen such that the chromaticity ξ is $\xi = 0$ and transition factor γ_{tr} is set to $\gamma_{tr} = 6.2$. As well the dispersion D in the straight sections is close to zero. The horizontal tune Q_x and vertical tune Q_y are regarded as free parameters. They can be adjusted between $7.58 < Q_i \leq 7.76$ oscillations per particle turn. One example for the resulting optical functions is shown in Fig. 3.

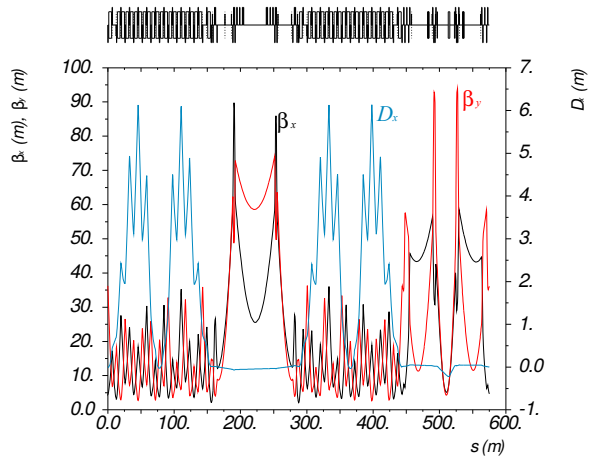


Fig. 3: The optical functions of the HESR antiproton injection lattice. The corresponding tunes are $Q_x = 7.61$ and $Q_y = 7.64$. The PANDA target will be located at $s \approx 515$ m.

Based on the linear lattice along with the measured imperfections as source for non-linear distortions a tracking simula-

tion is performed. Here the trajectory of a particle with given initial phase-space coordinates is calculated. Then the position of the particle in the transverse phase space is recorded for each turn. To save calculation time, for each starting position only the first 1000 turns are tracked. Based on the recorded data the starting point is to be classified as stable or chaotic. Therefore a second particle with initial coordinates as close to the original particle as $d_i = 1.414 \mu\text{m}$ is tracked as well. After each turn medium distances $\bar{d}_{i,f}$ are calculated:

$$\bar{d}_{i,f} = \sum_{n=i}^f \frac{d_n}{f-i}, \quad (2)$$

where d_n is the distance of the two tracked particles after turn n . Following the ideas of [5], a Lyapunov indicator λ_n is calculated from the medium distances:

$$\lambda_n = \frac{\bar{d}_{n/2,n} - \bar{d}_{0,n/2}}{\bar{d}_{n/4,3n/4}}, \quad (3)$$

again n represents the number of turns. Starting from initial coordinates near the design orbit, it is checked if these initial coordinates lead to a Lyapunov indicator that exceeds $\lambda_{\text{crit.}} = 1$ within the tracked 1000 turns. If not the coordinate is regarded as stable. Thus the distance of the initial coordinate to the design orbit is increased and a further tracking is performed. The transition to chaotic motion ($\lambda_n > \lambda_{\text{crit.}}$) defines the Dynamic Aperture. In Fig. 4 the result is shown for different tune combinations. A more detailed description of the analysis was presented at IPAC 2016 [6].

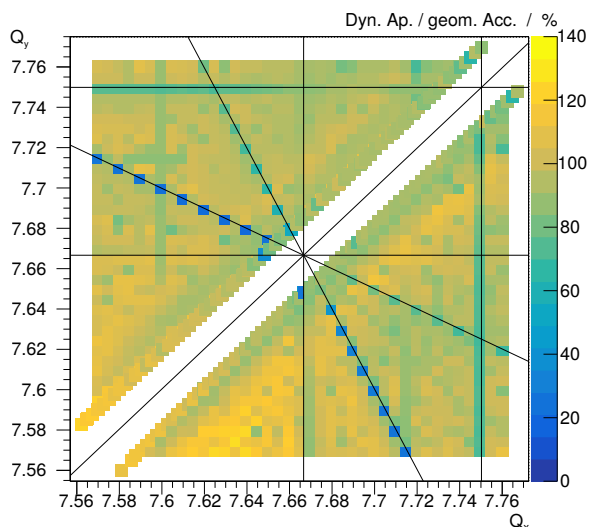


Fig. 4: The Dynamic Aperture as ratio of the geometric acceptance for different tune combinations. It is clearly visible that near the tune resonances (solid lines) the Dynamic Aperture is drastically reduced. The tunes near the coupling resonance $Q_x = Q_y$ could not be reached, due to the coupling \mathcal{A}_2 coefficient of the dipoles.

To estimate the reliability of the Dynamic Aperture, the analysis is rerun with different multipole distortions. Therefore the multipole coefficients are randomized according to their variance as estimated in the measurement. Then the whole tracking is repeated. To automate the procedure a c++ library

was written, that generates the tracking for MAD-X [7] and randomizes the multipole components. The deviation from run to run gives an estimate for the stability of the method. Usually it is less than 0.5%, if expressed as ratio of the geometric acceptance.

References:

- [1] IKP, "High energy antiproton physics, hadron structure and quark-gluon dynamics", http://www.fz-juelich.de/ikp/EN/Forschung/Beschleuniger/_doc/HESR.html
- [2] J. Hetzel, "Measurement of the Harmonic Content of the HESR Dipoles with a single Hall Probe", IKP Annual Report 2015, K - Further Contributions, Juel-4393 (2016)
- [3] L. Bottura, "Standard Analysis Procedures for Field Quality Measurement of the LHC Magnets - Part I: Harmonics", CERN Engineering Specification, LHC Project Document No. LHC-M-ES-0007 rev 1.0, 2001
- [4] S. Russenschuck, "Electromagnetic Design and Mathematical Optimization Methods in Magnet Technology", Version 3.2 (2006), ISBN: 92-9083-242-8
- [5] T. L. Rijof, F. Zimmermann, "Proceedings of the 11th International Computational Accelerator Physics Conference", WESA I3, pp. 135- 137, 2012
- [6] J. Hetzel, U. Bechstedt, J. Böker, A. Lehrach, B. Lorentz, R. Tölle "Towards Beam-Dynamics Simulations Including More Realistic Field Descriptions for the HESR", IPAC, 2016
- [7] H. Grote et al., "The MAD-X Program", Version 5.02.09

* Institut für Kernphysik 4, FZ Jülich, Germany

Theoretical Limits of Closed Orbit Corrections

F. Hinder^{a,b}

for the JEDI collaboration & the COSY Beam-Instrumentation-Group

The ambitious goal of a measurement of Electric Dipole Moments (EDMs) of elementary particles at the storage ring COSY (COoler SYnchrotron) requires a precise and reliable closed orbit correction. Simulations of the planned measurement method using an radio frequency Wien filter show, that a closed orbit correction is a crucial tool to lower systematic errors of an EDM measurement [1]. The correction of the orbit, by using a model independent Orbit Response Matrix (ORM) leads to an improvement of the measured orbit RMS down to ≈ 2 mm [2]. This fact leads to the question: Why is the orbit correction not better? Crucial points in the orbit correction are the number of corrector magnets, the number of Beam Position Monitors (BPMs) and the alignment precision of the magnetic elements. This report focuses on simulations with the mad [3] program to investigate the effects resulting in the orbit RMS. The presented results concentrate on the influence of misaligned quadrupoles, the precision of the BPMs and possible improvements are outlined. A detailed discussion of these results is given in [4].

The accelerator setup, used during the JEDI beamtimes with polarized deuterons at 970 GeV is the starting point of the simulation. All magnets and BPMs are assumed to be perfectly aligned. In addition, the BPMs measure the beam position with a perfect accuracy and resolution. With these settings the resulting orbit is centered in all elements. In a first step all quadrupoles are misaligned:

$$z = z_0 + \Delta z \quad z \in \{x, y, s, \theta, \psi, \varphi\}, \quad (1)$$

where Δz is randomly generated following the Gaussian probability function:

$$p(\Delta z) = \frac{1}{\sqrt{2\pi}\sigma_z} \exp\left(-\frac{(\Delta z)^2}{\sigma_z^2}\right). \quad (2)$$

The width of the Gaussian distribution is changed from 1×10^{-3} mm to 1.3 mm. For 10000 randomly generated misalignments, the orbit RMS values are calculated and the orbit correction is performed. The resulting distributions are shown in fig 1.

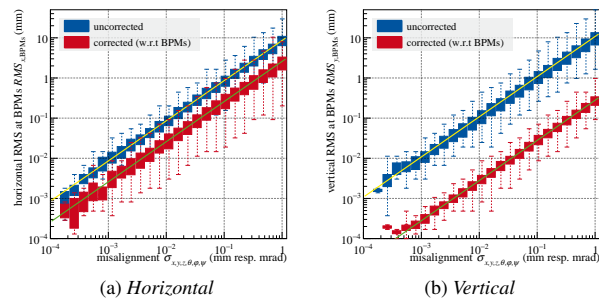


Fig. 1: The horizontal orbit RMS measured at the BPMs depending on the magnet misalignment. The uncorrected orbit RMS is shown in blue. The result of the orbit correction, with respect to the BPMs, is shown in red.

The blue graphs show the uncorrected case, whereas the red areas represent the corrected orbit. The filled error band includes 68 % of the simulated data points, whereas the error

bars represent all data points. For all four curves, a linear function is fitted against the data points:

$$RMS_{ideal} = f \cdot \sigma. \quad (3)$$

The slope f of these functions is the conversion factor between the alignment precision and the resulting orbit RMS. For both planes, the RMS value in mm of the uncorrected orbit is a factor ≈ 10 higher than the misalignment in mm resp. mrad.

The corrected orbit is obtained, by using the TSVD [4] method iteratively until the change in the orbit RMS is less than 2 %. In the vertical plane, the RMS of the corrected orbit is reduced by a factor of 50, which leads to an orbit RMS, which is 30 % of the assumed alignment resolution of the magnets. For the horizontal plane, the correction reduces the RMS only by a factor of 5. This shows, that the horizontal orbit can only be corrected to an RMS value, which is in the same range as the assumed alignment resolution.

In order to improve the RMS of the corrected orbit at COSY, the quadrupole magnets need to be aligned with a higher precision. This demanded precision is linear depending with the systematic EDM error [5].

As additional effect, the resolution of the BPMs is analysed. For this simulation, the measured beam position is smeared with a Gaussian distribution with a mean value of 0 and a width of 0.1 mm. The quadrupoles are misaligned in the same way as in the previous simulation run. The resulting curves are shown in fig. 2

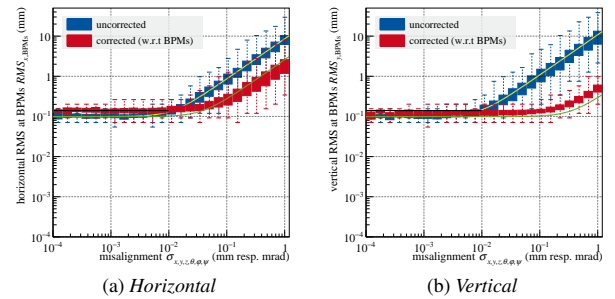


Fig. 2: The orbit RMS measured at the BPMs depending on the magnet misalignment. The uncorrected orbit RMS is shown in blue. The corrected orbit, with respect to the BPMs, is shown in red. The BPMs are assumed as perfectly aligned. The beam position measurement is simulated with a resolution of 0.1 mm.

For large misalignments, the resolution of the BPMs can be neglected and the curves are identical to the ones obtained with perfect BPMs. For alignment resolutions, which are at the same range as the BPM resolution and below, the curves diverge from the ones with perfect BPMs and converge to a minimum. This behaviour can be estimated by calculating the expectation value of the RMS [4, 6]:

$$\langle RMS_{realistic}(\lambda) \rangle = \sqrt{\frac{\pi}{2}} L_{1/2}^{(N/2-1)} \left(\frac{-\lambda^2}{2} \right) \frac{\sigma}{\sqrt{N}}. \quad (4)$$

In this equation, $L_{1/2}^{(N/2-1)}(x)$ is the generalized Laguerre polynomials and λ reads:

$$\lambda = \sqrt{\sum_{i=1}^N \left(\frac{\mu_i}{\sigma_i}\right)^2} \approx RMS_{ideal} \frac{\sqrt{N}}{\sigma}. \quad (5)$$

The ideal value RMS_{ideal} for the orbits is calculated by using the fit functions (3), obtained with ideal BPMs. The resulting expectation value of the realistic RMS is plotted above the corresponding data points as a yellow and green line in fig 2. The uncorrected data points are described very well. For the corrected ones, the data points are slightly above the expected value. This effect can be calculated as well and results in the black curve. All in all, the effect of the BPM resolution can be described analytically. The BPM resolution is the RMS limit, if the alignment of the magnets is better than the resolution of the BPMs.

In order to improve the orbit, additional elements can be installed at COSY. As a starting point for these considerations, additional BPMs at all quadrupoles as well as additional correction windings on all quadrupoles are assumed. In order to investigate the effect of such upgrades, the simulations are repeated with different scenarios:

- no upgrade (default)
- additional BPMs
- additional corrector magnets
- additional BPMs and additional corrector magnets.

For each scenario, the conversion factor between the alignment resolution and the corrected orbit RMS is calculated. The resulting factors are presented in fig 3.

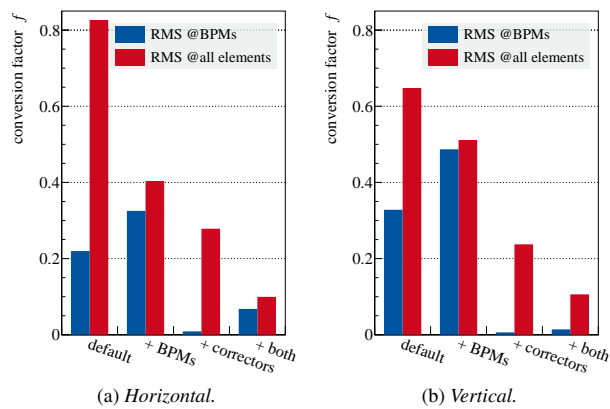


Fig. 3: The conversion factor f between the alignment resolution and the orbit RMS after correction is presented in the two diagrams for different combinations of additional corrector magnets and additional BPMs. In addition to the existing COSY systems ("default"), additional dipole windings are installed at the quadrupoles and/or additional BPMs are installed inside the quadrupoles. The RMS is calculated at the BPMs (blue), including the additional ones, and at all elements (red). The calculation is done for the horizontal and the vertical orbits.

In addition to the RMS at the BPMs, the RMS over the length of the accelerator is shown. For the existing system, the RMS

at the BPMs is clearly below the one at all elements. By upgrading the BPM system both factors come close to each other. If the two factors are close to each other, the RMS obtained at the BPMs is a measure for the RMS at all elements, which allows a estimation of the EDM limit. Additional corrector magnets lead to an improvement of the orbit at all elements. The combination of both upgrades improves the orbit RMS by a factor of ≈ 10 .

All in all the orbit RMS can be improved by a better alignment of the magnets, additional corrector windings and additional BPMs. The three possible states are ordered along their feasibility. The BPM resolution limits the orbit RMS if the alignment resolution multiplied by the conversion factor for the upgrade system fig 3 is in the same range as the BPM resolution.

During the next maintenance periods a realignment of the magnets as well as an upgrade of the BPM readout is planned, which improves the accuracy and the resolution of the BPM system. The corrected orbit after these upgrades will prove the presented behavior of the orbit RMS.

References:

- [1] M. Rosenthal, Spin Tracking Simulations Towards Electric Dipole Moment Measurements at COSY, in Proceedings 6th International Particle Accelerator Conference, IPAC15, Richmond, VA, USA (2015). <http://jacow.org/IPAC2015/papers/thpf032.pdf>
- [2] F. Hinder, B. Lorentz, M. Rosenthal and M. Simon, "Automation of the Orbit Response Matrix Measurement at COSY", in Annual Report 2015, Institut für Kernphysik Forschungszentrum Jülich, http://www.fz-juelich.de/ikp/DE/Service/Download/download_node.html
- [3] CERN - BE/ABP Accelerator Beam Physics Group, "MADX", <http://madx.web.cern.ch/madx/>
- [4] F. Hinder, "Development of Beam Diagnostic Systems for Electric Dipole Moment Measurements at Particle Accelerators", PhD thesis in preparation, 2017, RWTH Aachen University
- [5] M. Rosenthal, "Experimental Benchmarking of Spin Tracking Algorithms for Electric Dipole Moment Searches at the Cooler Synchrotron COSY", PhD thesis, 2016, RWTH Aachen University, http://collaborations.fz-juelich.de/ikp/jedi/public_files/theses/Thesis_MRosenthal.pdf
- [6] Evans, Merran and Hastings, Nicholas A. J. and Peacock, J. Brian, "Statistical distributions", third edition, Wiley, New York, 2000

a Institut für Kernphysik 4, FZ Jülich, Germany

b Physics Institute III B, RWTH Aachen University, Germany

Studies on η production in pd fusion to ${}^3\text{He}\eta$ with WASA-at-COSY*

N. Hüsken[†], F. Bergmann[†], K. Demmich[†] and A. Khoukaz[†]

The discovery of the attractiveness of the ηN potential in 1985 by Bhalerao, Haider and Liu [1, 2] inspired a wealth of research on η production off nuclei. Although originally proposed for cases of $A \geq 12$, Wilkin among others later showed that the so-called η -mesic nuclei, bound states of an η meson with a nucleus, can already occur for much lighter nuclei, like e.g. ${}^3\text{He}$ [3]. In the hunt for such states, the near threshold region of the $\text{pd} \rightarrow {}^3\text{He}\eta$ reaction was examined in great detail [4, 5, 6, 7, 8] (as can be seen in Fig.1). Away from threshold, however, the database looks more sparse [8, 9, 10, 11, 12, 13] with systematics between the various different experiments hindering a detailed study of the development of the increasingly anisotropic angular distributions with rising excess energy.

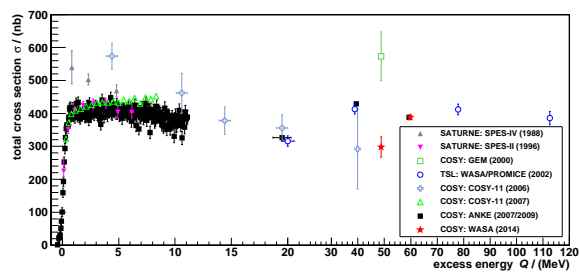


Figure 1: Total cross section data for the reaction $\text{pd} \rightarrow {}^3\text{He}\eta$ as a function of the excess energy Q . The uncertainties shown do not include systematic uncertainties resulting from an absolute normalization. The data from WASA-at-COSY (red stars) are scaled to the ANKE data point at $Q = 59.4 \text{ MeV}$. Figure taken from [13].

Our new measurement, performed in May 2014, made use of the supercycle technique of the COSY accelerator to determine detailed total and differential cross sections for the $\text{pd} \rightarrow {}^3\text{He}\eta$ reaction for 15 excess energies in the range between $Q_\eta \approx 13.6 \text{ MeV}$ and $Q_\eta \approx 80.9 \text{ MeV}$ with minimal systematics. Angular distributions are being extracted by fitting a background function based on Monte Carlo Simulations of the ${}^3\text{He}\pi\pi$ and ${}^3\text{He}\pi\pi\pi$ production channels to spectra of the final state momentum of the ${}^3\text{He}$ nuclei in the center of mass system for 25 bins of $\cos\vartheta_\eta^{\text{cm}}$. The measurement at $p_p = 1.70 \text{ GeV}/c$ ($Q_\eta \approx 61.7 \text{ MeV}$) was repeated in each supercycle and can therefore be used to study the systematics between the different parts of the beam time. As can be seen from Fig.2, where the currently unnormalized distributions were scaled to the total cross section of $\sigma = 388.1 \text{ nb}$ measured by the ANKE collaboration [9], the systematics are found to be negligible with the angular distributions of all three supercycles nicely coinciding with a previous measurement by the WASA-Collaboration [13].

*Supported by COSY-FFE, the European Union Seventh Framework Programme (FP7/2007-2013) under grant agreement n 283286 and the Deutsche Forschungsgemeinschaft (DFG) through the Research Training Group GRK2149

[†]Institut für Kernphysik Westfälische Wilhelms-Universität, 48149 Münster, Germany

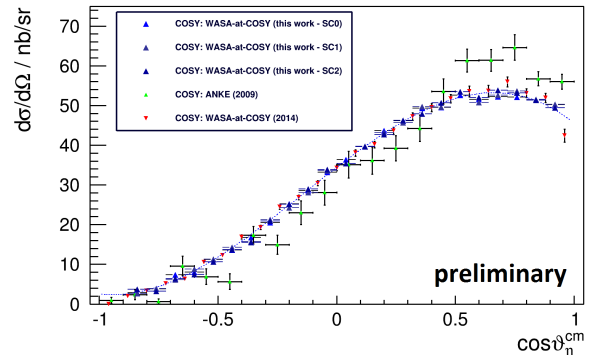


Figure 2: Angular distribution of the reaction $\text{pd} \rightarrow {}^3\text{He}\eta$ at $Q_\eta \approx 60 \text{ MeV}$. Blue upward triangles represent the current work normalized to the total cross section value of $\sigma = 388.1 \text{ nb}$ measured by the ANKE experiment [9], which is shown as green upward triangles. Also shown are the data from [13] as red downward triangles.

At the same time, there is an apparent disagreement with the differential cross sections from the ANKE measurement visualizing the impact of systematics between different experiments on a comparison between angular distributions. In that regard, our measurement will enable a study on the energy dependence of the differential cross sections with unprecedented precision due to the high statistics and the negligible systematics between the measurements at individual excess energies. Such studies would greatly aid in the development of theoretical models trying to describe the production process at higher excess energies, as the need for new high energy data was recently emphasized [14].

Both the total and differential cross sections for all 15 excess energies will be available soon, while other detailed studies of meson production in proton deuteron fusion (e.g. single- or double-pion production) are also being prepared.

References

- [1] R.S. Bhalerao *et al.*, *PhysRev. Lett.* **54**, 865 (1985).
- [2] Q. Haider *et al.*, *Phys. Lett. B* **172**, 257 (1986).
- [3] C. Wilkin, *Phys. Rev. C* **47**, R938(R) (1993).
- [4] T. Mersmann *et al.*, *Phys. Rev. Lett.* **98**, 242301 (2007).
- [5] J. Smyrski *et al.*, *Phys. Lett. B* **649**, 258 (2007).
- [6] J. Berger *et al.*, *Phys. Rev. Lett.* **61**, 919 (1988).
- [7] B. Mayer *et al.*, *Phys. Rev. C* **53**, 2068 (1996).
- [8] H.-H. Adam *et al.*, *Phys. Rev. C* **75**, 014004 (2007).
- [9] T. Rausmann *et al.*, *Phys. Rev. C* **80**, 017001 (2009).
- [10] R. Bilger *et al.*, *Phys. Rev. C* **65**, 044608 (2002).
- [11] R. Bilger *et al.*, *Phys. Rev. C* **69**, 014003 (2004).
- [12] M. Betigeri *et al.*, *Phys. Lett. B* **472**, 267 (2000).
- [13] P. Adlarson *et al.*, *Eur. Phys. J. A* **50**, 100(2014).
- [14] N.G. Kelkar *et al.*, *Rep. Prog. Phys.* **76**, 066301 (2013).

Development of a Track Reconstruction Algorithm for the Panda Forward Tracking System

F.Kibellus, G.Sterzenbach

The forward tracking system of the PANDA Detector consists of six stations (FTS1 – FTS6) aligned along the beam axis. Each station contains 4 double layers of straw tubes perpendicular to the beam. The straw tubes in layer 1 and 4 are vertical (parallel to the y-direction) layer 2 is tilted by 5 degrees to the right layer 3 is tilted 5 degrees to the left. The whole system covers an angle of $\pm 10^\circ$ horizontally and $\pm 5^\circ$ vertically with respect to the beam direction. The stations FTS3 and FTS4 are located in the magnetic field of the forward spectrometer's dipole magnet.

The algorithm works in five stages. When a particle traverses a double layer of straw tubes it will usually hit one straw tube in each layer. There are exceptions, if a particle hits only one tube on the edge of a double layer or when a tube does not respond (i.e. a signal below threshold). Ambiguities can emerge, when adjacent tubes in the same layer fire. In the first stage of the algorithm each double layer is scanned for such pairs of hits. Single hits are recorded for use in a later stage, ambiguous hit pattern are passed to the next stage as a set of pairs covering all possible combinations.

In the second stage, drift time is taken into account. The drift time in a tube defines an isochrone radius around the central wire inside the drift tubes. It is measured against a start time t_0 , which can be taken from another sub-detector of PANDA. Having the isochrone radius of two tubes one can construct four tangents (two inner and two outer) defining candidates for straight line tracks through the given pair of tubes projected to the coordinate plane perpendicular to the tubes axis. Only one of this 4 candidates represents the true track. The other 3 have to be filtered out by the following stage. There is no means to fix the coordinate along the tube axis in this stage. This is also done in stage 3.

The third stage combines the results of all 4 double layers within one station. Combination of layer 1 and 4 (the parallel double layers) allows to purge wrong candidates of projected tracks. This is achieved by comparing all possible combinations of track candidates of layer 1 and 4. If the angle between two candidates exceeds a given threshold the combination is canceled from the list. For the remaining candidates the intersection point of the track with the entrance plane of the module is computed and each combination for which the distance of the intersection points exceeds a given threshold the combination is again canceled.

The list of track candidates is now given by the candidates calculated with layers 1 and 4 and the candidates of layers 2 and 3. Including the tilted layers introduces the 3rd dimension into consideration. The projected tracks can be used together with the direction of the tube axis to span a plane in which the 3-dimensional track must be located. Track candidates are then the intersection lines of pairs of planes taken from the combined candidates from double layers 1 and 4 together with planes from layer 2 or layer 3 respectively, or of intersections

of planes from layer 2 with planes from layer 3. Again pairs of candidates are compared using the same similarity measure as before (i.e. angle between two candidates and distance of intersection points in a reference plane).

As mentioned before two stations are located within the dipole field of the forward spectrometer. In these Stations tracks are no longer straight lines but helix lines which can be seen as superpositions of a circular movements in the x-z plane together with linear movements in y-z-plane. For each double layer the program uses still the linear approach, but the combination of double layers works now using a way-follower propagating each track candidate from one layer to the next searching for the best continuation.

At the end of stage 3 the resulting track candidates of each station are refitted to account for the more complete data for each individual track.

In stage 4 track candidates of the different stations are combined using the same metric as for the combination of double layers within the stations. Again the stations, which lie inside the magnetic field, need a special treatment using the way-follower.

In the last stage the single left over hits are integrated into the nearest tracks. The maximum allowed distance to the track is of course limited by the geometry of the straw tubes.

The algorithm has been tested using DPM / Monte Carlo data. The tests were used to fix the threshold parameters in the different similarity analysis and finally to get impression of quality of the code. Without further limitations 61,58% of all tracks in FTS have been found. 33.66% were clean and complete. 15.4% were complete but were contaminated with hits from other tracks. 6.9% were incomplete (some hits not found) but clean, and 5.62% were incomplete and contaminated. 38% were not found.

Analyzing the reasons for incompleteness and contamination of reconstructed tracks, it turned out that tracks with less than 6 hits in FTS could not be fully reconstructed. Events with a high number of tracks were difficult to analyze because of the increasing number of ambiguities. Tracks the low momentum tend to produce narrow helix paths which result in hit pattern which cannot be resolved into separate lines. With some limitation reflecting these arguments (neglecting tracks with less than 6 hits, neglecting events with more than 6 tracks in FTS, and neglecting tracks with $P < 0.3 \text{ GeV}/c$ the statistic of reconstruction quality changed to 77.54% found tracks, 43.62% clean and complete, 17.43%, contaminated but complete, 8.67% clean but incomplete, and 7.83% contaminated and incomplete.

[1] F. Kibellus, Bachelorarbeit "Entwicklung eines Spurfindealgorithmus für das Forward Tracking System des PANDA-Detectors" Fachhochschule Aachen, FB: Medizintechnik und Technomathematik August 2016.

Study of dp breakup reaction in the Forward Detector

B. Kłos¹ and I. Ciepał²

An experiment to investigate the $^1\text{H}(d,pp)n$ breakup reaction using a deuteron beam of 340, 380 and 400 MeV and the WASA detector has been performed at the Cooler Synchrotron COSY-Jülich. The main goal was to study various aspects of few-nucleon system dynamics in medium energy region, with a particular emphasis on investigation of relativistic effects and their interplay with three nucleon force (3NF).

Currently, the data analysis is focused on the proton-proton coincidences registered in the Forward Detector with the aim to determine the differential cross section on a dense angular grid of kinematical configurations defined by the emission angles of the two outgoing protons: two polar angles θ_1 and θ_2 (in the range between 4° and 18°) and the relative azimuthal angle ϕ_{12} . The precise energy calibration, PID, normalization and efficiency studies, and their impact on the final accuracy of the result, was determined during last year. The breakup observables can be calculated below the pion production threshold using modern pairwise nucleon-nucleon NN interactions (so-called realistic potentials), combined with model of 3N forces [1]. Moreover, the two- and three-nucleon interactions can be modeled within the coupled-channel (CC) framework by an explicit treatment of the Δ -isobar [2]. The calculations in relativistic regime have recently been performed for the $^1\text{H}(d,pp)n$ breakup reaction at the beam energies of 340, 380 and 400 MeV [3], predicting very large relativistic effects at these energies.

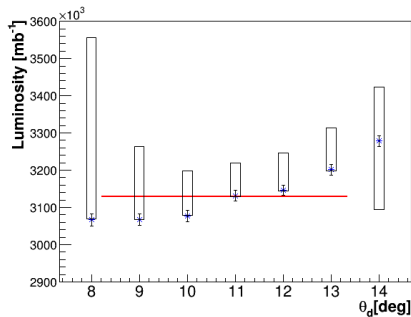


Fig. 1: The luminosity calculated at several values of the deuteron scattering polar angle. The solid line corresponds to the weighted average of four results with the smallest systematic errors (shown as boxes). The error bars represent statistical uncertainties.

To obtain differential cross section, the luminosity is determined on the basis of the number of the elastically-scattered deuterons registered at a given θ angle and the known cross section for elastic scattering at this angle. Systematic scatter of the data in this energy region motivated normalization based on theoretical calculations with the CDBonn potential and TM99 3NF. It has been shown that they provide a very good description of the data (in the angular range of interest) in the energy region between 108 and 200 MeV/nucleon. After selection of deuterons registered in the Forward Detector and energy calibration, the correct energy vs angle relation for elastically scattered deuterons was obtained. The values of the luminosity obtained for several angles of the deuteron scattering is shown in Fig. 1. The boxes represents system-

atic errors due to normalization either to calculated or measured cross section and/or uncertainty related to subtraction of the proton background. The results for angles between 9° and 13° represent good consistency within their systematic uncertainties. Determination of luminosity on the basis of data collected with much less restrictive trigger confirmed the compatibility between obtained values at the level of a few percent. The number of deuterons was corrected by efficiency factors, determined on the basis of Monte Carlo simulation. Including detector acceptance and all cuts applied in the analysis, the efficiency for registering and identifying elastically scattered deuterons is about 80%.

An example of the normalized experimental breakup event rate obtained for a sample kinematical configuration at the beam energy of 340 MeV is presented in Fig. 2. The result indicates that the data for this configuration are sensitive to Coulomb effects.

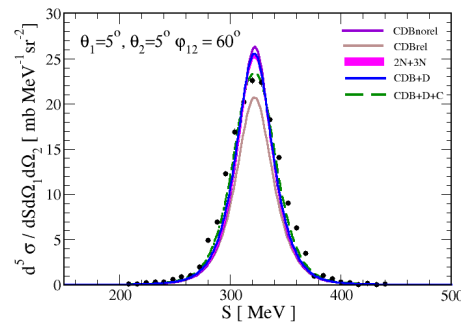


Fig. 2: Differential cross section distribution as a function of kinematical variable S obtained for chosen kinematical configuration (specified in the panel) of the breakup reaction at 340 MeV beam energy. The data are compared to: calculations based on realistic potentials: 2N complemented with the TM99 3NF and the realistic AV18 potential combined with the Urbana IX (the band called 2N+3N; the calculations within the coupled-channel approach with the CD Bonn potential (CDB), with the CD Bonn+ Δ potential without (CDB+D) and with (CDB+D+C) the Coulomb force included; relativistic calculations with CD Bonn potential (CDBrel).

We acknowledge support by the Polish National Science Center through grant No. 2012/05/E/ST2/02313 and by the FFE funds of the Forschungszentrum Jülich.

¹Institute of Physics, University of Silesia, PL-40007 Katowice, Poland

²H. Niewodniczański Inst. of Nuclear Physics PAN, PL-31342 Kraków, Poland

References:

- [1] W. Glöckle, H. Witała, D. Hübner, H. Kamada, J. Golak, Phys. Rep. **274** (1996) 107.
- [2] A. Deluva et al., Phys. Rev. C **72** (2005) 054004.
- [3] H. Witała, private communication.

A read-out system for the PANDA MVD prototypes: development and results

Alessandra Lai

Introduction The PANDA experiment will play a key role at the upcoming Facility for Antiproton and Ion Research (FAIR) in Darmstadt. Exploiting proton-antiproton interactions, its scientific program addresses fundamental questions of QCD. The Micro Vertex Detector (MVD) is the sub-detector system closest to the interaction point. It consists of four barrel layers in the central part and six disk layers in the forward direction. It uses two different kind of silicon detectors as sensitive elements: hybrid pixel detectors and double-sided strip detectors. Two different types of front-end ASICs are under development for the MVD: the Torino Pixel ASIC (ToPix) and the PANDA Strip ASIC (PASTA). The ToPix ASIC is a chip developed for the readout of silicon pixel detectors. The final version of a single chip reads out more than 10,000 pixels with pixel dimensions of $100 \mu\text{m} \times 100 \mu\text{m}$. In addition to the spatial information, the deposited energy in a pixel and the time when the pixel was hit are measured with a precision better than 10 ns [1]. The PASTA chip is designed to read out silicon strip sensors. Like the ToPix ASIC, it measures the position, the deposited energy and the time of a hit. Both are designed to transmit untriggered data at a rate of hundreds of Mb/s and to handle the expected hit rate in hot spots of the detector.

A test system capable to handle these high rates is therefore needed. It should be flexible to test different kinds of front-end electronics and easy to adapt to new prototypes. Therefore, an FPGA-based system is the ideal candidate. Suitable firmware and a software framework are thus under development at Forschungszentrum Jülich.

The Jülich Digital Readout System The main components of the Jülich digital readout system (JDRS) are an evaluation board from Xilinx (ML605), hosting a Virtex-6 FPGA and a custom made readout board that hosts the device under test (DUT), i.e., the chip. A network link allows the connection from the evaluation board to a PC. The logic scheme for the FPGA, called firmware, is written in VHDL (Very high speed integrated circuit-Hardware Description Language). A software called MVD Readout Framework (MRF) [2], based on C++ has been developed with the idea of maximum modularity in mind. It is a library that collects functions that allow access to the elements of the readout chain.

To facilitate the access to the readout elements, a Qt-based graphical user interface (GUI) has been developed. A schematic view of the system is shown in Figure 1. For more details see [3].

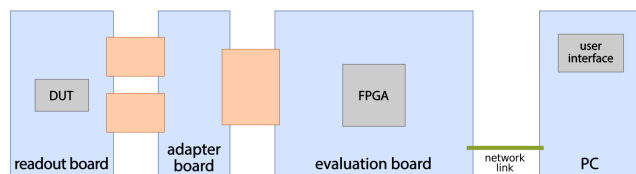


Fig. 1: Main components of the readout chain for the PANDA MVD ASICs.

Adaptation for the PASTA ASIC The key idea for the latest implementation of the JDRS was to keep the system modular, in order to enhance the reusability of the single parts. The development of the JDRS was so far focused on the ToPix ASIC [3]. Since recently, the first version of the PASTA ASIC was received [4], some efforts were made to adapt the system to the new prototype. Thanks to the modularity of the JDRS, a significant amount of both the software and the firmware can be used without any modification, e.g., almost all the MRF functions (except the ones specific for the chip structure) and the ethernet connection module.

PASTA receives a default configuration as it is powered on, but it is important to have the possibility to edit this configuration from the user interface. Dedicated modules were implemented to send and read back a global configuration (i.e., that is sent to all the channels) and a local configuration (i.e., sent on a channel by channel basis).

Once the chip is properly configured, the system is ready to receive a continuous stream of 8 bit/10 bit encoded data coming from the ASIC. As a first step, the data stream is 10 bit/8 bit decoded on the FPGA and stored into a FIFO (first in first out) buffer. It is then passed on to the software to be converted into a user-defined format (e.g. ASCII or Boost serializer) and stored in a user-defined memory location. In order to obtain usable objects for the analysis of the performances, the data stream goes then through another online decoding procedure. The JDRS offers the possibility to filter the data transmitted over the ethernet connection at the firmware level, in order to reduce the load on the line and the processing time, if necessary.

The GUI widget responsible for the communication with the FPGA module, which receives data from the ASIC, and for the data handling is shown in Figure 2.

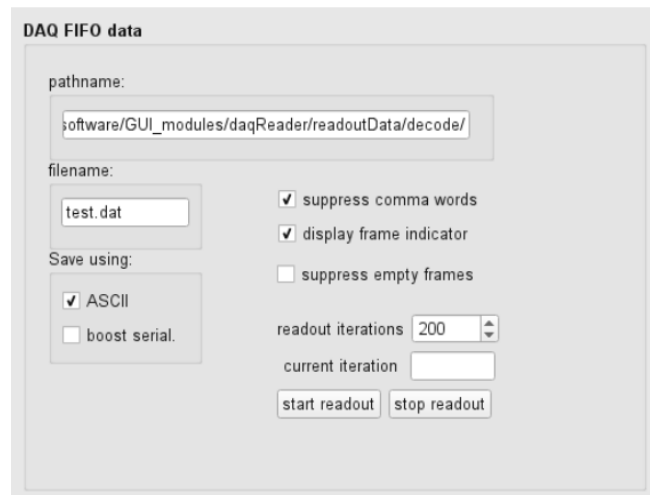


Fig. 2: GUI widget for data handling preferences.

Before studying the performances of the ASIC under a particle beam, it is important to characterize it in a laboratory environment. Therefore a section of the JDRS is dedicated to

handle the configuration of a test pulse, generated on-chip. With this module, the user can specify parameters such as pulse length and width.

To be able to test the behavior of the channels individually, a dedicated software module has been designed. In order not to have the user switch from one channel under test to the other and change the configuration parameter by hand, the idea was to make the procedure automatic. In Figure 3 one can see the GUI widget correspondent to this module. Here the user can choose what kind of test pulse will be produced, which range of channels will be enabled sequentially, and up to two configuration parameters to sweep. Once the scan has started, the selected channels will be enabled one by one. For each of these, a test pulse with parameters specified in the dedicated widget, as mentioned above, will be injected.

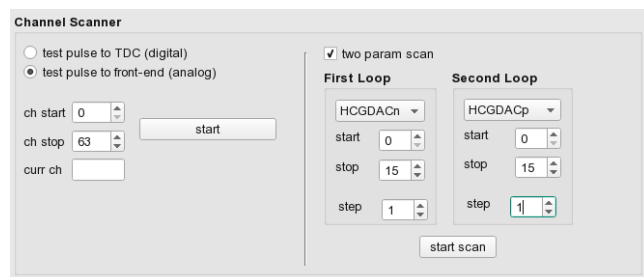


Fig. 3: GUI widget to automatize the procedure to test the channels individually.

Performance Test With the adaptations that have been illustrated in the previous paragraph, the JDRS is now ready to be used to start a campaign of measurements with the aim of a full qualification of the PASTA ASIC. This process is still ongoing so hereafter are some results that should be considered as qualitative.

A set of tools based on ROOT has been developed to analyze the data in an offline mode.

Figure 4 shows the time over threshold as a function of the pulse amplitude of the incoming signal, for a specific channel. The trend is linear as expected and the data points are affected by a very small statistical uncertainty.

The histogram in Figure 5 shows the number of registered events as a function of the global threshold (i.e., the same threshold value is applied to all the channels), at fixed pulse amplitude. For this kind of function, ideally one would expect to have a step function, with zero events at high thresholds value and 100% of the events for low threshold values. Effectively, what one observes is the superimposition of this behavior with a gaussian smearing due to the noise. Provided a proper calibration of the DAC (digital to analog converter), the noise level can be estimated in terms of equivalent noise charge, by fitting this distribution with a convolution of a step function with a Gauss error function

$$F(x) = \frac{n}{2} \left(1 + \operatorname{erf} \left(\frac{x - \mu}{\sqrt{2} \cdot \sigma} \right) \right)$$

where the error function is

$$\operatorname{erf} \left(\frac{x - \mu}{\sqrt{2} \cdot \sigma} \right) = \frac{2}{\pi} \int_0^x e^{-t^2} dt$$

Here n is a normalization factor, μ represents the mean, and σ represents the noise.

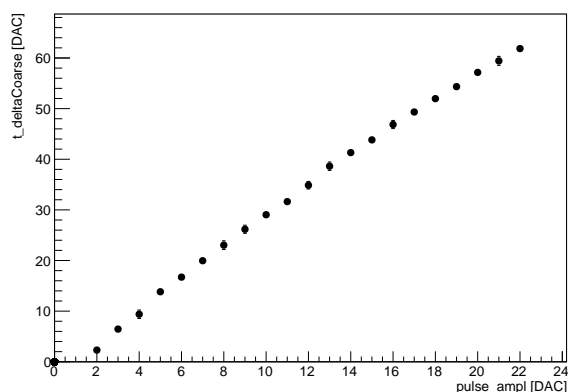


Fig. 4: Time over threshold as a function of the pulse amplitude of the incoming signal.

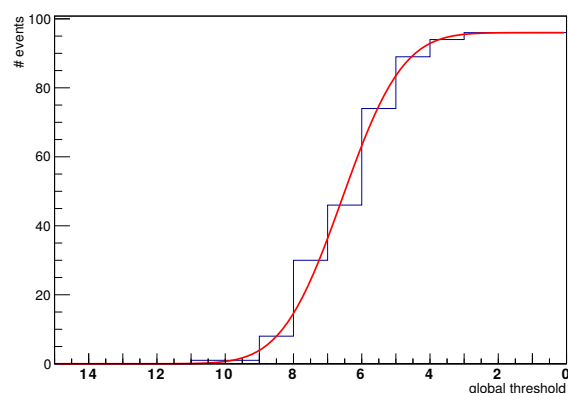


Fig. 5: Global threshold scan.

Conclusions and Outlook The development of the JDRS as a flexible and versatile readout system for the prototypes of the PANDA MVD is ongoing. Some preliminary results confirm the correct behavior of the implemented software and firmware, as well as the basic working principle of the latest prototype: the PASTA ASIC designed to read out the strip part of the MVD.

Since at the moment a set of tools for the analysis is available, more thorough performance tests will be carried out in the next future. Moreover, some new features will be implemented in the readout framework.

References:

- [1] The PANDA Collaboration, *Technical Design Report for the: PANDA Microvertex Detector*. (2011) <http://arxiv.org/abs/1207.6581>
- [2] M. Mertens, *PhD thesis* <http://www-brs.ub.ruhr-uni-bochum.de/netahtml/HSS/Diss/MertensMariusC/>
- [3] A. Lai, *A test system for the electronic components of the PANDA Micro Vertex Detector, Annual Report 2015 - Individual Contribution*.
- [4] A. Goerres, *Developing a Free-Running Readout ASIC for the MVD Strip Sensors, Annual Report 2014 - Individual Contribution*.

Dalitz Plot Analysis of $\eta \rightarrow \pi^+\pi^-\pi^0$ with CLAS

Daniel Lersch for the CLAS collaboration

The decay width Γ of the isospin violating decay $\eta \rightarrow \pi^+\pi^-\pi^0$ is proportional to Q^{-4} with:

$$Q^2 = \frac{m_s^2 - \hat{m}^2}{m_d^2 - m_u^2}, \quad \hat{m}^2 = \frac{1}{2}(m_u + m_d) \quad (1)$$

Therefore, the investigation of this decay allows to access the ratio of quark masses. One possibility of determining the decay width Γ is given by the Dalitz Plot analysis, which is defined by the two dimensionless variables:

$$X = \sqrt{3} \frac{T_{\pi^+} - T_{\pi^-}}{T_{\pi^+} + T_{\pi^-} + T_{\pi^0}} \quad (2)$$

$$Y = 3 \frac{T_{\pi^0}}{T_{\pi^+} + T_{\pi^-} + T_{\pi^0}} - 1 \quad (3)$$

where T_i refer to the kinetic energies of the decay particles in the η rest frame. Using these variables leads to the following parameterisation of the decay width:

$$\frac{d^2\Gamma}{dXdY} \propto (1 + aY + bY^2 + cX + dX^2 + fY^3 + \dots) \quad (4)$$

where a,b,c,d,e, and f are fit parameters. Due to C-conservation, all parameters connected to odd powers of X (i.e. c and e) are supposed to be zero, which has also been approved by the latest measurements [1, 2, 3]. Comparison between experimental and theoretical estimations of the Dalitz Plot parameters show strong tensions with respect to the a and b values [1, 2, 3, 5, 6]. The WASA-at-COSY results [2] were used for a partial wave analysis [4] and the Q-value has been directly determined [4]: $Q = 21.4 \pm 0.4_{stat}$.

mass: $M(\pi^+, \pi^-) \leq m_\eta - m_{\pi^0}$. Step (i) is used to suppress background from competing reactions (e.g. $\rho \rightarrow \pi^+\pi^-$) and to improve the resolution of the particle momenta. Step (ii) helps to reduce contributions from the reaction $\omega \rightarrow \pi^+\pi^-\pi^0$ which has the same final state topology and therefore passes step (i).

Fig. 1 shows the one dimensional Dalitz Plot distribution (black points) after reconstructing $\approx 700k$ $\eta \rightarrow \pi^+\pi^-\pi^0$ events. Each global bin i corresponds to a pair X and Y within the Dalitz Plot. The data points in Fig. 1 have been corrected for background and reconstruction efficiency. The red curve in Fig. 1 corresponds to a fit of Eq. 4, where the parameters c and e have been fixed to zero. A comparison between the black points and the red curve show a slight mismatch at global bins $i \in [74, 76]$, which is under current investigations.

The study of effects related to data analysis are ongoing such that systematic errors will be included in a next step. Furthermore, a partial wave analysis will be performed in order to determine the quark mass ratio Q directly.

References:

- [1] The KLOE collaboration, *JHEP*, 019, (2016)
- [2] The WASA-at-COSY collaboration, *Phys. Rev.*, C90(045207), (2014)
- [3] The KLOE collaboration, *JHEP*, 05, (2008)
- [4] Peng Guo et al., *Phys. Rev.*, D92(05016), (2015)
- [5] J. Bijnens and K. Ghorbani, *JHEP*, 11, (2007)
- [6] S-P. Schneider et al., *JHEP*, 028, (2011)

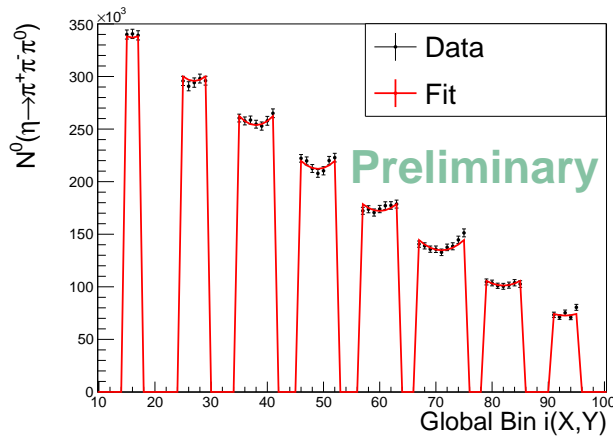


Fig. 1: One dimensional Dalitz Plot (black points) obtained from the analysis of the CLAS $\gamma p \rightarrow p\eta$ data set.

A third measurement of this decay has been performed with the CEBAF Large Acceptance Spectrometer (CLAS), located at the Thomas Jefferson National Laboratory. The mesons were produced via the photo-induced reaction: $\gamma p \rightarrow p\eta[\eta \rightarrow \pi^+\pi^-\pi^0]$.

The event reconstruction consists of two basic analysis steps: (i) A kinematic fit, where events with a fit probability less than 10% are rejected and (ii) A limitation of the two pion

Low-Noise BPM Preamplifier for the HESR

S. Merzliakov, C. Böhme, V. Kamerzhiev

Abstract The design of the preamplifiers for the Beam Position Monitors in the High Energy Storage Ring is described. The circuit includes cold resistance at the input [1] and double feedback loops (negative and positive). The device has 500 kOhm input impedance, 26 dBV gain, 80 MHz bandwidth and $1,4 \text{ nV}/\sqrt{\text{Hz}}$ input noise at 10 MHz.

Introduction For beam position measurements at the FAIR accelerator facility the Libera Hadron beam position processors from Instrumentation Technologies, Slovenia will be used [2]. The Hadron preamplifier (HPA) (also supplied by Instrumentation Technologies) though primarily envisaged for the SIS100 machine can also be used in the HESR. However, a FET-input trans-impedance preamplifiers described in this paper will be used in the HESR instead of a transformer based solution envisaged for the SIS100. The measurement method with capacitive pickups and main requirements to preamplifiers were determined in [3]. The BPM preamplifier benefits from modern components and utilizes novel design approaches. A similar design will be used within the BPM upgrade project and to readout the Rogowski coil pickups at COSY [4].

Preamplifier with double feedback The simplified schematic of the preamplifier is presented in Fig. 1. It is possible to distinguish the following main parts.

- Input stage with double FET (Q1 and Q2), as recommended in [3] for noise minimization. Gain and noise of these transistors define the noise parameters of the entire preamplifier.
- Main amplifier (U1) utilizes the AD4817 operational amplifier (OP). The parameters of this OP (frequency bandwidth beyond 1 GHz and noise $4 \text{ nV}/\sqrt{\text{Hz}}$ and $2,5 \text{ fA}/\sqrt{\text{Hz}}$) benefit the design. Its high gain and wide bandwidth reduce the influence of dispersions characteristics of the FET transistors on the preamplifier parameters.
- Two feedback loops, individual for each input transistor, define the gain of the preamplifier (R2-R6 and R3-R7). This approach increases the number of passive components. However, it makes the tedious pairwise matching of individual FETs unnecessary.
- Output buffer U3 based upon an AD8011. OP features excellent gain flatness (0,1 dB at 25 MHz) and small phase error, so Analog Devices recommended it for buffering high speed ADC (our case).
- U2 OP (also an AD8011) is used in the circuit as part of the cold resistance termination. It also stabilizes the zero offset at the analog output of the preamplifier.

Gain and cold resistance Detailed analysis of the preamplifier with cold resistance is presented in [2]. A BPM preamplifier of this type is used in the ELENA project [5]. Briefly, this device can be described as a FET-input fixed gain amplifier, that has an additional negative resistive feedback loop from the its output to its input. From theory, the input impedance of the preamplifier, in this case, is the value of the resistor in the feedback loop, divided by the gain factor of

the amplifier. The implementation of cold resistance reduces the thermal noise of the feedback resistor R14. However, the SPICE simulation shows that the noise reduction occurs in the frequency range up to 1 MHz. Given the values shown in Fig. 1 the preamplifier gain amounts to 20 dBV and the input impedance to 500 kOhm (10 MOhm of R14 divided by the gain value). Power of noise density at 100 kHz at the output of the preamplifier is $2,5 \text{ fV}^2/\text{Hz}$. Without "cold" feedback loop this value increases up to $15 \text{ fV}^2/\text{Hz}$.

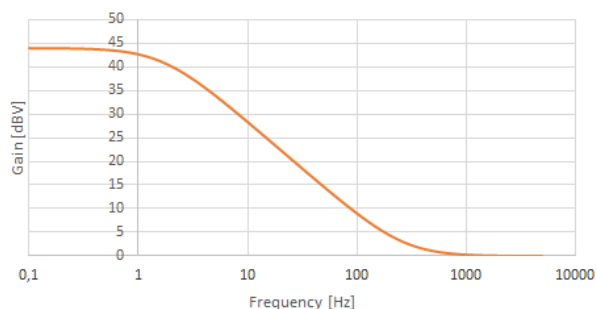


Fig. 2: Gain versus frequency at test point U2.

Offset stabilization with cold resistance termination

Additional benefits from cold resistance part of the preamplifier are automatic setting of working points of transistors Q1 and Q2 to 7,5 mA and offset stabilization at the output to the level of a few mV. For this purpose, an additional circuit C3-R13 was introduced to the design. This addition increases the DC-gain of U2 up to 44 dBV and then decreases it to 0 dBV at 2 kHz (see Fig. 2). With this shape of U2 gain, any slow variation from zero at the output of U1 will be compensated by the negative feedback loop through cold resistance from output of U2 to gates of input FETs. The attenuation factor is 70 dB (44 dB of U2 plus 16 dB of the main amplifier).



Fig. 3: A photograph of the HESR BPM preamplifier prototypes.

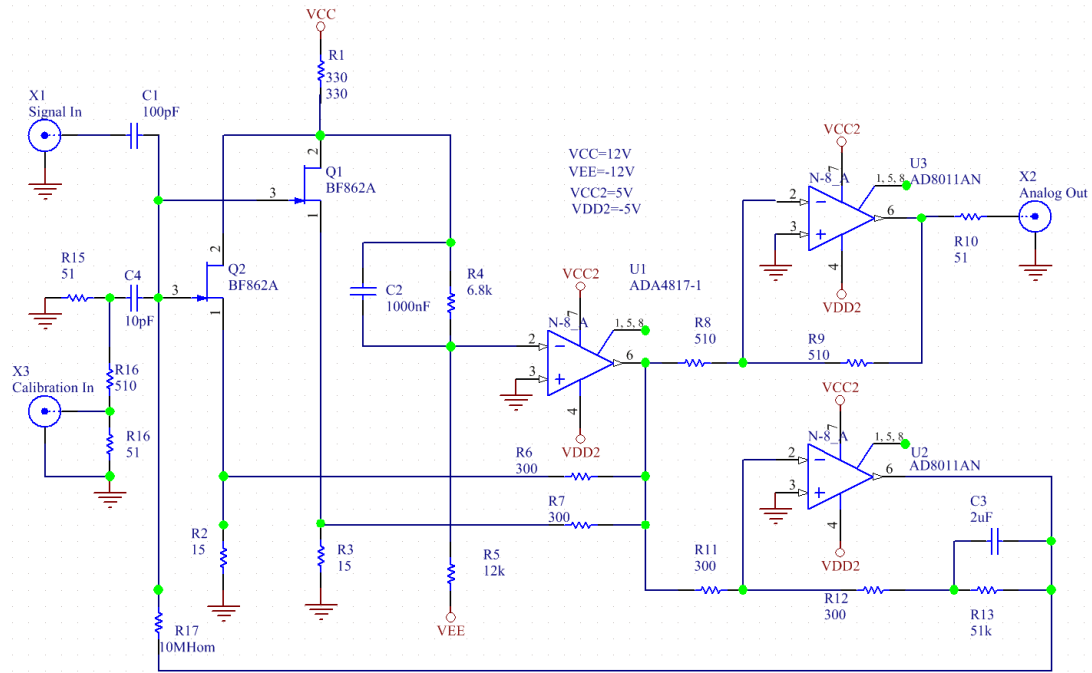


Fig. 1: Simplified electrical schematic of the preamplifier.

Specification

Input impedance	500 k Ω
Input impedance of the calibration input	50 Ω
Output impedance	50 Ω
Gain	20 dBV / 6 dBV (switch)
Frequency bandwidth	3 kHz-80 MHz (-3dB)
Output range	$\pm 1,2V$ at 50 Ω
Temperature coeff.	0.05% / $^{\circ}C$
Input noise	1,4 nV / \sqrt{Hz}
Supply voltages	$\pm 5 V$ and $\pm 12 V$

References:

- [1] E.Gatti, P.F. Manfredi, Signal coupling a semiconductor detector to a cold resistance preamplifier through a cable or a delay- line transformer. IREE Trans. on Nucl. Sci., vol. NS-25, No.1, Feb. 1978, pp.64-74.
- [2] Libera Hadron Beam Position Processor. User Manual. Instrumental Technologies 2015.
- [3] J. Biri, M. Blasovszki, J. Gigler, I. Mohos, K. Somlai, Zs. Zarandi KFKI-MSzKI, POB 49, H-1525 Budapest, Hungary.
- [4] F. Hinder, H. Soltner, F. Trinkel, Commission of a Magnetostatic Beam Position Monitor, IKP Annual Report 2015
- [5] Marco Bau, Marco Ferrari, Vittorio Ferrari, Lars Sjøby, Ricardo Marco-Hernandez, Fleming Pedersen, Low-noise Charge Preamplifier for Electrostatic Beam Position Monitoring at the Elena Experiment. Procedia Engineering 120 (2015) 1229-1232.

The EDM polarimetry detector development at COSY

F. Müller^{a,b}, D. Mchedlishvili^{a,c}, I. Keshelashvili^a and A. Kacharava^a for the JEDI collaboration

Introduction

In this contribution we overview the progress done since the first beam tests at COSY using the LYSO modules for the EDM polarimetry detector development [1]. The results of the investigation of the fundamental properties of the LYSO crystals are reported in annual report 2015.

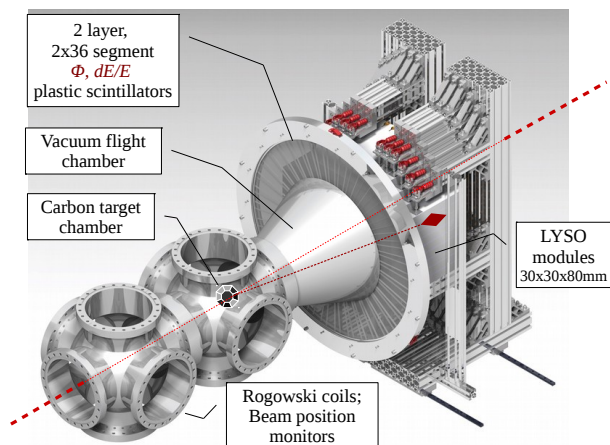


Fig. 1: Detector concept for the final detector setup.

The figure 1 shows the JEDI polarimetry concept based on LYSO novel scintillating material. The detector is modular so that it can be assembled step by step with different configurations and number of crystals. It can also be split and used at various places inside the storage ring to measure the polarization of the beam. The mechanical part of the detector is constructed with standard building materials which makes it easy and cost-effective to build.

To realize this project, we have already made the first steps by testing LYSO crystals using proton beam of 100 and 150 MeV kinetic energy to see the detector response. After that we shoot LYSO modules with deuteron beam of five different energies between 100 and 270 MeV. The essential characteristics we learned from the first tests are:

- The light output from LYSO scintillating material was very linear up to 270 MeV deuteron energy loss. In another word, the material has a linear respond within required energy range.
- The deuteron identification efficiency dropped up to 70% at 270 MeV deuteron kinetic energy. The main problem is the break-up reactions within the crystal. The rest of the spectrum was also recorded and compared to the GEANT4 simulation results.
- The deposited energy resolution vs incoming deuteron energy has been studied using the dual channel photomultiplier tube [2] and silicon photomultiplier [3]. Both modules demonstrated energy resolution as good as below 1% at 270 MeV deuteron energy. The dominant part this effect must be coming from the scintillating material.
- The crystals for these tests were provided by two different vendors: Saint-Gobain [4] and EPIC Crystals [5].

The results were compared, and the decision was made in favor to European provider due to warranty and safety conditions. Other than that, both crystals had very similar performance and prices. They were also substantially lower in price than three other companies we request the offer.

- Using the horizontal rotation (relative to COSY beam) of the split crystal (which is described in the previous proposals), the Bragg peak of the LYSO material for the 270 MeV deuterons has been reconstructed. The test shows that the beam is absorbed within the first 60 mm. So with this information, the length of new crystals are reduced from 100 mm to 80 mm. With 80 mm crystal length, one can eliminate radiation damage due to Bragg-peak simply flipping the crystal along the beam axis.
- In the second version of LYSO modules, the crystals have cut off edges from the both ends. In opposite, the holding structure made of aluminum has the fixator teeth. This guarantees the steep construction and fixed relative orientation between crystal and photosensor. The packaging and the spring load configuration is also improved (see figure 2).
- The readout of the modules during the last beam test has been made using 12-bit high linearity charge integrating ADC [6] and 14-bit 250 MS/s flash ADC [7]. The results were compatible, and for the detailed studies, the flash ADC with full signal shape recording have been used. The data has been analyzed and monitored online and finalized in more careful way offline.
- In parallel, we also tested the SiPM readout of the 5 mm thick plastic scintillator veto counters and developed OpAmp based preamplifier. This experience will be used for the designing of the dE/E plastic scintillator wall in front of the calorimeter.

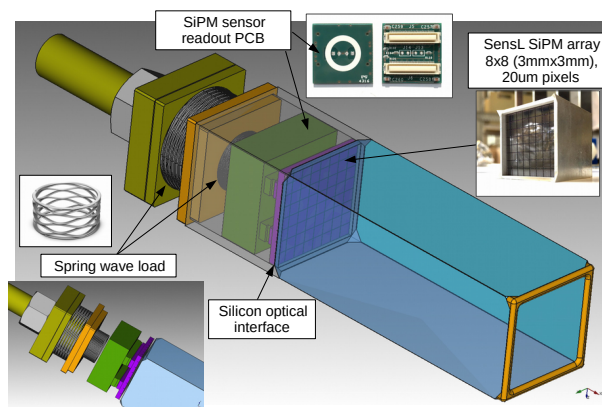


Fig. 2: The second version of LYSO polarimeter module with SiPM readout.

Setup used in recent beam-time

The experimental information collected during the measurements in lab first, and then at COSY, allowed us to construct

setup, with the modular assembly based on a standardized aluminum support structure shown on Fig. 3. The setup comprises 24 LYSO modules divided into two arms, each consisting of 12 calorimeter modules (2 x 6 crystals). The LYSO crystals were obtained from the company Saint-Gobain (SG). Such a construction allows us to build the polarimeter with a different number of crystals and with a different geometrical configurations.

The measurements taken at COSY during 2016 with various type solid targets (with different thickness of 5 to 10 mm), used a slowly extracted polarized deuteron beam at the BIG KARL experimental area. The goal was to investigate and optimize the performance of the DAQ and new SiPM based LYSO modules, with the aim to extract differential cross sections and vector analyzing powers for deuteron induced elastic reactions on different targets. With the help of specific target revolver, the above-mentioned physical parameters for the magnesium, carbon, silicon, and aluminum has been studied.

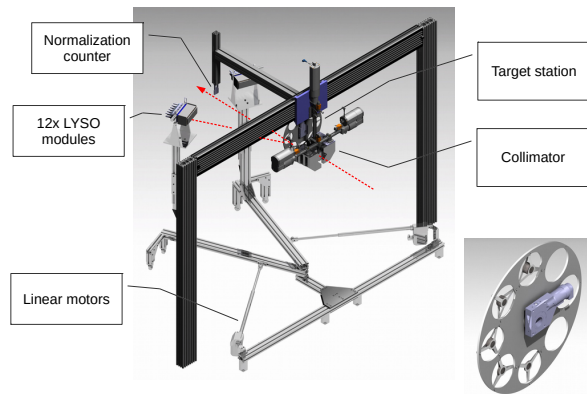


Fig. 3: Test setup at the BIG KARL experimental area.

On-line results

The preliminary (on-line) result of this measurements confirm the clear identification of elastic dC -scattering events as shown in Fig. 4. The detailed off-line analysis is in progress.

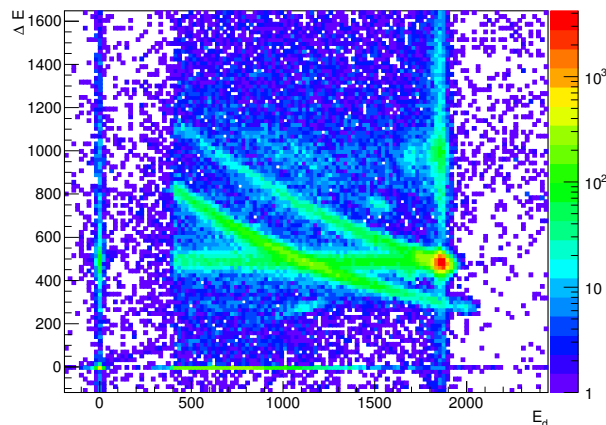


Fig. 4: A typical $\Delta E/E$ spectra for deuterons stopped in one of the LYSO modules for beam energy of $T_d=270$ MeV.

Outlook

The next step will be the production run in March 2017 with the already commissioned setup and preparation of the concept for an internal polarimeter at one of the COSY straight sections. A new idea for the target design is also under investigation, based on the use of small diamond pellets ($10 \div 100 \mu\text{m}$) to sample the beam and provide a 2-dimensional polarization profile of the beam's cross section. Laboratory tests of the target system elements will be the subject of the ongoing activities in 2017 as well. ^a IKP FZJ,

Jülich, Germany

^b RWTH Aachen University, Germany

^c HEPI TSU, Tbilisi, Georgia

* supported by SRNSF grant, Georgia

References:

- [1] http://pos.sissa.it/archive/conferences/243/026/PSTP2015_026.pdf
- [2] Hamamatsu R1548-07.
([http : //www.hamamatsu.com/us/en/R1548 - 07.html](http://www.hamamatsu.com/us/en/R1548-07.html))
- [3] SensL SiPM MicroFC-60035-SMT.
([http : //sensl.com/estore/microfc - 60035 - smt /](http://sensl.com/estore/microfc-60035-smt/))
- [4] Cerium doped Lutetium PreLude420 crystal.
([http : //www.crystals.saint - gobain.com/PreLude_420_Scintillator.aspx](http://www.crystals.saint-gobain.com/PreLude_420_Scintillator.aspx))
- [5] LYSO Ce scintillator.
([http : //www.epic - crystal.com/shop_reviews/lyso - scintillator/](http://www.epic-crystal.com/shop_reviews/lyso-scintillator/))
- [6] Phillips Scientific 16 Channel Charge ADC CAMAC Model 7166.
([http : //www.phillipsscientific.com/pdf/7166ds.pdf](http://www.phillipsscientific.com/pdf/7166ds.pdf))
- [7] SIS3316-250-14 16 channel 250 MSPS 14-bit.
([http : //www.struck.de/sis3316.html](http://www.struck.de/sis3316.html))

Automated Measurement of the COSY Injection Energy

B. Nauschütt

The beam energy at injection from the cyclotron into COSY is measured with the time of flight method. Two capacitive phase probes are used for this (labeled P2 and P3, with P2 closer to the cyclotron), which are located in the long straight section of the injection beam line. The signals from these probes are recorded by means of an oscilloscope with up to 20 GS/s. The data analysis is performed by a dedicated software, that was developed especially for this purpose and is running on the same device.

The software is written in Java and is capable of performing the processing and analysis needed to extract the energy and other beam parameters out of the measured data automatically.

The probes detect the bunches of the passing beam without affecting them. The marco pulse is used as trigger.

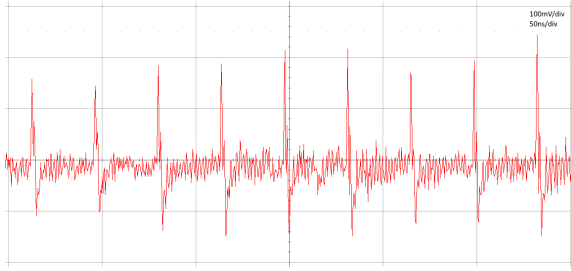


Fig. 1: A raw signal from phase probe P2 showing single bunches.

To improve the signal to noise ratio, several bunches are averaged with knowledge of the cyclotron frequency.

For the analysis, the signals are integrated. The resulting pulses can be described by

$$f(t) = A \cdot e^{-\frac{1}{2} \left(\frac{t-t_0}{m_\sigma \cdot (t-t_0) + \sigma_0} \right)^2} \quad (1)$$

with t_0 being the time, at which the pulse reaches its maximum A and m_σ and σ_0 being the pulse's asymmetry and width. The integral of a pulse is proportional to the beam current, however the proportionality factor has yet to be determined.

A and t_0 are determined by fitting a polynomial 2nd degree onto the points around the maximum of a pulse. m_σ and σ_0 result from a modified Gaussian fit:

$$m_\sigma \cdot (t - t_0) + \sigma_0 = \sqrt{\frac{(t - t_0)^2}{2 \cdot \ln\left(\frac{A}{f(t-t_0)}\right)}} \quad (2)$$

The software uses t_0 and the phase probes' distance of $L = 26.060\text{m} \pm 0.005\text{m}$ [1] to calculate the beam energy. The time of flight is corrected by the electrical delay, that the signals have due to different cable lengths. This time was measured as $t_{\text{delay}} = 0.36\text{ns}$.

Since the distance between the bunches themselves is smaller than the distance between the phase probes, it is necessary to know how many bunches fit in between. To determine this value, that is described by N , an estimate of the beam energy is used.

$$v_{\text{est}} = c \cdot \sqrt{\frac{b}{1+b}} \quad \text{with} \quad b = \frac{T_{\text{est}}}{E_0} \cdot \left(2 + \frac{T_{\text{est}}}{E_0} \right) \quad (3)$$

$$N = (\text{integer}) \left(\frac{L \cdot f}{v_{\text{est}}} \right) \quad \text{so} \quad v = \frac{L}{\frac{N}{f} + t_1} \quad (4)$$

With t_1 as the measured time difference. To transfer the velocity information into energy information:

$$T = E_0 \cdot \left(\frac{1}{\sqrt{1 - \left(\frac{v}{c}\right)^2}} - 1 \right) \quad (5)$$

T_{est} := estimated kinetic energy (by default: 45MeV for protons, 75MeV for deuterons)

T := particle's kinetic energy

$E_0 = m \cdot c^2$:= particle's rest energy

By comparison of the measured t_0 to its assumed value, the cyclotron frequency can be measured, too, if it is known roughly. The difference of the pulses' t_0 parameter and the assumed cyclotron period times the number of the pulse's averaging n has a linear relation. Fitting a linear function with slope m , the frequency is

$$f_{\text{cyclotron}} = \left(\frac{1}{f_{\text{cyclotron,estimated}}} - \frac{m}{n} \right)^{-1} \quad (6)$$

The software performs these calculations automatically and saves the results in a text file. It also shows a history of earlier measurements (fig. 2).

Using simulated signals, it can be confirmed, that the software can measure the beam energy, as well as the other parameters. The accuracies for specific settings can be determined this way, too.

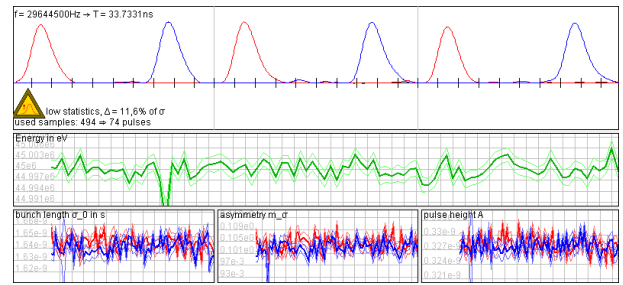


Fig. 2: Series of simulated signals for P2(red) and P3(blue).

In the lower windows, the thick lines indicate the mean, while the brighter, thin lines indicate the precision (in this case 11.6% of the standard deviation). Used parameters: $\sigma_0 = 1.5\text{ns}$, $m_\sigma = 0.13$, $A = 3.5 \cdot 10^{-10}$, $T = 45\text{MeV}$, $S/N = 1$, $S = 10 \frac{\text{GS}}{\text{s}}$, 8bit vertical resolution, pulses are 20-fold averaged. The resulting peaks are smaller, broader and more symmetric than the original, which is mainly due to a smoothing function, that is applied during the processing.

References:

- [1] H. Labus, N.Dolfus J. Dietrich, R. Maier, Measurement of the COSY Injection Energy, Annual Report 1992
- [2] R. Cee, Longitudinale Strahldiagnose mit Phasensonden am Heidelberger Hochstrominjektor (1997)

Overview

The High-Energy Storage Ring (HESR) will be part of the future accelerator facility FAIR at GSI in Darmstadt.

In the HESR, as in many accelerators, residual gas molecules in the beam pipe become ionised by the anti-proton beam. These positive ions are trapped in the potential well of the beam, causing neutralisation effects and reducing beam quality significantly [3]. To reduce these effects, Ion Clearing techniques have been developed, such as clearing electrodes.

The present report gives an overview of simulations on two designs that were proposed for the HESR. Using COMSOL Multiphysics®, their electric fields were studied as well as the behaviour of ions in the beam pipe.

The two designs proposed are:

- (1) The *Stripe-Design*, that consists of two 90°-arc-shaped stripes of 290mm length. Their diameter is equal to the diameter of the vacuum pipe.
- (2) The *Button-Design*, that features two button shaped electrodes with a diameter of 25mm on each side of the beam.

E-Field Comparison

The electrodes were modelled in COMSOL Multiphysics® and their electric field was calculated for several voltages. The Results are shown in figure 1 and 2. As can be seen from the charts, the magnitude along the beam axis is about five times higher for the stripe-design at equal voltage levels. In general, the stripe electrodes field is much stronger and therefore to be preferred.

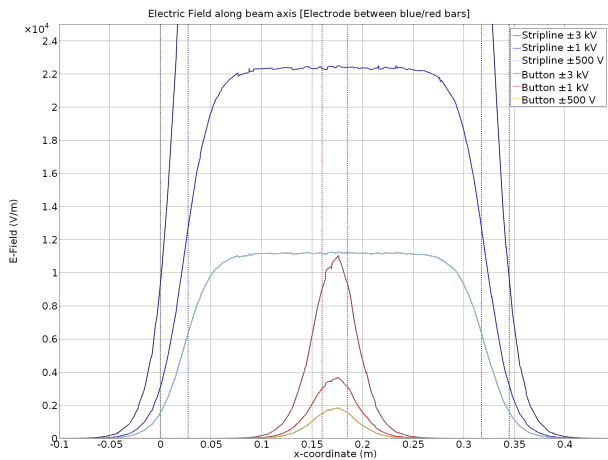


Figure 1: Electric field of clearing electrodes along the beam axis. The vertical lines indicate the electrodes geometry.

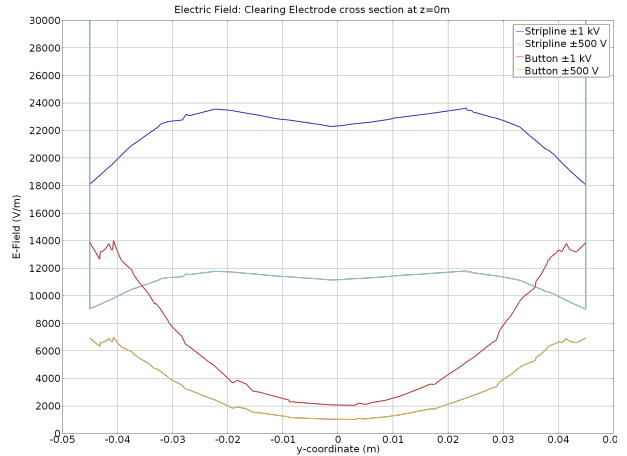


Figure 2: Electric field of clearing electrodes in cross section.

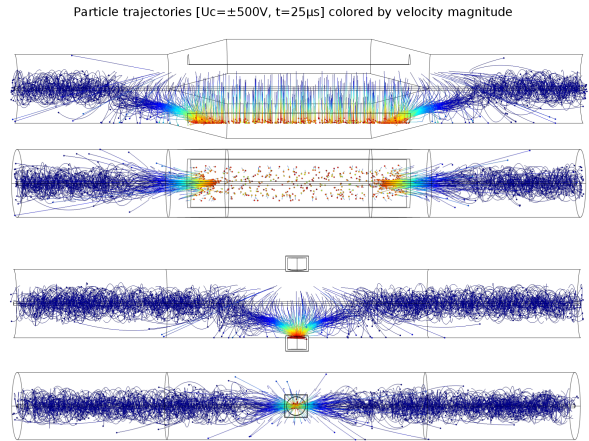


Figure 3: Trajectories of ions coloured by velocity magnitude for $U = \pm 500V$: top and side view for strip- and button-design.

Ion Particle Tracing

Clearing Electrode

In a second step, the fields were used to simulate the trajectories of charged ions using the particle tracing module of COMSOL Multiphysics®. As the residual gas consists mainly of H_2 molecules, H_2^+ ions were chosen. During the ionization process, most of the energy is taken by the electron, so that an average thermal energy can be assumed for the ions. For H_2^+ ions this equals $0.039eV$ [2, sec. 6].

The trajectories were simulated for 1000 ions over a period of $25\mu s$ using different voltage levels. An example is given in figure 3. One can see that the ions are trapped in the potential well of the beam until they eventually get attracted and cleared by the electrode.

Using the accumulator feature of COMSOL Multiphysics®, the particles were counted so that an esti-

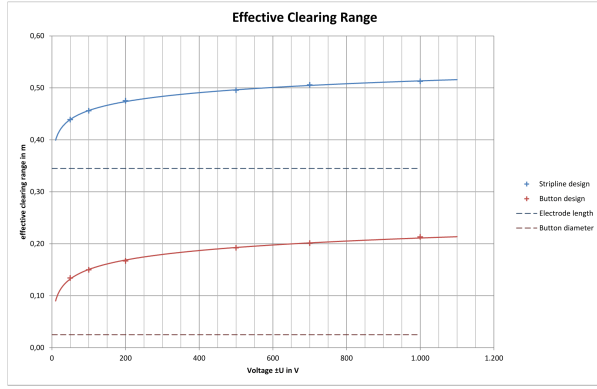


Figure 4: Effective clearing range for the button- (red) and stripe-design (blue). The dotted lines indicate the electrodes geometry.

mation for the effective clearing range could be given. This is the range along the beam axis where the electric field is strong enough to trap and clear the ions. For $U = \pm 500V$ the range equals $0.495m$ for the stripe- and $0.192m$ for the button-design. It is in general 2 to 2.5 times larger as can be seen in figure 4.

The accumulator feature also allowed it to investigate the distribution of impacts on the electrodes. While this is rather radial with the hotspot centred for the button-design, there are two hotspots on either side of the stripe electrode. This can also be seen on figure 3. The peak is, however, in the nano-watt-range (considering the ions energy and mean production rate) and thus negligible.

Arc Section

In the HESR there are multiple types of magnets that also affect the behaviour of ions. To consider for these effects, a section of an arc consisting of a sextupol, a quadrupol, the clearing electrode and a dipol was modelled. Again $2000 H_2^+$ ions were traced in the magnetic and electric fields.

It turns out, that there is an accumulation of ions on either end of the dipole magnets. This is due to the drift velocity that results from the superposition of the dipoles magnetic and the beams electric field and was among others already described in [1]. This drift velocity is slow compared to the ions velocity in other sections, and directed alongside the beam to the outside of the ring and in opposite direction to the inside of the ring, respectively. This ion motion is shown in figure 5. When choosing the polarity of the clearing electrode, this specific behaviour should be kept in mind.

The magnetic fields of the quadrupole and sextupole magnets have only minor influence on the positive ions, so that their trajectories are dominated by the beams electric field and their thermal motion. The simulations yielded no noticeable effects from these magnets.

Conclusion

The simulations clearly showed, that the stripe-design requires less than a fifth of the voltage that is necessary to reach an equal clearing rate when using the button-design. Also, its clearing range is more than two times

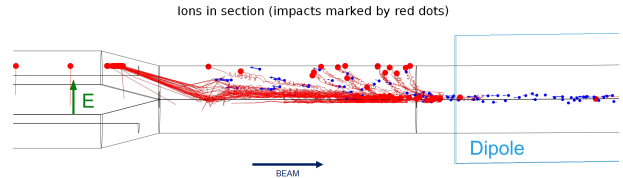


Figure 5: Ions motion at one end of a dipole with a strip clearing electrode. The traces of cleared ions are marked red, other ions in blue.

larger. Therefore the stripe-design should be preferred over the button-design.

Considering the location of clearing electrodes in the ring, it is best to place them close to the dipoles, to absorb the local accumulation of ions. The polarity should then be chosen accordingly, which is placing the cathode to the left side in front of a dipole or to the right side after a dipole (referring to the beam direction).

References

- [1] **Frank Hinterberger**, “Ion Trapping in the High-Energy Storage Ring HESR”, Berichte des Forschungszentrums Jülich 4343, 2011
- [2] **Frank Hinterberger**, “Counteracting Trapped Ion Effects in the HESR”, Berichte des Forschungszentrums Jülich 4357, 2012
- [3] **Y. Baconnier, A. Poncet and P. Tavares**, “Neutralization of accelerator beams by ionization of the residual gas”, In *Jyvaeskylae 1992, Proceedings, General accelerator physics, vol. 2* 525-564. CERN Geneva - CERN-94-01 (94/01,rec.Mar.) 525-564

Reconstruction efficiency for Forward-Central coincidences.

W. Parol¹, I. Ciepał¹ and B. Kłos²

1 Introduction

In 2013 an experiment dedicated to the study of the few-nucleon system dynamics via the $^1H(d, pp)n$ breakup reaction was performed at FZ-Jülich. In the experiment a deuteron beam impinged on a pellet target of hydrogen and proton-proton or deuteron-proton coincidences were registered with the WASA setup. The deuteron beam was produced by Cooler Synchrotron COSY working in the super-cycle mode at three energies of 340 MeV, 380 MeV and 400 MeV. The aim of the data analysis presented here is to obtain the differential cross-section for the proton registered in Forward-Central angular configurations of the breakup reaction. The cross-section distributions will be compared with the exact Faddeev calculations which include different components of the few-nucleon system dynamics like the so-called three-nucleon force, Coulomb force and relativistic effects. In this report we focus on PSB ADC analysis and obtaining a reconstruction efficiency for the deuteron-proton elastic scattering at 340 MeV.

2 Analysis

The Forward-Central coincidences were first preselected. The deuterons registered in the Forward part of the detector (stopped in FRH4) were identified and the coincident protons in the Central part were found based on the planarity condition ($\Delta\varphi \sim 180^\circ$). The selected protons were used to perform PSB ADC gain matching. Due to better angular resolution (0.2°) of the Forward detector, the scattering angles were selected via the deuteron polar angles θ_d . The limit was set in a range of $\theta_d \in (13^\circ, 14^\circ)$ (the range was set at the border of the punch-through in PSB) and the ADC distributions were prepared for each PSB element. Then, the positions of gauss-like distributions for each PSB element were taken and gain factors were obtained. The result of the applied ADC matching is shown in the Fig. 1.

Another important step of the analysis was to calculate the efficiency for the registration of the deuteron-proton elastic coincidences. The WASA Monte-Carlo simulations for the deuteron-proton elastic scattering at 340 MeV were performed and the efficiency was calculated at each deuteron scattering angle according to the formula:

$$\varepsilon_{rec}(\theta_d) = \frac{N^{rec}(\theta_d)}{N^{vert}(\theta_d)} \Big|_{|\Delta\phi-180^\circ|<5^\circ \wedge dist(\theta_p, \theta_d) < 3^\circ} \quad (1)$$

where: $N^{vert}(\theta_d)$ is the number of the simulated coincidences, whereas $N^{rec}(\theta_d)$ is the number of the reconstructed events. Besides the planarity condition, the cut a distance to the elastic scattering kinematics ($dist(\theta_p, \theta_d) < 3^\circ$) was applied. The distribution of the efficiency is presented in Fig. 2.

In the next step of the data analysis, the time integrated luminosity for the experiment will be calculated.

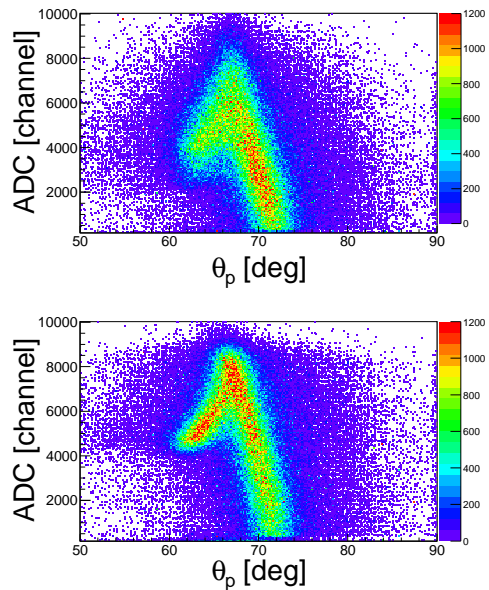


Fig. 1: Distribution of protons energy deposition in PSB as a function of angle reconstructed in MDC before (*upper panel*) and after (*lower panel*) applying gain matching.

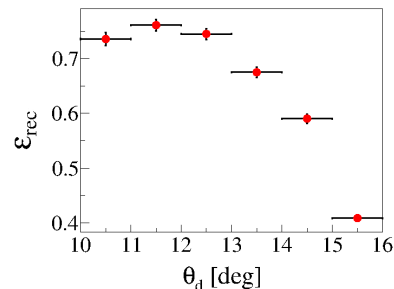


Fig. 2: Efficiency for registration of the proton-deuteron pair, as defined in Eq. 1.

-
1. Institute of Nuclear Physics Polish Academy of Sciences, PL-31342 Krakow, Poland
 2. Institute of Physics, University of Silesia, PL-40007 Katowice, Poland

Amplitude estimation of a sine function based on confidence intervals and Bayes' theorem

D. Eversmann^a, Marcel Rosenthal^{a,b}, Joerg Pretz^{a,b}

^a RWTH Aachen University, Germany, ^b Forschungszentrum Juelich, Germany

During the analysis of the data for the spin coherence time measurement, it was realized that one gets a bias fitting the amplitude P of a sine-wave, especially at small amplitudes. For small amplitudes the estimated value \hat{P} is on average larger than the true P . This is evident, because for $P = 0$ the least squares fit using the functional form

$$y(x) = N_0 (1 + A \sin(x) + B \cos(x)), \quad P = \sqrt{A^2 + B^2}$$

in general results in a estimator $\hat{P} > 0$. In the example of figure 1 (a) the fit yields $\hat{P} = 0.20 \pm 0.14$ for $P = 0.1$. Figure 1 (b) shows the result of \hat{P} for 10000 fits to distributions generated with $P = 0.1$. The average \hat{P} amounts to 0.2 which corresponds to a bias of 0.1. Interpreting the fit result $\pm 1\sigma$ as a 68% confidence interval for P may even lead to coverage in the unphysical region below zero.

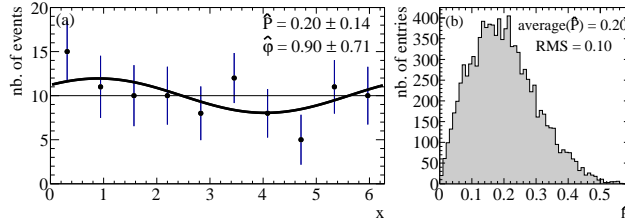


Fig. 1: (a): Data points simulated according to eq. (??) with $N = 100$ events with $A = 0.1$ and $B = 0$. The black line shows the result of a least squares fit with $\hat{P} = \sqrt{\hat{A}^2 + \hat{B}^2} = 0.20 \pm 0.14$ and $\hat{\phi} = 0.90 \pm 0.71$. (b): Distribution of \hat{P} for 10000 simulations.

A new algorithm based on the Feldman-Cousins algorithm of likelihood ratios is developed to construct improved confidence intervals having only coverage in the allowed region $P > 0$. Moreover using Bayes' theorem, a probability density function for P is derived which leads to better estimates compared to a simple least squares fit.

The main result is displayed in Fig. 2. We study the case where the amplitude of a sine-wave decays exponentially with time. The situation is very similar to the case of a decreasing horizontal polarization due to decoherence. In figure 2 the dotted line shows an exponential function $Ce^{-t/\tau}$ with a decay constant $\tau = 1$ and amplitude $C = 0.3$. Data were generated at ten different times t following the proper probability function for P which is in this case a Rice distribution. These values are displayed as data points with their statistical errors for the case that $N = 1000$ events are detected at each time bin. The blue curve shows the result of a least squares fit to these data points. It clearly overestimates the true curve (dotted line).

The vertical bands at each t -bin show the probability density function $\tilde{f}(P|\hat{P})$ as a function of P , where \hat{P} is the generated

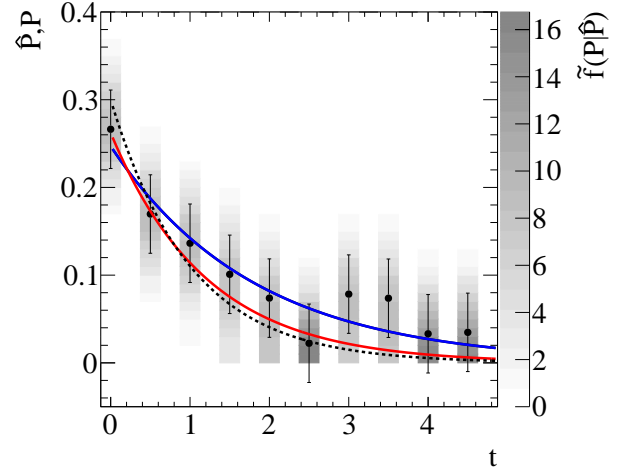


Fig. 2: Dotted line: $P(t) = Ce^{-t/\tau}$ with $\tau = 1$ and $C = 0.3$. Data points: random values according to to probability distribution for \hat{P} assuming 1000 events at each time bin. Blue line: result of a least squares fit to the data points. Vertical bands: probability distribution $\tilde{f}(P|\hat{P})$ for true P for the given generated \hat{P} . Red line: Result of a likelihood fit to these probability distributions.

value (i.e. the data point) derived using the Feldman-Cousins algorithm and Bayes' theorem. The red curve shows the result of a likelihood fit with the likelihood function

$$\mathcal{L} = \prod_{i=1}^{N_{bin}} \tilde{f}(Ce^{-t_i/\tau}|P_i)$$

varying τ and C to maximize \mathcal{L} . In this example the likelihood fit yields 1.20 ± 0.37 (red line) for $\hat{\tau}$ compared to 1.81 ± 0.51 (blue line) for the least squares fit to the black points. For 10000 simulations one finds $\langle \hat{\tau} \rangle = 1.04$ for the likelihood and 1.63 for the least squares fit. On average the likelihood result has a bias of $0.04/0.35=0.11$ of its statistical error, whereas the bias for the least square fit is $0.63/0.48=1.3$. This proves that the likelihood fit using a proper probability distribution function gives a result closer to the true value $\tau = 1$, as compared to the simple least squares fit.

This work has been published in JINST **11** (2016) no.05, P05003 (doi:10.1088/1748-0221/11/05/P05003, arXiv:1512.08715 [physics.data-an])

Study of Excited Ξ Baryons in $\bar{p}p$ -Collisions with the PANDA Detector

Jennifer Pütz

Introduction

Understanding the excitation pattern of baryons is indispensable for a deep insight into the mechanism of non-perturbative QCD. Systematic experimental studies have so far been focused on the nucleon excitation spectrum, while very little is known on excited states of double and triple strange baryons. In $\bar{p}p$ collisions a large fraction of the cross section is associated to final states with a baryon-antibaryon pair together with additional mesons, giving access to excited baryon and antibaryon states. With its large acceptance, the PANDA detector is well-suited for a comprehensive baryon spectroscopy program in the multi-strange sector.

Event generation

For the study of excited Ξ^- baryons 1.5 million signal events for the reaction $\bar{p}p \rightarrow \Xi(1820)^- \bar{\Xi}^+$; $\Xi(1820)^- \rightarrow \Lambda K^-$; $\bar{\Xi}^+ \rightarrow \bar{\Lambda} \pi^+$; $\Lambda \rightarrow p \pi^-$ were generated with the event generator EvtGen at $p_{\bar{p}} = 4.6 \text{ GeV}/c$ and another 1.5 million for its charge conjugate channel $\bar{p}p \rightarrow \bar{\Xi}(1820)^+ \Xi^-$. If not otherwise specified, the charge conjugate process is implicitly included in the following.

The simulation was done by using the PandaRoot framework at trunk revision 29165. The properties of the $\Xi(1820)^-$ resonance used in EvtGen are taken from [1]. The production cross section is expected to be of the same order ($\sim \mu\text{b}$) as for the ground state Ξ^- production in $\bar{p}p \rightarrow \Xi^- \bar{\Xi}^+$ [2].

Reconstruction

To reconstruct all particles involved in the reaction one starts with the final state particles and proceeds backwards through the reaction chain. The selected final state particles are proton, anti-protons, π^- , π^+ and K^- mesons. Due to the use of an ideal track reconstruction, only particles with at least 3 hits in any inner tracking detector of PANDA are selected. The particle identification is also ideal. A study of realistic particle identification is in preparation.

The reconstruction efficiency for the final state particles is shown in table 1.

Table 1: Reconstruction efficiency ϵ for final state particles for $\bar{p}p \rightarrow \Xi(1820)^- \bar{\Xi}^+$ (left) and $\bar{p}p \rightarrow \bar{\Xi}(1820)^+ \Xi^-$ (right). The statistical error on the reconstruction efficiency is $\sigma_\epsilon = 0.1\%$ for all particles.

final state	$\epsilon/\%$	final state	$\epsilon/\%$
π^-	85.5	π^+	84.7
π^+ ($\bar{\Xi}^+$)	83.3	π^- (Ξ^-)	82.9
π^+ ($\bar{\Lambda}$)	86.5	π^- (Λ)	86.1
K^-	78.2	K^+	82.9
p	82.7	p	78.7
\bar{p}	76.3	\bar{p}	79.6

For the reconstruction of a Λ hyperon a proton and a π^- meson are combined. The reconstruction of $\bar{\Lambda}$ is done by combining a \bar{p} and a π^+ . After combining the daughter particles, a mass cut within the mass window $0.3 \text{ GeV}/c^2$ symmetric to

the nominal Λ mass is performed on the Λ candidate. Then a vertex fit is performed on the selected candidate. On the fitted candidate a mass constraint fit is performed using a kinematic fitter. Only those candidates which have a probability of more than 1% in both fits are selected. If more than one candidate is found, the candidate with the smallest χ^2 is chosen.

In case of a correct selection of π^+ as daughter particle of $\bar{\Lambda}$, only one π^+ meson is left as daughter of the $\bar{\Xi}^+$ baryon.

The reconstruction scheme of the $\bar{\Xi}^+$ is similar to the reconstruction of Λ and $\bar{\Lambda}$. After combining the $\bar{\Lambda}$ hyperon and the π^+ meson a mass cut within a window of $0.3 \text{ GeV}/c^2$ symmetric to the nominal $\bar{\Xi}^+$ mass is performed. On the selected candidate a vertex fit and a mass constraint fit is performed. The candidate which has a probability of more than 1% in both fits and the smallest χ^2 value is selected. The same is done for the Ξ^- in the charge conjugate channel.

For the reconstruction of $\Xi(1820)^-$ baryons a Λ hyperon and a K^- meson are combined. Only candidates with a mass within a mass window of $0.3 \text{ GeV}/c^2$ symmetric to the nominal $\Xi(1820)^-$ mass are selected and a vertex fit is performed. Fitted candidates with a probability of more than 1% and the smallest χ^2 value are selected for further studies. The reconstruction of $\bar{\Xi}(1820)^+$ is done by combining a $\bar{\Lambda}$ hyperon and a K^+ meson from the charge conjugate channel and using the same cuts.

The vertex resolution for $\Xi(1820)^-$ and $\bar{\Xi}(1820)^+$ is shown in table 2.

Table 2: Vertex resolution for $\Xi(1820)^-$ and $\bar{\Xi}(1820)^+$

Position	$\bar{p}p \rightarrow \Xi(1820)^- \bar{\Xi}^+$	$\bar{p}p \rightarrow \bar{\Xi}(1820)^+ \Xi^-$
x/mm	0.31	0.30
y/mm	0.30	0.29
z/mm	0.86	0.88

The mass distribution of $\Xi(1820)^-$ after all cuts is shown in figure 1. The reconstructed mass of the $\Xi(1820)^-$ resonance obtained from a Voigt fit is about $1.822 \text{ GeV}/c^2$. The fitted width of the distribution is $\Gamma = (25.28 \pm 0.02) \text{ MeV}$, to be compared to the input value $\Gamma = 24 \text{ MeV}$

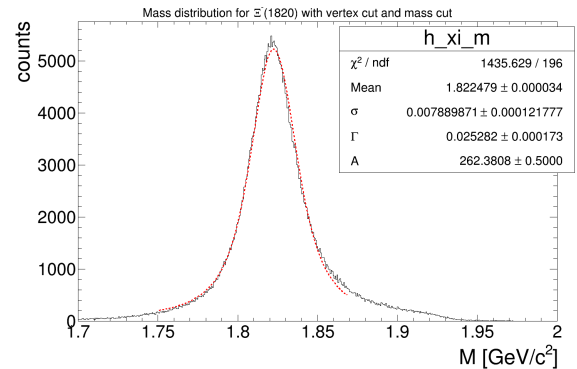


Fig. 1: Mass distribution of $\Xi(1820)^-$ (blue histogram). The Voigt Fit is shown as red dashed line.

To reconstruct the full reaction chain, $\Xi(1820)^-$ and $\bar{\Xi}^+$

are combined. This is also done for $\bar{\Xi}(1820)^+$ and Ξ^- in the charge conjugate channel. The resulting four-momentum vector of both daughter particles are fitted to the initial four-momentum vector $(p_x, p_y, p_z, E) = (0, 0, 4.6, 5.63)$ GeV of the $\bar{p}p$ entrance channel. Only those candidates are selected which have a probability of more than 1%. Table 3 shows the reconstruction efficiency of the intermediate state particles.

Table 3: Reconstruction efficiency ε for intermediate state particles for $\bar{p}p \rightarrow \Xi(1820)^- \bar{\Xi}^+$ (left) and $\bar{p}p \rightarrow \bar{\Xi}(1820)^+ \Xi^-$ (right).

particle	$\varepsilon/\%$	particle	$\varepsilon/\%$
Λ	32.9	Λ	26.8
$\bar{\Lambda}$	25.2	$\bar{\Lambda}$	31.2
$\bar{\Xi}^+$	13.0	Ξ^-	13.7
$\Xi(1820)^-$	27.6	$\bar{\Xi}(1820)^+$	27.8
$\Xi(1820)^- \bar{\Xi}^+$	2.1	$\bar{\Xi}(1820)^+ \Xi^-$	2.2

As a next step background simulation will be done and a partial wave analysis of $\Lambda K^- \bar{\Xi}^+$ final state and its charge conjugate final state will be explored.

Partial Wave Analysis with PAWIAN

The **Partial Wave Interactive Analysis** Software is a software package for partial wave analysis dedicated to all physics cases at PANDA [3]. The user has the possibility to define complicated decay trees and to choose different spin formalisms and dynamics. The software has been developed for mesons and was extended to baryons recently. Detailed test for baryons are still missing.

The aim of a first study of PAWIAN is to reproduce the input values of given quantum numbers. For this first study, we focused on one single initial state with the quantum numbers $J^{PC} = 1^{--}$. This is realized by choosing the production channel $\bar{p}p \rightarrow J/\Psi \rightarrow \Xi(1690)^- \bar{\Xi}^+$ at beam momentum $p_{\bar{p}} = 4.065$ GeV/c.

First checks of the software were done by testing the stability of the maximum likelihood fit. For this check, 30000 toy data events were generated with Blatt-Weisskopf barrier factors and additional 100000 events with a uniform phase space distribution were generated. The toy data production requires a set of start parameters. After generation of the toy data the start parameters were changed to test the stability of the maximum likelihood fit. The maximum likelihood fit was performed with different sets of start parameters when using the same set of toy data. The test results show that the maximum likelihood fit procedure converges to the same result, independent of the start parameter set. The next step is to check if the input values corresponding to different sets of quantum numbers for the initial state are reproduced by the fit.

References:

- [1] K. A. Olive *et al.* [Particle Data Group Collaboration], *Chin. Phys. C* **38**, 090001 (2014). doi:10.1088/1674-1137/38/9/090001
- [2] W. Erni, I. Keshelashvili, *et al.*, "Physics performance report for PANDA: Strong interaction studies with antiprotons.", arXiv preprint arXiv:0903.3905 (2009)

- [3] Bertram Kopf, *et al.* "PAWIAN PWA Software", <https://panda-wiki.gsi.de/foswiki/bin/view/PWA/PawianPwaSoftware>

Search for η -mesic ${}^3\text{He}$ with the WASA-at-COSY facility

O. Rundel^a, O. Khreptak^a, M. Skurzok^a, W. Krzemien^b, P. Moskal^a

In May 2014 the experiment on searching η -mesic ${}^3\text{He}$ has been provided by WASA-at-COSY collaboration. Proton beam and deuterium pellet target were used. The beam momentum of the ramped beam was changing in the range corresponding to the range of Q for creating ${}^3\text{He}$ and η from -70 MeV to $+30\text{ MeV}$. The data obtained from experiment are currently analysed.

For performing of one of the ways of luminosity estimation channel $pd \rightarrow {}^3\text{He}\eta$ was analysed. It's one of the processes that can be used for this purpose. We also plan to analyse the channel of quasi free proton-proton scattering $pd \rightarrow ppn_{spectator}$.

The analysed during last year channel $pd \rightarrow {}^3\text{He}\eta$ has essential background among forward ${}^3\text{He}$ tracks. Nevertheless, the algorithm used in current analysis allowed to reduce it. It was shown that only two background reaction persist (Fig.1).

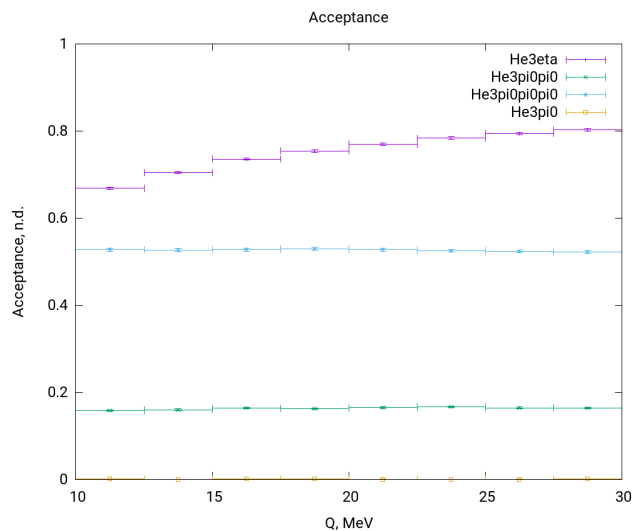


Fig. 1: Acceptance for reactions $pd \rightarrow {}^3\text{He}\eta$, $pd \rightarrow {}^3\text{He}2\pi^0$, $pd \rightarrow {}^3\text{He}3\pi^0$ and $pd \rightarrow {}^3\text{He}\pi^0$ estimated for analysis algorithm used for luminosity estimation. It's shown that the influence of reaction $pd \rightarrow {}^3\text{He}\pi^0$ is neglectable.

For performing the analysis ${}^3\text{He}$ missing mass spectra were built. The whole range of beam momentum that corresponded to the range of $Q(pd \rightarrow {}^3\text{He}\eta)$ from -70 MeV to $+30\text{ MeV}$ was split into 40 bins. ${}^3\text{He}\eta$ can be visible only when $Q > 0$. The accuracy of analysis was satisfactory only for $Q > 10\text{ MeV}$.

The distributions of ${}^3\text{He}$ missing mass for each Q -bin were fitted by the sum simulated ones obtained for all observed reactions (Fig.2). For each Q -bin, the fit was performed independently and had three parameters corresponding to the amounts of events from all observed processes.

From the fit, the number of events corresponding to ${}^3\text{He}\eta$ was obtained. The amount of data that has been analysed with this algorithm is 399 runs of total amount of 1012. This is almost 40% of the whole data collected in

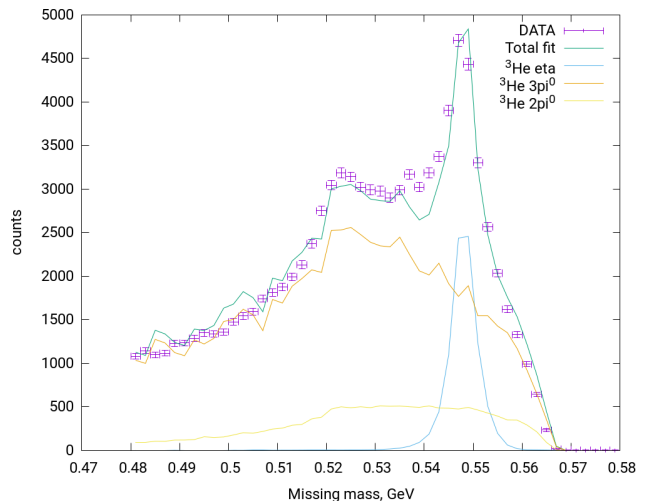


Fig. 2: Fit of missing mass spectrum obtained from the experiment with sum of Monte Carlo simulations of $pd \rightarrow {}^3\text{He}\eta$, $pd \rightarrow {}^3\text{He}2\pi^0$ and $pd \rightarrow {}^3\text{He}3\pi^0$. The example spectrum corresponds for one Q -bin ($[20; 22.5]\text{ MeV}$).

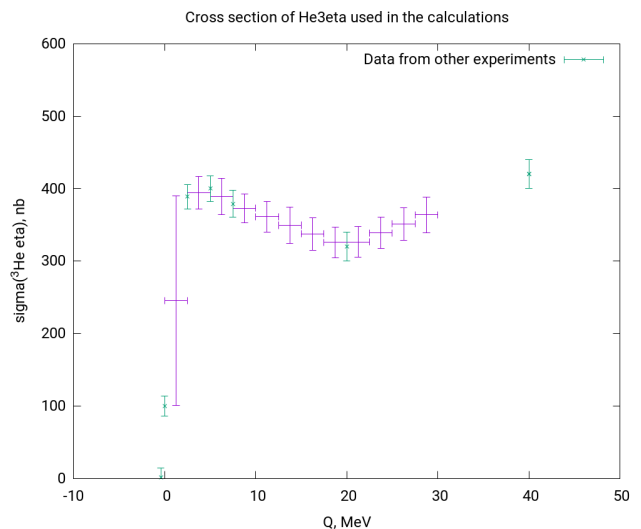


Fig. 3: $pd \rightarrow {}^3\text{He}\eta$ cross section values estimated for all Q -bins present in the analysis. Experimental data taken for interpolation are described in the papers [1, 2]

the experiment.

In order to calculate the integral luminosity the amount of events was divided by the acceptance for ${}^3\text{He}\eta$ (Fig.1) and by the cross section. The cross section values for each Q -bin were obtained via interpolation (Fig.3). Experimental values used for interpolation have been taken from [1, 2].

For the part of data that have been processed by the algorithm the estimation of integral luminosity has been performed (Fig.4). By the order of magnitude these val-

ues are in agreement with proposal [3] and alternative estimations. Nevertheless the exact estimation would be provided by analysing the channel of quasi free proton-proton scattering $pd \rightarrow ppn_{spectator}$.

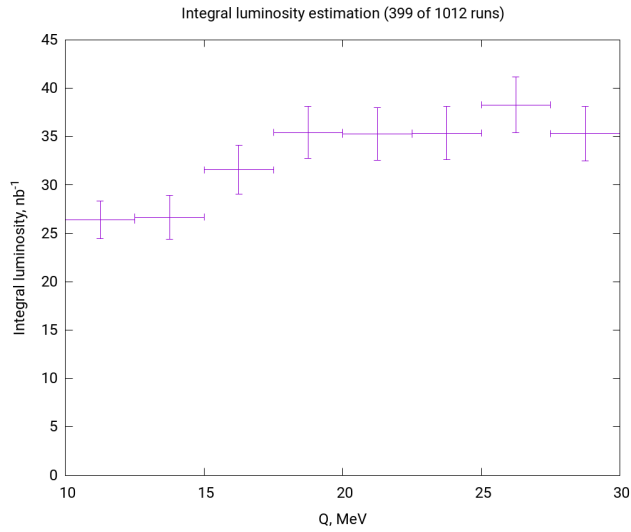


Fig. 4: Integral luminosity obtained from $pd \rightarrow {}^3\text{He}\eta$ reaction. The amount of data processed by the analysis is about 40%.

We acknowledge support by the Foundation for Polish Science - MPD program, by the Polish National Science Center through grants No. 2011/01/B/ST2/00431, DEC-2013/11/N/ST2/04152 and by the FFE grants of the Forschungszentrum Jülich.

References:

- [1] T. Mersmann *et al.*, *Phys. Rev. Lett.* *98*, 242301, January 2007
- [2] R. Bilger *et al.*, *Phys. Rev. C* *65*, 044608, 2002
- [3] P. Moskal, W. Krzemień, M. Skurzok, 2014, *COSY Proposal/Beam Request: Search for the η -mesic ${}^3\text{He}$ with WASA at COSY*, PAC Session No. 42 2013, Exp. No. 186.3, http://donald.cc.kfa-juelich.de/wochenplan/List_of_all_COSY_Proposals.shtml.

^a M. Smoluchowski Institute of Physics, Jagiellonian University, 30-059 Cracow, Poland

^b National Centre for Nuclear Research, 05-400 Otwock-Świerk, Poland

Systematic effects of orbit excursions in the spin tune mapping with solenoids*

A. Saleev^a for the JEDI collaboration

The method of spin tune mapping with static solenoids was tested by the JEDI Collaboration in September 2014 at COSY. Motivation of the study was to develop a method for compensation of unwanted background MDM spin rotation in the precursor EDM experiment. In the precursor experiment, the RF Wien filter is running on the spin tune frequency which leads to the resonant build-up of vertical polarization [1]. Build-up rate is proportional to the angle ζ between the stable spin axis at the location of RF Wien filter \vec{c} (this axis is defined at idle spin precession when RF Wien filter is not running) and the axis \vec{w} of magnetic RF field of the Wien filter. In the ideal case of strictly parallel axes of RF WF magnetic field and vertical guiding fields of main dipoles, and also in the absence of horizontal magnetic fields, the resonance strength ε which defines build-up rate will be proportional to the EDM signal ζ_{EDM} and the amplitude of the spin kicks χ_{WF} in the RF Wien filter:

$$\varepsilon = \frac{1}{2} \chi_{\text{WF}} |\vec{c} \times \vec{w}| = \frac{1}{2} \chi_{\text{WF}} \sin \zeta_{\text{EDM}}. \quad (1)$$

In the real magnetic ring, horizontal fields produced by magnet misalignments create background MDM spin rotation, which leads to the inclination of stable spin axis. This, in turn, spoils the resonant EDM build-up of polarisation with RF Wien filter, as the build-up rate will be significantly increased by strong MDM background. Magnet positions and corresponding field misalignments at the moment can be determined with the precision up to 10^{-4} rad. Such precision is missing 6 orders of magnitude in order to be sufficient to set EDM limit of 10^{-24} e-cm in the precursor experiment. In order to overcome the trouble of precise mechanical alignment of magnets, we proposed to compensate horizontal fields with additional horizontal (artificial imperfection-AI) field, and control the process with the spin tune measurement. When AI field is applied, spin tune changes according to the formula

$$\begin{aligned} \cos(\pi v_s(\chi_{\text{AI}})) &= \cos(\pi [v_s^0 + \Delta v_s(\chi_{\text{AI}})]) \\ &= \cos(\pi v_s^0) \cos\left(\frac{1}{2} \chi_{\text{AI}}\right) \\ &\quad - \sin(\pi v_s^0) \sin\left(\frac{1}{2} \chi_{\text{AI}}\right) (\vec{c} \cdot \vec{k}). \end{aligned} \quad (2)$$

Here, $\Delta v_s(\chi_{\text{AI}})$ denotes the change in spin tune from the unperturbed value v_s^0 which is observed when the artificial imperfection is not activated. χ_{AI} is an amount of spin rotation around \vec{k} - a spin rotation axis of the AI device.

The measurements of Δv_s for a given χ_{AI} and \vec{k} produce a spin tune map. In our study, we used static solenoids with longitudinal magnetic fields as AIs. In this case, the product $(\vec{c} \cdot \vec{k}) = c_z$ defines longitudinal direction of stable spin axis at location of solenoid. Parabolic dependence $\Delta v_s(\chi_{\text{AI}}) \approx \chi_{\text{AI}}^2$ will have a minima at $\chi_{\text{AI}}^{\text{min}} = 2c_z \tan(\pi v_s^0)$. Effectively, at $\chi_{\text{AI}}^{\text{min}}$ static solenoid compensate longitudinal field integral of the ring (up to first order). To compensate radial field integral (up to first order) using the same approach, static Wien filter

with radial B-field can be used, such that $(\vec{c} \cdot \vec{k}) = c_x$. During its operation, Wien filter should be transparent for the beam momentum, only rotating spin. Transparency of the AI device to the beam momentum means that it does not steer the beam, and there is no closed orbit excursions all over the ring during the spin tune mapping.

Continuous variation of \vec{k} that keeps condition of beam momentum transparency at different operation modes of AI can be realized with two configurations: 1) double helical snakes at 45 degree w.r.t. each other, superimposed with horizontal electric field plates to provide Wien filter condition, or 2) a snake produced by combination of 3 or 4 horizontal and vertical steerers, where the ratio of H and V fields defines spin axis (\vec{k}) and strength (χ_{AI}) of the snake. Such configuration allows for exact compensation of spin rotation in all horizontal fields of the ring.

Subsequent theoretical analysis revealed that compensation of horizontal imperfection fields would amount to compensation of EDM signal as well. In this regard, the method can be used exclusively for the determination of EDM signal with spin tune measurement. The greatest obstacle in both approaches- the spin tune mapping or RF Wien filter method- is how to separate the effect of spin rotation due to EDM in the integral motional E-field from the spin rotation due to MDM in the integral transverse magnetic fields (imperfection background). EDM spin rotation is intrinsic in main dipoles and proportional to the Lorentz force. Therefore, we should develop a method to control all horizontal magnetic fields which contribute to the magnetic field integral, as well as a means to set every dipole field parallel to each other. If the field integral can be controlled with the precision of up to $\approx 10^{-10}$ Tm, then the effect of spin rotation in the integral motional electric field due to EDM 10^{-24} e-cm, can be compensated. Using the description in the terms defined earlier, it should be possible to determine ζ_{EDM} in (up to first order approximation):

$$\zeta = \zeta_{\text{EDM}} + \zeta_{\text{MDM}} \quad (3)$$

by the variation of ζ_{MDM} which depends on configuration of horizontal fields (for example, by changing vertical steerer settings). Determination of ζ can be performed either by spin tune mapping (AI device should have variable \vec{k} , such that $\vec{c} \cdot \vec{k} = \sin \zeta$) or by using RF Wien filter method.

According to 2014 JEDI spin tune mapping study, relative precision of spin tune measurement 10^{-10} (see [2]) allows for determination of angular direction of stable spin axis \vec{c} at the level of $\sim 10^{-6}$ rad (preliminary results are given in [3]). However, this accuracy still needs further refinement, as the e-cooler solenoids, which were used as AI devices, produced closed orbit excursions at the level of 0.2-0.5 mm. Systematic effects of beam excursions during the spin tune mapping are the most important constraints of the method. We investigated the steering effect of misaligned solenoid on the spin motion in COSY ring using beam tracker COSY-Infinity. The solenoid was located at the place of 100 KeV e-cooler (in the middle of second straight section) and was set at specific misalignment angles ξ_x or ξ_y . Solenoid field integral was varied

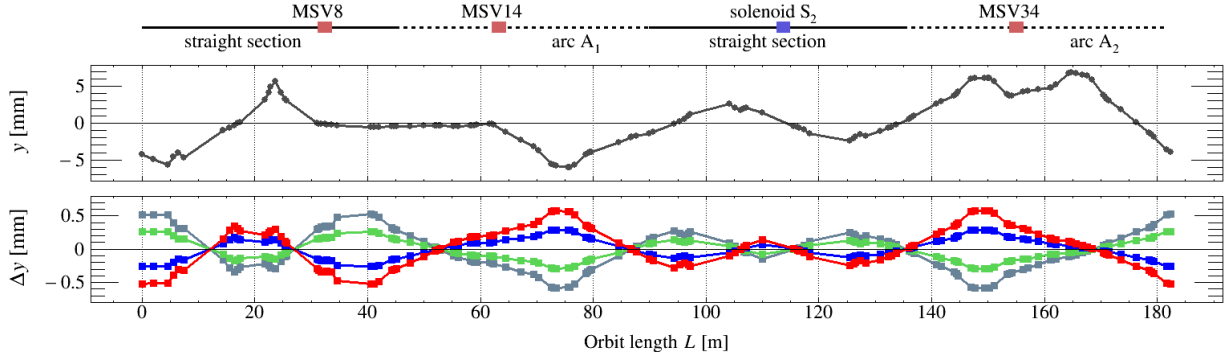


Fig. 1: Absolute beam position y [mm] indicate the vertical orbit for the vertical steerer set (top), when solenoid S_2 is switched off. The panel for Δy [mm] show the vertical orbit excursions with respect to the absolute beam positions when solenoid S_2 is switched on with a spin kick angle $\chi_{AI} = 13$ mrad, and rotated around the y -axis by $\xi_y = -8(\bullet), -4(\circ), 4(\blacklozenge),$ and $8(\color{red}\bullet)$ mrad. The observed excursions are linear in ξ_y .

producing the spin kicks in the range $\chi = [-13..13]$ mrad. Rotation of solenoid around Y -axis by ξ_y leads to vertical beam excursions (fig. 1), and has the most significant effect on the spin motion in the rest of the ring (fig. 2). Rotations of solenoid around X -axis (by ξ_x) lead to the changes of the spin tune jumps which are negligible (at the level of 10^{-9}). The reason for that can be, vertical field of the misaligned solenoid does not change beam energy due to zero dispersion in the straight section. Resulting horizontal orbit excursions does not lead to path lengthening integrally, and only non-commuting rotations of spin will produce the spin tune change. It will be a product of spin rotations due to vertical field perturbations and horizontal magnetic fields - an effect of quadratic smallness. Due to vertical orbit excursions in case of ξ_y misalignment of solenoid, horizontal field integral changes proportionally to the product of χ_{AI} and ξ_y . Spin rotation, representing spin transfer through all elements of the ring excluding the solenoid, is given in eq. 2 by \vec{c} and v_s^0 . We investigated how these values change relative to $\chi_{AI}\xi_y$ and $\chi_{AI}^2\xi_y$, so that deviation of spin tune map from prediction of eq. 2 can be specified. The changes of vector $\vec{c} = (c_x^0, c_y^0, c_z^0)$ are given by the changes of its horizontal components, $\delta c_x = c_x(\chi\xi) - c_x^0$ and $\delta c_z = c_z(\chi\xi) - c_z^0$ (fig. 2.(a)).

For the spin tune, $\delta v_s = v_s^0 - v_s(\chi, \xi)$. To illustrate symmetric/antisymmetric properties of the effects, we show the

$$\delta_{\pm}(\xi, \chi) = \frac{1}{2} [\delta v_s(\chi, \xi) \pm \delta v_s(-\chi, \xi)]. \quad (4)$$

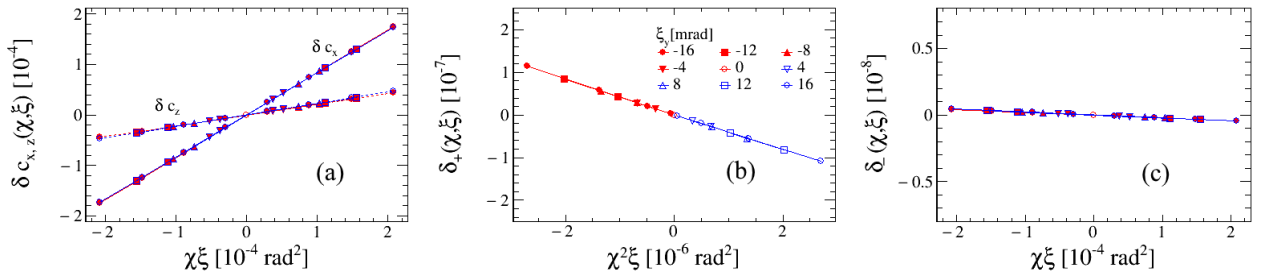


Fig. 2: Perturbation of \vec{c} and v_s^0 caused by the steereng effect of Y -axis solenoid rotation: the change of a) horizontal projections of spin rotation axis, b) symmetric term of spin rotation angle, c) antisymmetric term of spin rotation angle.

As we see on fig. 2.(b,c), δ_{\pm} exhibit different scaling properties as a function of ξ and χ . The slopes of $\delta_+(\chi^2\xi)$ and $\delta c_{x,z}(\chi\xi)$ lead to the calibration effect of the spin kick χ in eq. 1:

$$\chi \rightarrow \chi(1 + \delta k). \quad (5)$$

By testing different steerer settings, we found that δk does not depend on them. Based on simulation results (fig. 1), orbit excursions observed for the 100 keV solenoid in the spin tune mapping experiment, correspond to misalignment $\xi_y \approx 8$ mrad. This gives calibration factor $\delta k = 2.3 \cdot 10^{-4}$. However, the calibration factors for the fit of experimental spin tune map are by an order of magnitude larger. It means, some systematic effects are not yet implemented in our model in order to describe the data. Nevertheless, the effect of orbit excursion does not compromise the power of the technique. Determination of the spin tune map minima is possible when the change of horizontal field integral by the misaligned part of AI field is much smaller than the horizontal field integral of the ring itself. That is the case we had in the mentioned spin tune mapping study ([3]), where integral longitudinal field in the ring was $\approx 10^3$ times bigger than those generated due to misalignment of solenoid. Results of numerical simulations will help to determine a required accuracy for suppression of systematic effects in further EDM experiments.

^a Institut für Kernphysik, Forschungszentrum Jülich, Ger-

many, and Landau Institute, Chernogolovka, Russia.

* supported by the COSY–FFE program under contract number COSY-125 and a Grant from the Russian Science Foundation (grant number RNF-16-12-10151).

References:

- [1] F. Rathmann et al., *J. Phys.: Conf. Ser.* **012011**, 447 (2013).
- [2] D. Eversmann et al. (JEDI), *Phys. Rev. Lett.* **115**, 094801 (2015).
- [3] A. Saleev, N. Nikolaev, and F. Rathmann, *Int. J. Mod. Phys. Conf. Ser.* **40**, 1660093 (2016).

Simulation of Closed Orbit influencing Effects at COSY

V. Schmidt^{a,b} and A. Lehrach^{a,b,c} for the JEDI collaboration

The intended first direct measurement of an Electric Dipole Moment (EDM) of deuterons at the Cooler Synchrotron COSY [1] requires precise knowledge and control of the beam position. Therefore the analysis of closed orbit influencing effects is necessary. Displacement of magnets as well as residual power supply oscillations can lead to a change of the particles' trajectory through the ring. The spin motion could be influenced as well due to additional radial fields leading to false EDM signals. Assuming Gaussian distributed magnet misalignments with a standard deviation of 0.1 mm leads to a vertical closed orbit RMS¹ of around 1 mm. The resulting signal corresponds to an EDM of $d \approx 5 \cdot 10^{-19} \text{ e} \cdot \text{cm}$ [2]. With the current set-up of COSY, the vertical closed orbit RMS after applying an orbit correction is in the order of 2 mm. In order to reduce the contribution of a false EDM signal, its main sources must be identified. Using the MAD-X software [3] the effect of displaced magnets and power supply oscillations can be modeled by implementing the current COSY lattice and applying randomly distributed magnet displacements and field values.

Magnet misalignments

Considering first only magnet displacements, for each dipole and quadrupole six independent Gaussian distributed positioning errors (displacement along each axes, rotation around each axes) with the same standard deviation are generated according to

$$\Delta(x, y, s, \phi, \Theta, \Psi) = \text{Gauss}(0, \sigma_{x,y,s,\phi,\Theta,\Psi}), \quad (1)$$

with $\sigma_x = \sigma_y = \sigma_s$ and $\sigma_\phi = \sigma_\Theta = \sigma_\Psi$ and where $x, (y, s)$ describes the displacement along the x- (y-, s-) axes and ϕ (Θ, Ψ) indicates a rotation respectively. Including these magnet misalignments in the model, the closed orbit is simulated and the RMS is calculated in both transverse directions. For each standard deviation 100 random seeds are used and the results are considered before and after applying an orbit correction. The mean transverse RMS is shown in Figure 1 in vertical and horizontal direction including a linear fit to the data.

Power supply oscillations

In order to investigate the effect of residual power supply oscillations, a sinusoidal oscillation with an amplitude of $\Delta I_{\text{max}}/2$ is assumed (see Figure 2), where ΔI_{max} indicates the peak-to-peak value resulting from the relative errors and the maximum provided current of the power supplies. In Table 1 the values for each type of magnet at COSY are summarized [4]. Independently of the magnet type, its strength depends linearly on the current. Thus one can easily deduce the oscillation of the magnet strengths given its variation of the current [5]. Estimating the maximum effect of current oscillations, for each power supply an amplitude of the sine wave is randomly generated using a Gaussian distribution with a standard deviation of $\Delta I_{\text{max}}/2$. Since the magnitude of

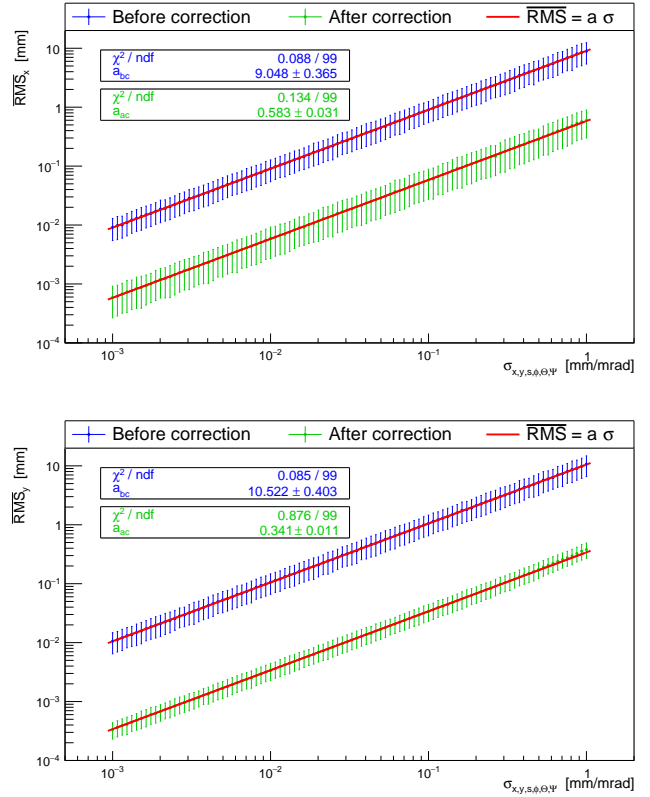


Fig. 1: Mean closed orbit RMS in horizontal and transverse direction. The blue markers indicate the results before an orbit correction is applied. The simulation results after the orbit correction are shown in green. The values result from generating magnet errors with 100 random seeds. The behavior is linear in both directions.

the current change is time dependent, additionally a random phase of the sinusoidal field variation is generated uniformly. The resulting value for the change in current is then given by

$$\Delta I = \text{Gauss}\left(0, \frac{\Delta I_{\text{max}}}{2}\right) \cdot \sin\left(\text{uniform}(0, 2\pi)\right). \quad (2)$$

Incorporating the generated field variations in the model and calculating the closed orbit leads to a snapshot of the dynamic scenario. By creating various of these snapshots one can investigate the average influence of power supply oscillations on the transverse closed orbit. In the simulation 1000 snapshots, i.e. 1000 closed orbits calculations, each for a different set of current values, are generated. For the reference orbit a fixed set of misaligned dipoles and quadrupoles was chosen. The deviations from the reference orbit at each BPM are collected in a histogram for all 1000 simulations and a Gaussian fit is performed. The width of the fit indicates the influence of the field oscillation at this specific BPM. The average width over all BPMs indicates the influence on the closed orbit RMS in x- (y-) direction due to field changes caused by residual power supply oscillations. The results for every magnet type are summarized in Table 2. None of the RMS changes is of a larger order of magnitude than $10 \mu\text{m}$.

¹Root Mean Square

Thus, regarding the precursor experiment at COSY, the residual power supply oscillations play a minor role when trying to improve the quality of the closed orbit to reach a transverse RMS of about $100 \mu\text{m}$ [2]. The effects of displaced and rotated magnets dominate the effect of power supply oscillations by many orders of magnitude.

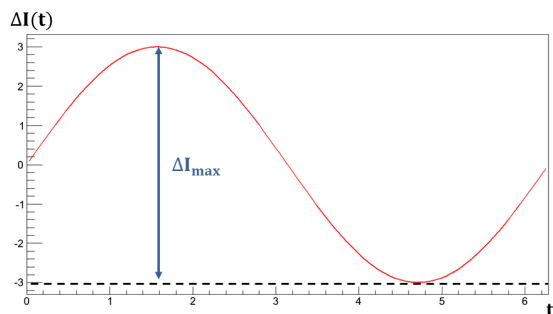


Fig. 2: Sketch of sinusoidal residual power supply oscillation. The peak-to-peak value is called ΔI_{max} . The typical frequency of the power supply oscillation is approximately 600 Hz.

Relative error on the current of the COSY magnets			
Magnet	σ [ppm]	I_{max} [A]	ΔI_{max} [A]
Dipole	20	5000	100
Quadrupole	20	550	11
Sextupole	500	275	137.5
Corrector	100	30	3

Table 1: Relative error and maximum current of COSY magnets.

Effect of power supply oscillations on the closed orbit RMS		
Magnet	ΔRMS_x	ΔRMS_y
Dipole	$(27.69 \pm 0.24) \mu\text{m}$	$(9.0 \pm 0.1) \text{nm}$
Quadrupole	$(1.11 \pm 0.01) \mu\text{m}$	$(0.7 \pm 0.01) \mu\text{m}$
Sextupole	$(48.7 \pm 0.9) \text{nm}$	$(49.9 \pm 0.6) \text{nm}$
Corrector	$(34.43 \pm 0.30) \mu\text{m}$	$(28.07 \pm 0.22) \mu\text{m}$

Table 2: Influence of residual power supply oscillations of the COSY magnets on the closed orbit RMS.

Survey at COSY

The former results show that magnet misalignments are one of the main sources of closed orbit deviations at COSY. It is therefore necessary to determine the current positions of all dipoles and quadrupoles and to correct large displacements and rotations towards the target position. A corresponding survey was conducted in April 2016 by the external company Stollenwerk. The dipoles and quadrupoles at COSY are armed with reference marks at which a laser-based position measurement according to a fixed reference point can be carried out. The positioning of these marks on the magnet is sketched in Figure 3 [6].

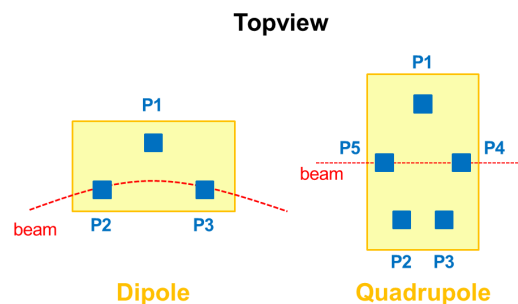


Fig. 3: Topview on magnets: Reference marks on dipoles and quadrupoles. For dipoles the marks P2 and P3 are the closest to the beam path. In the case of a quadrupole, the marks P4 and P5 lie directly above the ideal beam trajectory through the magnet. [6]

Taking the first dipole in the left arc as the reference point, the relative vertical displacement of all other dipoles is measured. The same procedure is used for the quadrupoles, taking the first quadrupole after the injection point as the reference element. Given these information a best-fit-plane to which all elements afterwards should be optimally positioned was estimated. The best-fit-plane is found by taking the vertical measurement results and fitting a plane to the values which minimizes the vertical deviations. It turned out that taking only the reference marks P2 and P3 of the dipoles into account leads to the best result for the fitted plane. Ignoring some outliers of the measurement points further improves the result [6]. Finally, the deviations of all magnets from the achieved best-fit-plane were calculated in each direction using the different reference marks. Implementing the measured magnet misalignments into the COSY model leads to the uncorrected closed orbit shown in Figure 4. The closed orbit RMS values are similar to the ones that are measured at COSY which supports the assumption that magnet misalignments are the main source for closed orbit deviations [7].

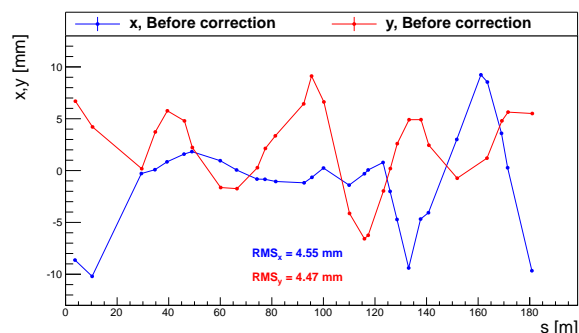


Fig. 4: Simulated closed orbit before an orbit correction resulting from magnet misalignments taken from the survey data. The closed orbit RMS in the uncorrected case is similar to measured RMS values at COSY. Also the whole pathway of the uncorrected closed orbits show similarities to the measured orbits.

References:

- [1] A. Lehrach, B. Lorentz, W. Morse, Precursor Experiments To Search For Permanent Electric Dipole Moments (EDMs) of Protons and Deuterons at COSY, 2011
- [2] M. Rosenthal, A. Lehrach, Spin Tracking Simulations Towards Electric Dipole Moment Measurements at COSY, in Proceedings 6th International Particle Accelerator Conference, IPAC15, Richmond, VA, USA (2015), <http://jacow.org/IPAC2015/papers/thpf032.pdf>
- [3] Methodical Accelerator Design, <http://mad.web.cern.ch/mad/>
- [4] M. Retzlaff, private communication
- [5] K. Wille, Physik der Teilchenbeschleuniger und Synchrotronstrahlungsquellen, edition 2, 1996, Springer Fachmedien
- [6] Vermessungsbüro Dipl.-Ing. H.J.Stollenwerk, private presentation
- [7] F. Hinder, M. Rosenthal, F. Trinkel, Beam Position Monitors at COSY, 2015

^a Institute for Nuclear Physics IV , FZ Jülich, Germany

^b Physics Institute III B, RWTH Aachen University, Germany

^c JARA-FAME

Production of η -mesons in pn-collisions at ANKE *

D. Schröder[†], C. Fritsch, A. Khoukaz, M. Rump for the ANKE-Collaboration

To study the possible formation of η -mesic nuclei the production of η -mesons was measured at ANKE via the quasi-free reaction $p + d \rightarrow d + \eta + p_{sp}$. In this case the deuteron is used as an effective neutron target while the proton acts as a spectator particle. Two different beam momenta ($p_1 = 2.09$ GeV/c and $p_2 = 2.25$ GeV/c) in combination with the Fermi motion inside the target deuteron allow to obtain total and differential cross sections in a region from threshold up to an excess energy of $Q = 90$ MeV (Fig. 1).

The course of the cross section, especially near threshold, will give access to information about the final state interaction (“FSI”) between the η -meson and the deuteron.

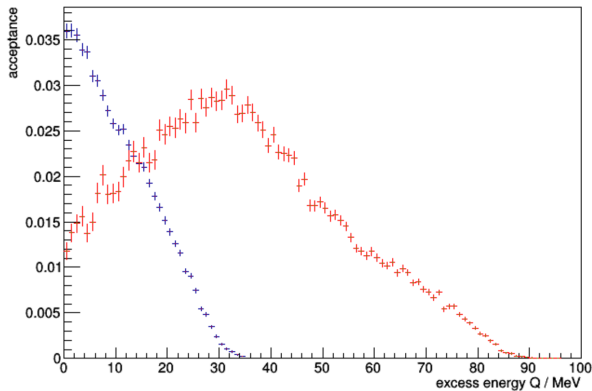


Fig. 1: Acceptance of the reaction $p + n \rightarrow d + \eta$ in blue for $p_1 = 2.09$ GeV/c and in red for $p_2 = 2.25$ GeV/c

For this two particle final state the cross section can be written as

$$\frac{d\sigma}{d\Omega} = \frac{p_f}{p_i} \cdot |f(\vartheta)|^2, \quad (1)$$

with the final/initial state momentum being p_f/p_i and the production amplitude f . This amplitude can be splitted into an energy independent amplitude f_{prod} and the final state interaction term FSI. It can then be rewritten as

$$|f(\vartheta)|^2 = |f_{prod}|^2 \cdot |FSI|^2 = \frac{|f_{prod}|^2}{|1 - iap_f|^2} \quad (2)$$

with the complex scattering length a , which describes the strength of the $d\eta$ final state interaction [1]. Different to the final state interaction, which could vary strongly at threshold, the production amplitude is expected to expose only a weak energy dependence.

The identification of this reaction is achieved via the Missing Mass method. In order to do so, two particles in the final state have to be measured. The deuteron is detected in the forward system and identified by the energy loss [2] while the spectator proton in registered in one of two Silicon Tracking Telescopes.

To subtract the multi-pion background, a method developed by the SPESIII Collaboration [3] is used [4] and the result is shown in Fig.2. The resulting count rates have to be corrected

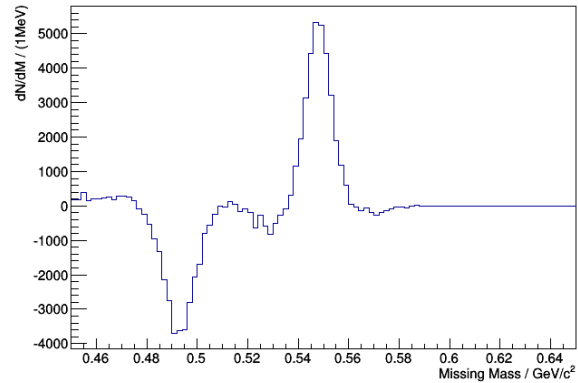


Fig. 2: Difference between the missing mass spectra for both beam momenta. The right, positive peak corresponds to the first beam energy, while the left, negative peaks is a result of the subtraction of the events of the second beam energy.

for acceptance and Fermi motion inside the target deuteron as the latter causes different effective luminosities for every Q value. A preliminary analysis with unnormalized cross sections are shown in Fig.3. A fit to the data using Eq. 1 and 2 already describes the data nicely. However, in the final analysis further effects like finite beam energy smearing have to be considered. This is currently in progress.

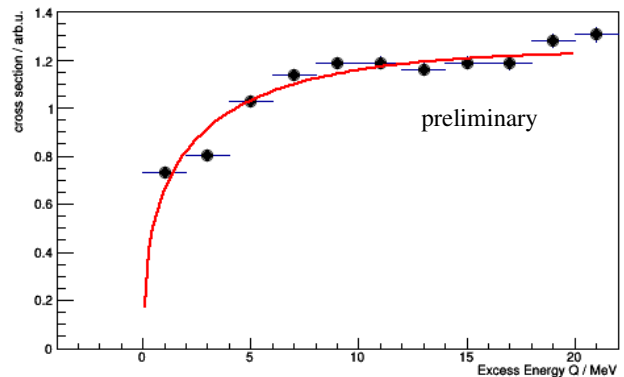


Fig. 3: Preliminary cross section of the reaction $p + n \rightarrow d + \eta$. In red the fit with Eq. 1 and 2 is shown.

In total, approximately 100k events of the reaction $p + n \rightarrow d + \eta$ have been gathered in agreement with expected count rates [5]. A preliminary scattering length could be determined via the course of the total cross section but the differential cross sections will be investigated to determine the limit for the s -wave FSI-ansatz. Additionally the calculation of the luminosity via elastic scattering is on its way to allow to value the total cross section.

References:

- [1] C. Wilkin et al., Phys. Lett. B 654, 92-96, 2007
- [2] M. Rump et al., Annual report (2015)
- [3] F. Hibou et al., Phys. Rev. Lett. 83, (1999) 492.
- [4] D. Schröder et al., Annual report (2015)
- [5] A. Khoukaz et al, COSY proposal #211 (2012)

*Supported by COSY-FFE

[†]Institut für Kernphysik, Westfälische Wilhelms-Universität, 48149 Münster, Germany

QUASI-FROZEN SPIN CONCEPT OF DEUTERON STORAGE RING AS INSTRUMENT TO SEARCH ELECTRIC DIPOLE MOMENT

Y. Senichev

IKP, Forschungszentrum Jülich, Germany

INTRADUCTION

Currently, the “Jülich Electric Dipole Moment Investigation” (JEDI) collaboration works in two directions: first on the existing accelerator COSY the precursor experiment is carried out to prove the feasibility of EDM measurement using the storage ring, and secondly the conceptual design of the ring specifically for search of the deuteron electrical dipole moment (dEDM) is being developed. At present we have already obtained very important experimental results with precise measurements of the spin precession frequency [1,2] which will allow calibrating the particle energy using the clock-wise and counter clock-wise procedure, and we have reached the longest spin coherence time ~ 1000 sec in horizontal plane [3].

At present there are two options of future dEDM ring based on the frozen (FS) and quasi-frozen spin (QFS) concepts [4]. The idea of FS concept has been suggested by BNL [5], and it is based on the elements with incorporated electric and magnetic fields in one element, when the spin of the reference particle is always orientated along the momentum.

Studying the FS structure, we have paid attention to the fact that the frozen spin condition is performed only for the reference particle, and the spin vector of all other particles oscillates relative the frozen direction. But if so, it might not be worth it to strictly fulfill the frozen spin condition even for the reference particle. Let us see if the spin oscillates in the horizontal plane with respect to the frozen spin direction with amplitude Φ_s , then the EDM growth decreases proportionally to the factor $J_0(\Phi_s) \approx 1 - (\Phi_s)^2/4$. Taking into account that the deuteron’s anomalous magnetic moment $G = -0.142$ has a small value and the fact that the spin oscillates around the momentum direction within half value of the advanced spin phase $\pi \cdot \gamma G/2$ in the magnetic arc, each time returning in the elements with electrical field on the straight sections, it is obvious that the effective contribution to the expected EDM effect is reduced only by a few percent. This allows us to proceed to the concept of quasi-frozen spin QFS [6], where the spin is not frozen with respect to the momentum vector, but continually oscillates around momentum with small amplitude of few degrees.

In case of the quasi-frozen spin concept, we have two options of lattice. In the first option, the electrical and magnetic fields are fully spatially separated in arcs and straight section elements.

In second option of QFS lattice we introduced a magnetic field of small value ~ 100 mT, compensating the Lorentz force of the electric field on straight section (see fig.1).

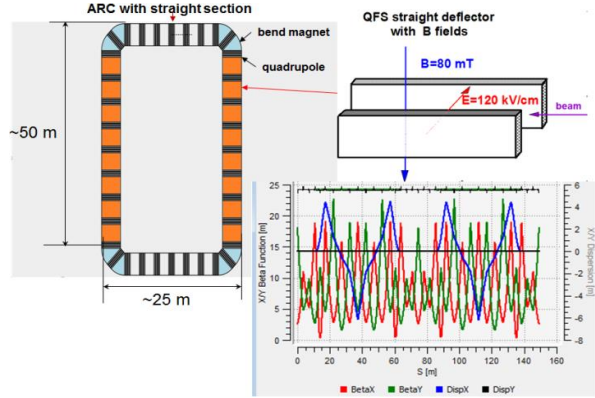


Figure 1: QFS lattice with TWISS functions.

In both cases the QFS lattice has the conventional magnetic arcs with the zero dispersion on the straight sections in the middle for installation of the polarimeter, the beam extraction and injection systems, and the RF cavity.

The QFS concept simplifies the EDM lattice and makes it possible to realize QFS concept in existing COSY ring to search for dEDM.

SYSTEMATIC ERRORS

Generally, the measurement errors can be divided into two components: random errors and systematic errors. The systematic error is called the error component, which remains constant in repeated measurements and is caused by imperfections of the physical facility. In the EDM ring experiment, the systematic error arises due to the misalignments of electric and magnetic elements in the ring and causes a “fake” EDM signal. The nature of origin being random errors, the misalignments create conditions for systematic errors in EDM experiments. The installation errors (misalignments) are associated with limited capabilities of the geodetic instruments. As is known, the bending magnet (or the electric deflector) can be rotated in three planes. We consider only the rotation around the longitudinal and transverse axis, because the rotation around the vertical axis does not introduce a systematic error.

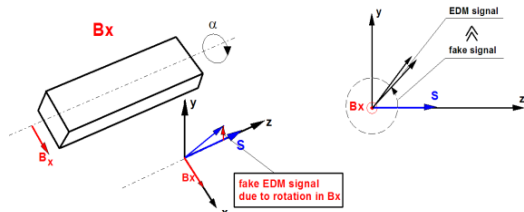


Figure 2: Magnet rotating relative to longitudinal axis.

First, let us consider the case of the magnet rotated relative to the longitudinal axis (see Fig.2). Due to such rotation, a horizontal component of the magnetic field B_x arises and causes the spin rotation $\Omega_x = \Omega_{Bx}$ in the same plane where we expect the EDM rotation. To illustrate, let us write the solutions of T-BMT equations with initial condition $S_x = 0, S_y = 0, S_z = 1, \Omega_z = 0$ and $\Omega_x \neq 0$ in simplest form:

$$S_x(t) = \frac{\Omega_y \sin(\sqrt{\Omega_x^2 + \Omega_y^2} t)}{\sqrt{\Omega_x^2 + \Omega_y^2}}; S_y(t) = -\frac{\Omega_x \sin(\sqrt{\Omega_x^2 + \Omega_y^2} t)}{\sqrt{\Omega_x^2 + \Omega_y^2}}. (1)$$

Taking into account the above, we can present components: $\Omega_x = \Omega_{EDM} + \Omega_{Bx}$ and $\Omega_y = 0 + \delta\Omega_{decoh}$,

where Ω_{EDM} is the frequency of spin rotation due to the presence of an EDM, B_x is the horizontal component induced by the magnet rotation (misalignments), and $\delta\Omega_{decoh}$ is the spin tune decoherence in the horizontal plane. Since the decoherence is allowed to reach an rms value of 1 rad for spin coherence time $t_{SCT} > 1000$ sec, that is the rms value of $\langle \delta\Omega_{decoh} \rangle \approx 10^{-3}$ rad/sec.

The magnets are supposed to be installed at the technically realized accuracy of $10\mu\text{m}$, which corresponds to the rotation angle of the magnet around the axis of about $\alpha_{max} = \pm 10^{-5}$ rad. Using COSY Infinity [7] and MODE [8], we have calculated the MDM spin rotation due to B_x , which is $\Omega_{Bx} \approx 3$ rad/sec. At the same time, at presumable EDM value of 10^{-29} e·cm, the EDM rotation should be $\Omega_{EDM} = 10^{-9}$ rad/sec, that is $\Omega_{EDM} / \Omega_{Bx} \approx 10^{-9}$, and the expression (1) can be simplified without loss of measurement accuracy of possible signal EDM at the level of 10^{-9} :

$$\langle S_x(t) \rangle = \frac{\langle \delta\Omega_{decoh} \rangle}{\Omega_{Bx}} \sin \Omega_{Bx} t; S_y(t) = -\sin(\Omega_{Bx} + \Omega_{EDM}) t. (2)$$

We can see from the first equation of (2) that the spin decoherence in the horizontal plane is not growing and is stabilized at the level of $\langle S_y \rangle \sim \langle \delta\Omega_{decoh} \rangle / \Omega_{Bx} \approx 10^{-3}$. This is a significant positive feature. But to be fair, we should understand that, since $\Omega_{Bx} = \frac{e}{m\gamma} (\gamma G + 1) B_x$, we will now get due to $\gamma = \gamma_0 + \Delta\gamma$ the spin frequency decoherence $\Omega_{Bx} = \Omega_{x,\gamma=\gamma_0} + \Delta\Omega_{x,\Delta\gamma}$ in the vertical plane around horizontal axis, which one we can minimize by the same methods (sextupoles, RF) as in horizontal plane. In addition, we are really deprived of ability to measure the accumulated EDM signal by growth of the vertical component of spin suggested in [5], since the spin

rotation due to the magnet errors is much faster than due to possibly existing EDM $\Omega_{Bx} \gg \Omega_{EDM}$. That is S_y reach a maximum for very short time meanwhile the signal EDM does not have time to be accumulated.

Therefore, the only solution is to measure the total frequency $\Omega_{Bx} + \Omega_{EDM}$, but in order to split out the EDM signal from the sum signal, we need an additional condition. Such a condition is to measure the total spin frequency in the experiment with a counter clock-wise (CCW) direction of the beam $\Omega_{CCW} = -\Omega_{Bx}^{CCW} + \Omega_{EDM}$ and compare with clock-wise (CW) measurements $\Omega_{CW} = \Omega_{Bx}^{CW} + \Omega_{EDM}$. Simultaneously, we must understand that the accuracy of the frequency measurement of $\Omega_{CW}, \Omega_{CCW}$ determines the precision of the EDM measurement.

Let us assume that we can measure the spin frequencies $\Omega_{CW}, \Omega_{CCW}$ with accuracy $\Delta\Omega_{CW,CCW} = 10^{-9}$, detailed discussion of which one is handed of the scope of this article. Then we will be able to determine the EDM signal by

simple addition $\Omega_{EDM} = (\Omega_{CW} + \Omega_{CCW})/2 + (\Omega_{Bx}^{CCW} - \Omega_{Bx}^{CW})/2$ at the level of $\sim 10^{-29}$ e·cm. The additional orders of magnitude can be obtained by the time modulation of the ‘‘diamond pellets’’ target (frequency of following diamonds) and higher detector rate [9]. It would allow having bigger number of useful events in the interval when the polarization asymmetry changes faster and having the smaller statistic errors. Thus, such an approach looks promising.

However, we need to be sure that when the sign of the driven magnetic field B_y for the CW-CCW is changed, the magnetic field component B_x is restored with the required relative precision of not lower than 10^{-10} . Therefore, we suggest calibrating the field in the magnets using the relation between the beam energy and the spin precession frequency in the horizontal plane, that is, determined by the vertical component B_y . Since the magnet orientation remains unchanged, and the magnets are fed from one power supply, the calibration of B_y will restore the component B_x with the same relative accuracy 10^{-10} , which applies to the difference $\Omega_{Bx}^{CCW} - \Omega_{Bx}^{CW}$ as well. Besides, we should mention that the calibration in the horizontal plane does not involve the EDM signal. Thus, this calibration will not decrease the accuracy of EDM measurement, and it will be finally defined by accuracy of $\Omega_{CW,CCW}$ measurement.

We shall not discuss here the other systematic errors arising from the rotation of the magnet with respect to the longitudinal axis, because it does not mix EDM and MDM signal and is quite well discussed in [10].

CONCLUSION

In the paper, we analyzed the frozen and quasi-frozen spin structures, taking into account the effect of spin decoherence and systematic errors. It has been shown how you can measure the EDM in an imperfect ring using achieved the experimental results of spin tune measurement and the beam polarization lifetime of 1000 sec. In the proposed conception we use: the calibration energy in horizontal plane and measurement in vertical plane, the invariability of ratio B_x to B_y after change of polarity in all elements. These estimates show that the lower limit of detection of presumably existing EDM can be as low as $\sim 10^{-29}$ e·cm.

REFERENCES

- [1] Z. Bagdasarian et al., Measuring the polarization of a rapidly precessing deuteron beam, Phys. Rev. ST Accel. Beams 17, 052803 (2014)
- [2] D. Eversmann et al., New method for a continuous determination of the spin tune in storage rings and implications for precision experiments, Phys. Rev. Lett. 115, 094801 (2015)
- [3] G. Guidoboni, et al., How to reach a thousand-second in-plane polarization lifetime with 0.97-GeV/c deuterons in a storage ring, Phys. Rev. Lett. 117, 054801, (2016)
- [4] Y.Senichev et al., Investigating of lattice for deuteron EDM ring, Proceedings of ICAP 2015, Shanghai, China, pp. 17-19
- [5] D. Anastassopoulos et al., "AGS Proposal: Search for a permanent electric dipole moment of the deuteron nucleus at the $10\text{--}29$ e · cm level", BNL, 2008.
- [6] Yu.Senichev et al., Quasi-frozen Spin Method for EDM Deuteron Search, Proceedings of IPAC2015, Richmond, VA, USA
- [7] M. Berz, "Computational Aspects of Design and Simulation: COSY INFINITY", NIM A298, (1990).
- [8] Ivanov A. et al., (2014), "Matrix Integration of ODEs for Spin-orbit Dynamics Simulation", Proc. of IPAC2014, Dresden, Germany, 400-402.
- [9] I.Keshelashvili, Towards JEDI Polarimetry, XVIth International Workshop in Polarized Sources, Targets, and Polarimetry, PSTP2015, Bochum, Germany
- [10] Yu.Senichev, et al., Systematic Errors Investigation in Frozen and Quasi-Frozen Spin Lattices of Deuteron EDM Ring, Proceedings of IPAC2016, Busan, Korea

Developments for the EDM polarimeter at COSY

D. Shergelashvili^{a,b}, O. Javakhishvili^{a,c}, M. Gagoshidze^c, D. Mchedlishvili^a, I. Keshelashvili^d, F. Müller^{d,e} and A. Kacharava^d
for the JEDI collaboration

This report covers the current status of the readout system development for the JEDI polarimeter detector and of the power supply modules recently used in the second beam tests of LYSO modules at COSY. The final detector will be modular, containing few hundreds of modules. The main goals for the precision polarimetry are to develop a high speed - high efficiency data acquisition, online analysis and slow control systems. This will allow tracking down the tiny changes of the polarization axis of charged particles in real time, providing information on charged particle EDMs. The data acquisition system will employ FPGA based fast Flash ADCs which allow wide range of features and configurations. The analyses part of the readout system will be adapted to multithreaded operation to handle high count rates at high complexity levels of analyses.

During two beam tests of the LYSO modules at COSY an initial version of the readout system has been successfully used. Experimental data from the detector modules as well as from the additional detectors (start, stop, dE/E, VETO...) are read out by FADCs and saved in a cluster format. The data distributor system, in parallel, distributes the readout data across the network. The online analysis tools which are connected to the data stream from the distributor analyze the data in real time. A block diagram of the whole system is shown on Fig.1.

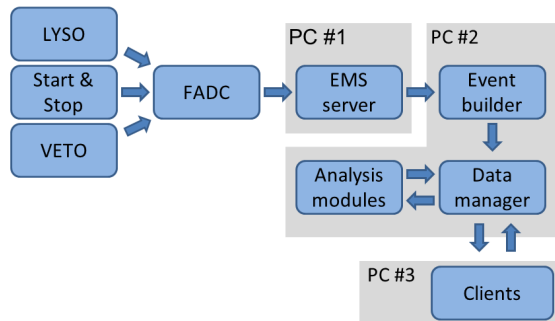


Fig. 1:
Block diagram of the current version of the data readout and online analysis system for the JEDI polarimeter detector.

In the first beam tests only four LYSO modules were measured. Together with additional start/stop and VETO counters these fitted in to one FADC module (32 channels). However, it became necessary to employ two of them to handle 24 LYSO modules and additional plastic scintillators during the second beam tests. The two FADCs modules were operating in a synchronous mode, internally triggered from any FADC channel and showed a flawless performance. In addition to more advanced configuration of the FADC

modules for the second beam tests, the online analysis software was also updated to implement more complex analyses. The thin dE/E plastic scintillators which were placed in front of the LYSO modules, allowed us to more clearly identify elastically scattered deuterons in the $\bar{d}C$ interaction process. Two dimensional dE vs E plots were prepared for direct monitoring of elastic deuterons. Besides, the spin state information, provided by the COSY ProfiBus system, was also included in the data stream and implemented in the online analysis software. This allowed the online monitoring of the measured asymmetries.

Furthermore, another subject of development became clear after the first beam tests. SiPMs, which will be used in all modules of the final detector, are very sensitive to the bias voltage, unlike conventional photo multiplier tubes. During the laboratory tests a near-to-exponential dependence was observed between the SiPM's gain and the biasing voltage. At normal operational voltages of $30 \div 32$ V a change of 1 mV in the biasing voltage introduces the change in the gain of the SiPM of around $0.02 \div 0.05$ %. This can have significant impact on the resolution and the linearity of the whole detector module. Besides, although the average current consumption by the SiPM array of a single module is in the few mA range (depending on the rate), the amplitude of the pulses during the detection can reach 100 mA and more (per channel). All these put quite high requirements on the characteristics of the power supply for the SiPMs. Since the final detector will consist of hundreds of modules, the voltage supply should also be modular, with the ability to control each channel remotely, have very high short/long term stability, high temperature stability, very good dynamic performance characteristics and, most importantly, low noise.

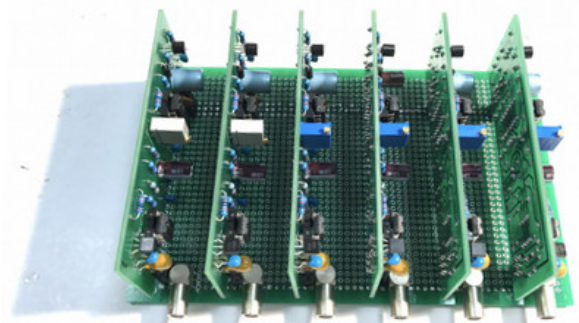


Fig. 2:
Power supply board (one out of four) with six voltage regulator modules on it.

The majority of multi-channel power supplies, currently available on the market, fail to simultaneously fulfill all the requirements mentioned above. Therefore, a new supply development started for the second beam tests. The first version, which was successfully used during these tests, is based on the integrated precision voltage regulator circuit LM723. In addition to the main features of LM723, such as current limitation, voltage regulator modules are also provided to have manual output voltage adjustment ability and output enable/disable pin, which was connected with a Raspberry Pi system and controlled remotely via a network connection. During enabling/disabling the output, an additional circuit was developed to slowly ramp the output from zero to the nominal value and back. Every six modules were placed on a supporting PCB which provided input/output and controlling connections and also the physical support to the whole assembly, as shown on Fig. 2. Four such boards, holding 24 channels in total, were placed on the specially designed metallic construction allowing to mount the whole supply on a standard rack. The LM723 regulators were supplied from an external voltage reference MAX6350 to further improve the noise figure and the stability of the output voltage. The developments discussed in this report will be continued. More design reports and test results will follow soon. This work is supported by SRNSF, Georgia.

^a SMART|EDM_Lab, HEPI, TSU

^b Tbilisi State University

^c Agricultural University of Georgia

^d IKP, Forschungszentrum Jülich

^e RWTH Aachen

Measurements of the new HESR pick-up at COSY

B. Breikreutz, N. Shurkhno, R. Stassen, H. Stockhorst

Introduction

Forschungszentrum Jülich is responsible for the development and commissioning of the HESR facility at FAIR. In the frame of this work first pick-up for stochastic cooling was manufactured and thoroughly measured in a test-bench and with the beam at COSY within 2015-2016. The measurements include transverse and longitudinal signals of the pick-up, signals from each single direction. Based on the longitudinal Schottky spectra the normalized longitudinal amplitude response of the pick-up was also calculated.

Pick-up structure

HESR pick-up is described in detail in [1]. Fig. 1 shows manufactured pick-up before placement into the beam pipe:

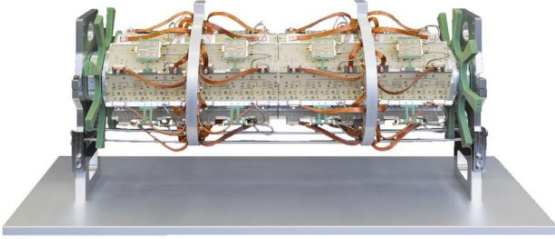


Fig. 1: Manufactured HESR pick-up.

It represents the stack four slot-ring couplers with 16 rings each. The electrodes in each 16-ring structure are immediately combined in pairs corresponding to top, bottom, left and right directions, providing four outputs for each structure. Then outside of the tank the outputs are consequently combined with proper delays, allowing to work with all degrees of freedom at the same time.

At first, the new pick-up was thoroughly measured in a test-bench, the measurements included reflections from each output, transmission between different outputs and structures. All measurements were performed both at room and cryogenic temperatures.

Measurements with the beam

After test-bench measurements, the pick-up was installed at the COSY ring, replacing old vertical pick-up, and measurements with the beam were carried out.

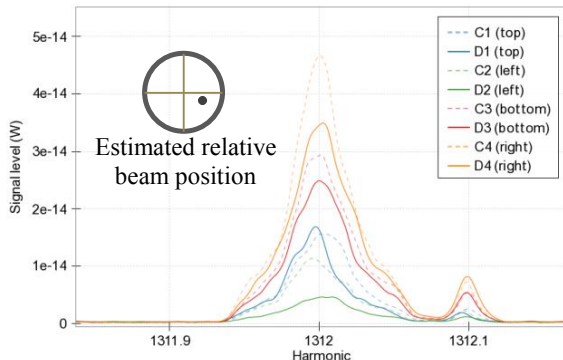


Fig. 2: Measured signals from top, bottom, left and right outputs of two 16-rings structures.

Fig. 2 shows signals from each output (top, left, right and bottom) of two consequent 16-rings structures. The structure is sensitive enough to the beam displacement, allowing to use the pick-up also as a beam-position monitor.

Vertical and horizontal signals measured with the pick-up are shown in Fig. 3, the intensity of the proton beam was $8 \cdot 10^8$. The signals have different amplitudes due to different beam displacements in vertical and horizontal directions.

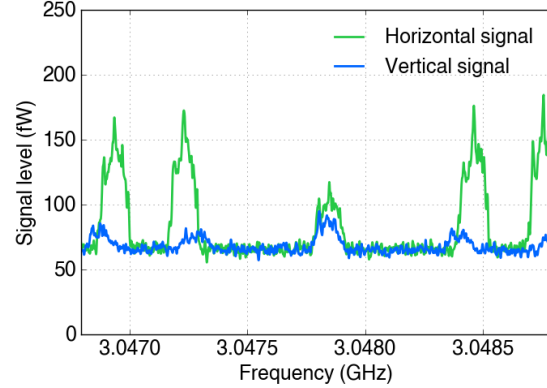


Fig. 3: Measured horizontal and vertical signals for $8 \cdot 10^8$ protons.

In addition, many measurements were carried out, comparing the signals for different combinations of modules and for different intensities, showing that pick-up is linear and works properly.

Longitudinal amplitude response

Spectrum analyzer measures signal proportional to the sum of two components – beam signal (Schottky noise) and hardware noises, corresponding spectral density could be written as [2]:

$$\frac{dP_{SA}}{df} = G^2(P_{Sch} + P_{Th}),$$

where G – transfer function of hardware after the pick-up, P_{Sch}, P_{Th} – Schottky and thermal spectral powers, which are given by

$$P_{Sch} = n_p Z_p Z_0 \times 2(e f_0)^2 \Psi_n(f),$$

$$P_{Th} = k(T_A + T_0) Z_0,$$

where n_p – number of pick-ups, Z_p – pick-up coupling impedance, Z_0 – system impedance, e – elementary charge, f_0 – revolution frequency, Ψ_n – particle distribution function at n -th harmonic, k – Boltzmann constant, T_A – effective amplifier temperature, T_0 – pick-up temperature.

We rewrite spectral analyzer signal, introducing the noise-to-signal ratio $NS = P_{Th}/P_{Sch}$:

$$\frac{dP_{SA}}{df} = G^2 P_{Sch} (1 + NS).$$

Distribution function at n -th harmonic is expressed as:

$$\Psi_n = \frac{dN}{df} = \frac{1}{n} \frac{dN}{df_p} = \frac{1}{n} \Psi.$$

Approximating distribution function Ψ with normal distribution, the noise-to-signal ratio at the center of the n -th Schottky band could be written as

$$NS = \frac{k(T_A + T_0)\sqrt{2\pi}n\eta\Delta p/p}{n_p Z_p 2e^2 f_0 N},$$

which for the present system is around 0.01, and thus could be neglected.

System transfer function G is defined mainly by preamplifiers G_A and cables G_C from pick-up to spectrum analyzer. Preamplifiers used in the experiment have flat enough frequency response, so could be considered constant, while cables have frequency dependent attenuation $G_C = 0.35\sqrt{f} + 0.04f$ per meter.

Finally, the spectrum analyzer signal could be written as

$$\frac{dP_{SA}}{df} = G_A^2 G_C^2 2(e f_0)^2 \Psi Z_0 \frac{Z_P}{n}.$$

Then we introduce a function, that depends on the unknown pick-up impedance:

$$F = \frac{n}{G_C^2} \frac{dP_{SA}}{df} = G_A^2 2(e f_0)^2 \Psi Z_0 \times Z_P.$$

Normalizing this function with a value at arbitrary frequency f_1 we can define the function for the pick-up normalized amplitude dependence:

$$F_{Norm}(f) = \frac{F(f)}{F(f_1)} = \frac{Z_P(f)}{Z_P(f_1)}.$$

This function could be calculated directly from the measurements and compared with the simulation results. Following figure shows measured longitudinal signals from the new pick-up:

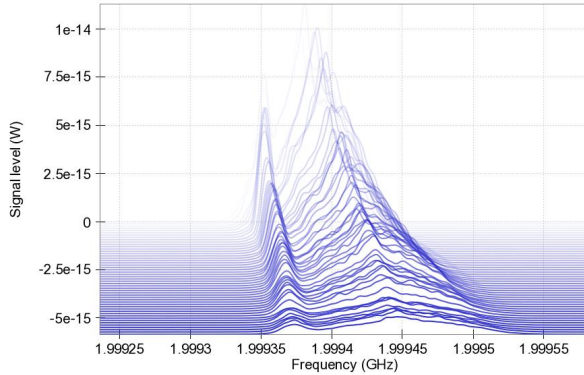


Fig. 4: Waterfall plot of longitudinal Schottky bands, less transparent lines correspond to higher frequencies, frequency axis is shown for the first Schottky band for reference.

Calculating function F_{Norm} for the centers of measured longitudinal Schottky bands we obtain normalized amplitude response of the pick-up. Fig. 5 shows calculated responses from horizontal and vertical electrode pairs' sums as well as simulated pick-up response:

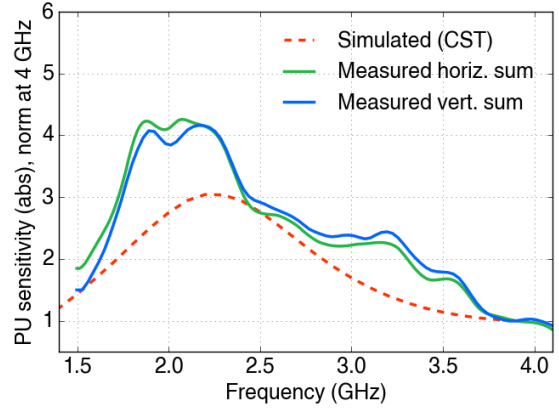


Fig. 5: Calculated and simulated pick-up amplitude responses.

Despite of rather rough calculations, the theoretical and experimental results show reasonable agreement, proving that pick-up works as expected.

Outlook

The first pick-up for the HESR stochastic cooling system was manufactured and successfully tested at COSY. The signals from each direction as well as transverse and longitudinal signals were measured with the beam, showing excellent pick-up performance. Pick-up normalized amplitude response was calculated from longitudinal spectra, showing reasonable agreement with the simulation. Essentially the work on the HESR stochastic cooling system is on schedule.

References

- [1] Stassen, R., Stockhorst, H., Katayama T., Thorndahl L. (2011). The stochastic cooling system of HESR. In proceedings of COOL'11 conference (pp. 129-131).
- [2] Möhl D. (1995). Stochastic cooling. In proceedings of CERN Accelerator School'93 (pp. 587-681).

Search for η -mesic ${}^4\text{He}$ in the $dd \rightarrow {}^3\text{He}n\pi^0$ and $dd \rightarrow {}^3\text{He}p\pi^-$ reactions with the WASA-at-COSY facility

M. Skurzok^a, W. Krzemień^b, P. Moskal^a

We performed the search for ${}^4\text{He}$ - η bound states with the WASA-at-COSY facility via the measurement of the excitation function for the $dd \rightarrow {}^3\text{He}n\pi^0$ [1–3] and $dd \rightarrow {}^3\text{He}p\pi^-$ [1, 2] processes. The deuteron beam momentum was varied continuously between 2.127 GeV/c and 2.422 GeV/c, corresponding to the excess energy for the $dd \rightarrow {}^4\text{He}\eta$ reaction ranging from $Q = -70$ MeV to $Q = 30$ MeV. The luminosity was determined based on the $dd \rightarrow {}^3\text{He}n$ reaction and the quasi-free proton-proton scattering via $dd \rightarrow ppn_{\text{spectator}}n_{\text{spectator}}$ reactions [4], while the overall detection and reconstruction efficiencies were determined based on the Monte Carlo simulation for the $dd \rightarrow ({}^4\text{He}\eta)_{\text{bound}} \rightarrow {}^3\text{He}n\pi^0$ and $dd \rightarrow ({}^4\text{He}\eta)_{\text{bound}} \rightarrow {}^3\text{He}p\pi^-$ processes taking into account response of detection system and selection criteria applied in the data analysis. The excitation functions, determined independently for the measured reactions, do not reveal a structure which could be interpreted as a narrow mesic nucleus. Therefore, the upper limits of the total cross sections for the bound state production and decay in $dd \rightarrow ({}^4\text{He}\eta)_{\text{bound}} \rightarrow {}^3\text{He}N\pi$ processes were determined taking into account the isospin relation between the both of the considered channels, which state that the probability of $p\pi^-$ pair production is two times higher than in case of $n\pi^0$ production. The obtained results are presented in Fig. 1.

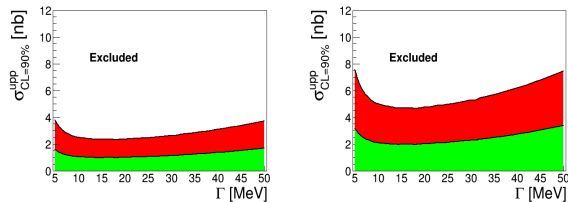


Fig. 1: Upper limit of the total cross-section for $dd \rightarrow ({}^4\text{He}\eta)_{\text{bound}} \rightarrow {}^3\text{He}n\pi^0$ (upper panel) and $dd \rightarrow ({}^4\text{He}\eta)_{\text{bound}} \rightarrow {}^3\text{He}p\pi^-$ (lower panel) reaction as a function of the width of the bound state. The binding energy was fixed to 30 MeV. The upper limit was determined via the simultaneous fit for both channels. The green area denotes the systematic uncertainties. The figure is adapted from Ref. [1].

The upper limits vary from 2.5 to 3.5 nb for the first process and from 5 to 7 nb for the second process for the width ranging from 5 to 50 MeV, when assuming that the momentum distribution of N^* in the $N^*{}^3\text{He}$ system is the same as momentum distribution of nucleons in the ${}^4\text{He}$ nucleus (red solid line in Fig. 2). However, these upper limits increase by the factor of 1.7 when assuming in the analysis that the N^* momentum distribution is given by the results of the recently proposed model [5] (dashed line in Fig. 2).

The excitation function for the $dd \rightarrow ({}^4\text{He}\eta)_{\text{bound}} \rightarrow {}^3\text{He}n\pi^0$ process was for the first time obtained experimentally. The result obtained for the $dd \rightarrow ({}^4\text{He}\eta)_{\text{bound}} \rightarrow {}^3\text{He}p\pi^-$ reaction is about four times lower in

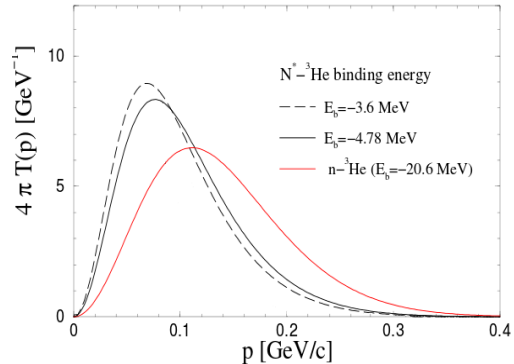


Fig. 2: Momentum distribution of N^* (black solid and dashed) and neutron (red solid) inside ${}^4\text{He}$ nucleus calculated for $N^*{}^3\text{He}$ potential for binding energy -3.6 MeV and -4.78 MeV [5, 6] and $n{}^3\text{He}$ potential with 20.6 MeV binding energy, respectively.

comparison with the result obtained from 2008 data [7]. The achieved sensitivity of about 6 nb is close to the theoretical prediction resulting in $\sigma_{\text{tot}} \simeq 4.5$ nb [8] which is based on an approximate calculation of the scattering amplitude for the two body process. We may conclude that the data collected with the WASA-at-COSY detector in 2010 do not show a signal for a narrow ${}^4\text{He}\eta$ mesic nucleus [1]. However, the theoretical interpretation with respect to very wide $({}^4\text{He}\eta)_{\text{bound}}$ or ${}^3\text{He}\text{-}N^*$ bound system is in progress [5, 6].

We acknowledge support by the Foundation for Polish Science - MPD program, by the Polish National Science Center through grants No. 2011/01/B/ST2/00431, DEC-2013/11/N/ST2/04152 and by the FFE grants of the Forschungszentrum Jülich.

References:

- [1] P. Adlarson *et al.*, *Nucl. Phys. A*, submitted (2017).
- [2] M. Skurzok, W. Krzemień, O. Rundel and P. Moskal, *Acta Phys. Polon.* **B47**, 503 (2016).
- [3] M. Skurzok, *PhD Thesis, Jagiellonian University*, *arXiv:nucl-ex/1509.01385* (2015).
- [4] M. Skurzok, W. Krzemień, P. Moskal, *Acta Phys. Polon.* **B46**, 133 (2015).
- [5] N. G. Kelkar, *Eur. Phys. J.* **A52**, 309 (2016).
- [6] N. G. Kelkar, D. Bedoya Ferro, P. Moskal, *Acta Phys. Polon.* **47**, 299 (2016).
- [7] P. Adlarson *et al.*, *Phys. Rev.* **C87**, 035204 (2013).
- [8] S. Wycech, W. Krzemień, *Acta Phys. Polon.* **B45**, 745 (2014).

^a M. Smoluchowski Institute of Physics, Jagiellonian University, 30-059 Cracow, Poland

^b National Centre for Nuclear Research, 05-400 Otwock-Świerk, Poland,

Search for the box anomaly via $\eta' \rightarrow \gamma\pi^+\pi^-$ with CLAS

Xinying Song

Introduction The effective Wess-Zumino-Witten Lagrangian is constructed as a close form expression in 5 dimensions to account for chiral effective lagrangian due to the parity violation. It summarizes and determines the effects of anomalies in current algebra [1, 2], and consists of two parts as shown in Eq. 1 and Eq. 2 [3]. Part A describes the $\pi^0 \rightarrow \gamma\gamma$, which is defined as triangle anomaly term shown in Fig. 1, while the part B describes the vertex coupling of the photon to three pseudo-scalar meson, which is noted as box anomaly as shown in Fig. 2.

$$A = \frac{ne^2}{96\pi^2 f_\pi^2} \pi^0 \epsilon^{\mu\nu\alpha\beta} F_{\mu\nu} F_{\alpha\beta}, \quad (1)$$

$$B = -\frac{1}{12} \frac{n}{\pi^2 f_\pi^3} \epsilon^{\mu\nu\alpha\beta} A_\mu \partial_\nu \pi^+ \partial_\alpha \pi^- \partial_\beta \pi^0. \quad (2)$$

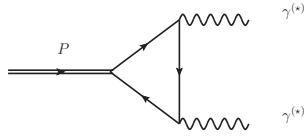


Fig. 1: triangle anomaly

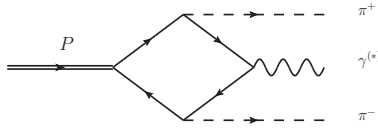


Fig. 2: box anomaly

Besides, the η/η' decays offer a good probe of charge parity violation (CPV) in the flavor conserving sector, which is different from that seen in flavor-changing B-meson decays. It can yield complementary information on the s-strangeness conserving CPV which can only be indirectly gleaned from neutron electric dipole moment study [4]. With the the world's largest statistic of η' taken in 2008 of g12 run in CLAS at Jefferson Lab [5], we could measure the $\text{Br}(\eta' \rightarrow \gamma\pi^+\pi^-)$ and the contribution of box anomaly via $\eta' \rightarrow \gamma\pi^+\pi^-$.

Signal extraction After applying the energy loss and momentum correction on every event, to select the signal events and suppress the background, we select events with the selection criteria on vertex, the difference between the measured and calculated time for $\pi^{+/-}$, the true timing difference of charged particles in the final state and the fiducial geometry of the detectors. After performed the kinematic fitting, the confidence level of the χ^2 probability density function is required greater than 1%. However, after applied the event selection criteria above, the mainly background of $\gamma p \rightarrow p\rho^0$ with $\rho^0 \rightarrow \pi^+\pi^-$ survived much. The possible solution is to extract the signal yields of η' via fitting for η' yields in each bin of invariant mass of $\pi^+\pi^-$, as shown in Figure. 3. The statistic reaches up to 0.5 million.

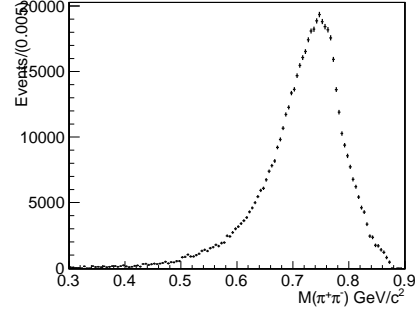


Fig. 3: Invariant mass spectrum of $\pi^+\pi^-$

Correction on the line shape of $M(\pi^+\pi^-)$ The contribution from the box anomaly is small and comparably flat on mass spectrum of $\pi^+\pi^-$, henceforth, we must consider the distortion on the line shape of $M(\pi^+\pi^-)$ from the acceptance and resolution as functions of $M(\pi^+\pi^-)$, though they may have a small impact. To extract the acceptance curve and resolution curve, we generate signal MC samples on every mass point of $M(\pi^+\pi^-)$ with 0 width. Considering the migration of the mass point, a tuning on the MC sample by the proportion of each mass point in real ρ^0 shape [6, 7, 8] is done. Finally, the mass shift and acceptance curve is given as shown in Figure 4. The resolution of MC samples of each mass point on $M(\pi^+\pi^-)$ is shown in Figure 5.

Models to be used We also show the projections on $M(\pi^+\pi^-)$ of the models which will be used in the spectrum fitting. They are including ρ^0 shape [6, 7, 8] with ρ^0 - ω mixing effect with or without considering box anomaly and model-independent approach with interference with ω , as shown in Figure 6.

The service work in CLAS The service work in CLAS includes: The recooking work of the g12 data in CLAS experiment for the missing data on the JLab farm tape silo. The tape silo was down before so part of reconstructed data of g12 run was lost. What I have done are: cached, skimmed and reconstructed the raw data and wrote them into the tape silo, confirmed of the missing files which have been back after updating the the computing system, re-skimmed the remaining files of g12 after confirming all the missing files are back. These data which was missing before takes about one quarter of the whole data of g12 in the first two directories, and they could be used in the physics analysis such as the searching for CPV in $\eta' \rightarrow \pi^+\pi^-e^+e^-$, $\eta'\gamma e^+e^-$.

Summary To extract the contribution from box anomaly, a measurement with high precision is required. In this text, the mass shift and distortion on the line shape of $M(\pi^+\pi^-)$ during the reconstruction are discussed. Besides, according

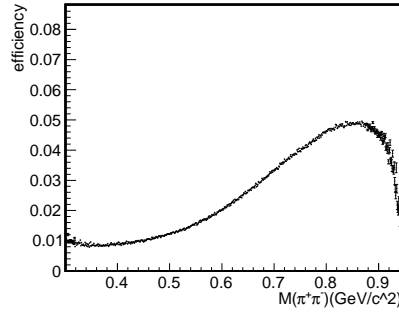


Fig. 4: The mass shift and acceptance curve.

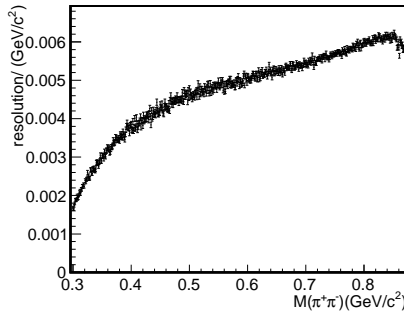


Fig. 5: (The resolution of MC samples of each mass point on $M(\pi^+\pi^-)$).

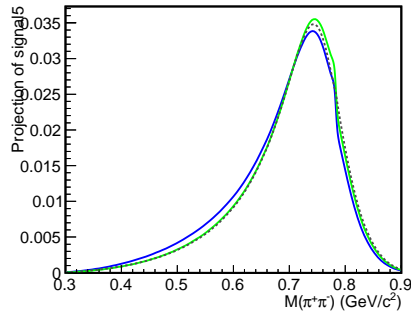


Fig. 6: The blue solid line represents the models [6, 7, 8] with $\rho - \omega$ mixing effect; the green solid green line represents models [6, 7, 8] with $\rho - \omega$ mixing effect plus the contribution from box anomaly; the dotted black line represents line shape of the model-independent approach [9] with interference with $\omega \rightarrow \pi^+\pi^-$.

to the $\rho - \omega$ mixing effect observed on the line shape, we introduce several models which could be used to describe the distribution.

References:

- [1] J. Wess and B. Zumino, Phys. Lett. B **37**, 95 (1971).
- [2] E. Witten, Nucl. Phys. B **223**, 422 (1983).
- [3] Thimo Petri, Anomalous decays of pseudoscalar mesons, arXiv:1010.2378.
- [4] C.Q. Geng, J.N. Ng and T.H. Wu, Mod. Phys. Lett. A **17**, 1489-1498 (2002)
- [5] https://www.jlab.org/Hall-B/physics/experiments/run_period.html.
- [6] G.J. Gounaris, J.J. Sakurai, Phys. Rev. Lett **21**, 244 (1968).
- [7] R. R. Akhmetshin et al., Phys. Lett. B **527**, 161 (2002).
- [8] B. Aubert et al., Phys. Rev. D **86**, 032013 (2012).
- [9] F. Stollenwerk et al., Phys. Lett. B **707** 184C190 (2012).

Search for light dark bosons in η meson decays

M.Berlowski, D.Pszczel, J.Stepaniak

Search for weakly interacting light particles related to Dark Matter was performed with WASA detector at COSY in η decays with dielectron pair(s). According to some extension of the Standard Model (SM) a hypothetical new light boson that couples to dileptons can be responsible for an increase in the branching fraction of $\eta \rightarrow e^+e^-$ and $\eta \rightarrow \pi^0 e^+e^-$ decays. In such decays, the background from SM diagrams is negligible. In more frequent Dalitz decay into lepton pair and a photon the new vector U boson could manifest itself as an enhancement in the distribution of e^+e^- pair invariant mass. It would be a carrier of a new type of weak interaction responsible for dark matter annihilation into lepton pair therefore it turns out to be an important element for the Light Dark Matter scenario. The vector boson cannot be produced in $\eta \rightarrow \pi^0 e^+e^-$ decay in a tree-level and this decay channel appears to be adequate for the search of the scalar/pseudoscalar object.

The η mesons were produced in $pp \rightarrow pp\eta$ reaction at 1.4 GeV incident proton kinetic energy. About 50×10^6 and 90×10^6 η meson were produced in two experiments performed in 2008 and 2012 during about two and seven weeks of data taking respectively. The event candidates were chosen to fulfill proper topology condition and particle identification criteria. Events from gamma conversion in the beam tube were rejected. Final separation of signal candidates was based on kinematics criteria. Fig. 1 shows the reconstructed e^+e^- invariant mass distribution from $\eta \rightarrow e^+e^-\gamma$ decay for the 2012 data sample. The shape of the distribution is well described by simulation of expected signal with small background admixture. We don't observe any significant maximum from a hypothetical U boson decay. The search for unseen up to now $\eta \rightarrow \pi^0 e^+e^-$ decay was performed at two selection level. The fit to the MMpp distribution (Fig. 2a) after the first selection step clearly indicates the contribution of η decays. After the final selection a fit to the sum of expected η signal and background from the most prominent $\pi^0\pi^0$ direct production is consistent with possible admixture of only a couple of $\eta \rightarrow \pi^0 e^+e^-$ events. It allows us to establish a preliminary upper limit for BR of about 3×10^{-5} . More stringent limit can be obtained for large masses of e^+e^- pair ($M_{ee} > 100 MeV/c^2$), where 4 events are observed in 2012 data set and 2 events in 2008 data. In the final selection of $\eta \rightarrow e^+e^-$ event candidates we don't observe any enhancement around the η mass in MMpp distribution (see Fig. 3). The preliminary limit for $\eta \rightarrow e^+e^-$ BR of about 6×10^{-6} is extracted.

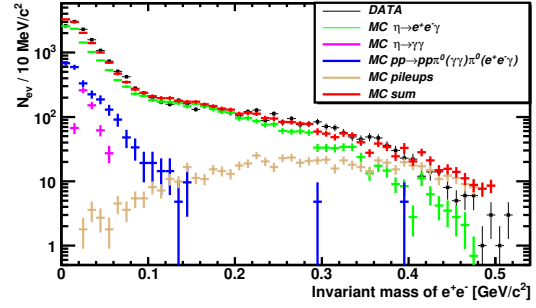


Fig. 1: Invariant mass of e^+e^- in the $\eta \rightarrow e^+e^-\gamma$ decays.

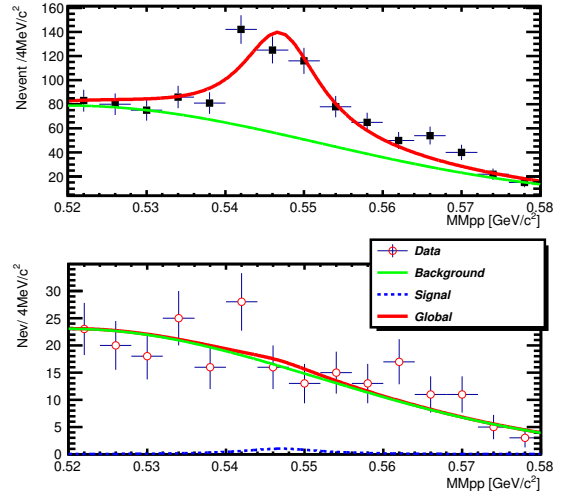


Fig. 2: Distribution of pp missing mass for $\eta \rightarrow \pi^0 e^+e^-$ candidates from 2012 run. The best fits to the sum of the signal and background are shown for first (a) and second (b) selection step.

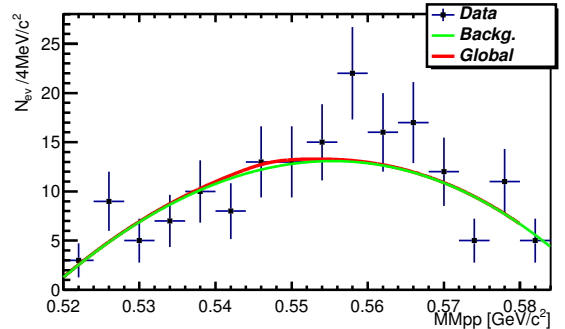


Fig. 3: Distribution of pp missing mass for $\eta \rightarrow e^+e^-$ candidates in 2012 data set .

Executive Summary of Theoretical Developments in Electron Cooling and Stochastic Cooling

H. Stockhorst and T. Katayama, Nihon University, Japan

The cooler synchrotron COSY is the world's only machine that is equipped with a low energy electron cooler (100 keV) as well as a high energy cooler with 2 MeV. In addition the machine offers stochastic cooling in the high energy range. COSY is therefore virtually predestinated to investigate the interaction of high energy electron and stochastic cooling as well as for research topics related to open theoretical and experimental questions specifically in the domain of high energy electron cooling. Research results are of major importance in future accelerator projects for precision experiments in particle physics.

Electron Cooling

The binary collision model of an ion with electrons to describe electron cooling was developed mostly by BINP (Budker Institute of Nuclear Physics, Novosibirsk, Russia) group since ~ 1970. It was based on the plasma physics theory rapidly evolved in 1950 ~ 1960 for the nuclear fusion project. The features of this binary collision model are 1) the flattened electron velocity distribution and 2) the adiabatic collision model for the magnetized electrons. Results of those theories give us the basic understanding of friction and diffusion forces while the Coulomb logarithm terms in the theory seem to be complicated and have some ambiguity. It could be concluded that the present status of the electron cooling theory is far from the level of a complete description of the physical cooling process. It could be compared with the stochastic cooling theory where the reliable friction and diffusion forces of the cooling process are obtained for the coasting or bunched beams.

In these circumstances, the empirical formulae given by V. Parkhomchuk (2000) are quite simple, being convenient to be used in the simulation work of which the results sometimes reproduce the experimental ones quite well. However in this formulae the longitudinal and transverse cooling forces are represented to be identical which seems to be much different from the results of binary collision model and the experimental results found e.g. at COSY with its new high energy electron cooler. In addition, as a matter of fact, this is lacking the theoretical background as an *empirical formulae*, even sometimes it gives the nice agreement with the experimental ones.

A new approach of describing the cooling process, the evolution of transverse and longitudinal ion velocity distribution, is necessary, for example to solve the 2D Fokker-Planck equation with use of universal Friction (F) and Diffusion (D) forces. An ambitious project is started to obtain the universal F and D terms. In a first step a report [1] has been prepared where the electron cooling theory, including the new approach of Coulomb logarithm problem is reviewed. However the construction of a complete theory of electron cooling is not yet finished. Especially in the case of magnetized cooling, the process is not well analyzed and needs more theoretical studies as well as experimental investigations with the high energy cooler at COSY.

To check the validity of Parkhomchuk empirical formulae, we have compared the experimental cooling results at

COSY with the simulations deduced from the Parkhomchuk empirical formulae. The agreement is found to be rather well for the COSY low energy electron cooler. Presently the development of the Fokker-Planck code for the simultaneous solution of longitudinal and transverse velocity distribution functions is continued.

Stochastic Cooling

As compared to the electron cooling the theory of stochastic cooling is quite well understood. In a recent publication [2] a comprehensive description of the stochastic cooling process based on the mathematical theory of signal processing was presented. This allows including a practical or theoretical engineering design of pickup and kicker structures in the cooling model. Measured or theoretical transfer functions of microwave amplifiers and filters are included as well. Knowing the cooling system parameters the evolution of momentum cooling is then described by a Fokker-Planck equation. The solution gives the time evolution of the particle's momentum distribution. From the point of view of signal processing the stochastic cooling system forms a feedback loop via the beam. Consequently, depending on the adjustment of the system parameters and the machine optics lattice the loop can be stable or unstable resulting in cooling or heating. The theory therefore allows to analyze the open loop gain. The results can be directly compared with open loop measurements and give important information on the loop stability margin of the systems' closed loop gain.

Transverse cooling is described by a rate equation for the transverse beam emittance which similarly to momentum cooling includes the engineering design of the transverse feedback loop.

The cooling theory includes the beam-target interaction induced by an internal target. Intra-beam scattering being important at low particle velocities and high beam intensities is taken into account.

In a series of cooling experiments at COSY including the beam-target interaction the validity of stochastic cooling model has been successfully verified. The model has been applied to design the stochastic cooling system of the HESR for ion and anti-proton beam cooling as well as for beam cooling during the anti-proton accumulation assisted by moving barrier bucket operation [3]. The proposed accumulation scheme was successfully tested in a proof-of-principle experiment at the GSI, Darmstadt [4].

References:

- [1] T. Katayama, Internal Report, November 2016
- [2] H. Stockhorst, T. Katayama and R. Maier, "Beam Cooling at COSY and HESR", Key Technologies, Volume 120, Forschungszentrum Jülich, ISBN 978-3-95806-127-9
https://juser.fz-juelich.de/record/807739/files/Schlusseltech_120.pdf
- [3] T. Katayama et al., IPAC10, Kyoto, Japan, May 23-28, 2010
- [4] M. Steck et al., COOL11, Alushta, Ukraine, Sept. 12-16, 2011

FairMQ for the \bar{P} ANDA Experiment

T. Stockmanns,
Forschungszentrum Jülich

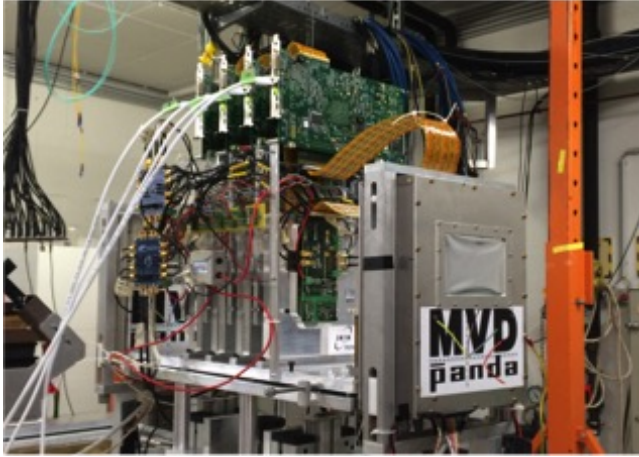


Fig. 1: Picture of the test beam setup at the COSY accelerator in Jülich

1 Introduction

Once \bar{P} ANDA is running with its design luminosity of $2 \cdot 10^{32} \text{ cm}^{-2} \text{ s}^{-1}$ it will produce about 200 GByte/s of raw data. Due to the very similar signatures of signal and background events all sub-detectors continuously transmit their data to the online computing system without a hardware trigger. Each detector hit contains a time stamp which is the basis to combine the free running data into events. This data stream is then processed in an event selector which has to reduce the data by a factor of 1000 for permanent storage by selecting only those events which look physically interesting. After data selection \bar{P} ANDA will produce a total of about 1 PByte/year experimental data and in addition 2 PByte/year simulation data.

To find the signal events in the large background is the challenge of the event selection and requires that most, if not all, of the data produced by the experiment is processed online with the same average rate with which the data are measured. To achieve the necessary computing power in an efficient way different hardware types from FPGAs, GPUs to multicore CPUs and mixtures of these systems are under study. To exploit parallel hardware different technologies are available. One very convenient approach for multicore systems are message queues. They allow to pack the algorithms in small independent processes which are running in parallel and handle the inter-process communication via the message queues. Their application is tested on the example of test beam data for the \bar{P} ANDA experiment.

2 The Test Beam Setup

As a first test of FairMQ with real detector data a test beam of the MVD at the COSY accelerator in Jülich was chosen. Fig. 1 shows the setup. The first and the last detector layers both consisted of conventional silicon strip detectors for

alignment purposes and was not part of this test. In between the two strip planes were four silicon pixel detectors with a continuous running front-end electronics ToPix v4 ASIC¹. Each of the pixel detectors was read out via an attached FPGA board (XILINX ML605) which pushed the data via an UDP connection to two data taking PCs where the raw data for each ASIC was stored in an individual file. A 2.8 GeV/c proton beam was directed through the setup perpendicular to the detector planes.

3 Processing of Test Beam Data

The processing of the test beam data is subdivided into small individual executable programs which are connected via different types of FairMQ connections. The input to the processing stage is either the raw data of the beam time stored in binary files or directly the test beam data during the beam time. The output are fully processed tracks based on the data measured with the four pixel detectors.

Fig. 2 shows an overview of the different processing components in the coloured boxes and their connection via message queues. The raw data is processed individually on 4 different PCs before it is merged in an *Event Builder* which combines the individual data streams by their time stamps into single events. After that the *Track Finder and Fitter* searches for straight line tracks in the data of the four front-end ASICs in each event.

4 Performance

The performance in a distributed system was tested with 4+1 PCs. The first four Linux PCs were each processing the data of one ASIC. One of them also did the event building and track finding/-fitting. These four PCs were connected via Gbit ethernet. The fifth MAC PC was used to run the online monitoring and the global controller to start the processing. This one was connected with the other PCs via a 100 Mbit ethernet connection.

The processed data corresponded to one beam spill with a length of 20 seconds. Each ASIC collected about 55 MByte of data during this time. The subdivision of the processing into single executables allowed to use all 8 cores of the Linux machines for 100 % during the run time. The individual processing stages for each ASIC took 15 seconds for full processing which is below the 20 seconds it took to create the data, which was the requirement. The processing time nevertheless increased to one minute once the event building with all four ASICs was included. The later track finding and fitting did not have any influence on the processing time.

The reason for the strong increase of the processing time is still under study.

¹Application Specific Integrated Circuit

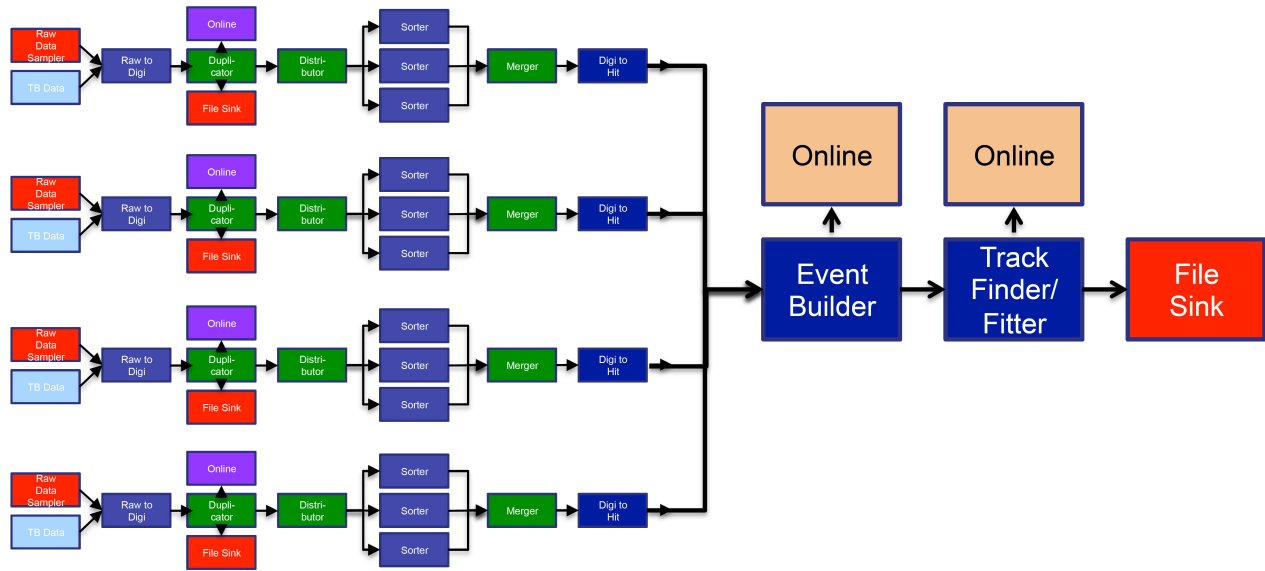


Fig. 2: Flow chart of the processing stages for the complete setup

5 Summary

A first test of FairMQ was made for the \bar{P} ANDA experiment. A very simple setup with just four pixel detectors was chosen with the requirement to process the data with the same speed it was produced. In total 50 processes are dealing with the data running on four different PCs with an additional control PC. The change from the standard implementation in PandaRoot towards a system based on FairMQ proved to be easy and reliable. With this setup it is possible to process the test beam data up to fully reconstructed tracks. The achieved performance for the individual processing stages of the four detectors was faster than the data production in the test beam. However, the performance dropped significantly when the data from all four detectors was combined into a common event structured data stream, which is subject to further development.

Comparison of the theoretical higher order Rogowski coil beam position model with a simulation

F. Trinkel^{a,b} and H. Soltner^c for the JEDI collaboration

For the planned measurement of Electric Dipole Moments (EDMs) of charged hadrons, like the proton or deuteron, a new RF-Wien Filter will be installed at the COoler SYNchrotron (COSY). To control the beam position to the magnetic and electric center of the Wien Filter two new Beam Position Monitors (BPMs), using so called Rogowski coils, will be installed downstream and upstream of the Wien Filter [1]. These BPMs measure the magnetic field induced by the particle beam flux. The beam position is calculated out of this measured magnetic field, which induces a voltage in each segment of the segmented coil. A theoretical Rogowski coil beam position model is compared with simulations to improve the possibility of a better beam position measurement.

Each BPM consists of a torus which is wound by one layer of a 150 μm copper wire. The radius of the torus is $R = 40\text{mm}$. The radius of the tube amounts to $a = 5\text{mm}$. The winding is divided in four segments. Each covers an azimuth angle range of 90° , starting at 0° . The number of windings for each segment is 255. A sketch of such a Rogowski coil is shown in Fig. 1.

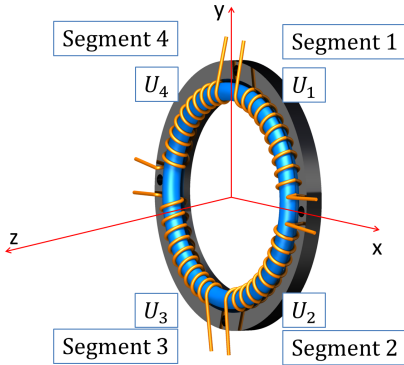


Fig. 1: Sketch of a Rogowski Coil, which detects the horizontal and vertical beam position. The radius of the torus is $R = 40\text{mm}$ and the radius of the tube amounts to $a = 5\text{mm}$.

For a more precise beam position determination an accurate model is necessary. The improvement of the Rogowski coil BPM model is presented in the following. In equation 1 the magnetic field is shown in dependency of the beam position. The coordinates are expressed in cylindrical coordinates r_0 and φ_0 . I_0 represents the pencil like beam current and μ_0 is the vacuum permeability. The observer position is described by r and φ .

$$B_\varphi = \frac{\mu_0 I_0}{2\pi r} \frac{1 - \frac{r_0}{r} \cos(\varphi - \varphi_0)}{1 + \left(\frac{r_0}{r}\right)^2 - 2\frac{r_0}{r} \cos(\varphi - \varphi_0)} \quad (1)$$

$:= A$ with $u = \frac{r_0}{r}$ and $\Delta\varphi = \varphi - \varphi_0$.

The definition of A is shown in equation 2, where $u = \frac{r_0}{r}$ and $\Delta\varphi = \varphi - \varphi_0$.

$$A(u, \Delta\varphi) = \frac{1 - u \cos(\Delta\varphi)}{1 + u^2 - 2u \cos(\Delta\varphi)} \quad (2)$$

The next step is a Taylor series for $A(u, \Delta\varphi)$ with $u = \frac{r_0}{R} \ll 1$ up to the fifth order is calculated.

$$B_\varphi = \frac{\mu_0 I_0}{2\pi r} \left[\frac{dA}{du^0} \Big|_{u=0} + \frac{dA}{du^1} \Big|_{u=0} \left(\frac{r_0}{r}\right) + \frac{1}{2} \left(\frac{r_0}{r}\right)^2 \frac{d^2 A}{du^2} \Big|_{u=0} + \frac{1}{6} \left(\frac{r_0}{r}\right)^3 \frac{d^3 A}{du^3} \Big|_{u=0} + \frac{1}{24} \left(\frac{r_0}{r}\right)^4 \frac{d^4 A}{du^4} \Big|_{u=0} + \frac{1}{120} \left(\frac{r_0}{r}\right)^5 \frac{d^5 A}{du^5} \Big|_{u=0} + O\left(\left(\frac{r_0}{r}\right)^6\right) \right]$$

With this magnetic field the induced voltage for the Rogowski coil BPM can be calculated by solving the integrals presented in equation 3. The integral limits φ_1 and φ_2 defines the angular range. $-a$ and a with $R - \sqrt{a^2 - z^2}$ and $R + \sqrt{a^2 - z^2}$ denote the area of the induced magnetic flux. The parameter N describes the number of windings, which are in the area of the integral limits.

$$U_{\text{ind}} = -N \frac{d\Phi}{dt} = -N \frac{d}{dt} \frac{\int_{\varphi_1}^{\varphi_2} \int_{-a}^a \int_{R-\sqrt{a^2-z^2}}^{R+\sqrt{a^2-z^2}} B(r, \varphi) r dr dz R d\varphi}{\int_{\varphi_1}^{\varphi_2} R d\varphi} \quad (3)$$

The solution of equation 3 is presented in the following lines. $\Delta\Psi$ is the angular range, which each segment covers. For a Rogowski coil BPM, which is parted into four segments, $\Delta\Psi$ covers $\pi/2$. a and R are Rogowski coil parameter, which are the radii of the torus and the coil itself.

$$U_{\text{ind}} = \frac{N\mu_0}{2\Delta\Psi} \frac{dI_0}{dt} \left[2(\Delta\Psi) \left(R - \sqrt{R^2 - a^2} \right) + 2r_0 \left[\sin(\Psi - \varphi_0 + \Delta\Psi) - \sin(\Psi - \varphi_0) \right] \frac{R - \sqrt{R^2 - a^2}}{\sqrt{R^2 - a^2}} + \frac{r_0^2}{2} \left[\sin(2(\Psi - \varphi_0 + \Delta\Psi)) - \sin(2(\Psi - \varphi_0)) \right] \frac{a^2}{(R^2 - a^2)^{3/2}} + \frac{r_0^3}{3} \left[\sin(3(\Psi - \varphi_0 + \Delta\Psi)) - \sin(3(\Psi - \varphi_0)) \right] \frac{a^2 R}{(R^2 - a^2)^{5/2}} + \frac{r_0^4}{4} \left[\sin(4(\Psi - \varphi_0 + \Delta\Psi)) - \sin(4(\Psi - \varphi_0)) \right] \frac{a(a^2 + 4R^2)}{(R^2 - a^2)^{7/2}} + \frac{r_0^5}{5} \left[\sin(5(\Psi - \varphi_0 + \Delta\Psi)) - \sin(5(\Psi - \varphi_0)) \right] \frac{a^2 R(3a^2 + 4R^2)}{4(R^2 - a^2)^{9/2}} \right]$$

For each segment with the corresponding starting angle Ψ and $\Delta\Psi = \pi/2$ the induce voltage is calculated. With the identities in equation 4 the induced voltage is presented in dependency of the beam position x_0 and y_0 .

$$\begin{aligned} x_0 &= r_0 \cos(\varphi_0) \\ y_0 &= r_0 \sin(\varphi_0) \end{aligned} \quad (4)$$

To compare the simulation with the theoretical prediction a horizontal and vertical voltage ratio is calculated. These ratios are presented in equation 5. The arrangement of the voltage is shown in figure 1.

$$\begin{aligned} \frac{\Delta U_x}{\Sigma U} &= \frac{(U_1 + U_2) - (U_3 + U_4)}{U_1 + U_2 + U_3 + U_4} \\ \frac{\Delta U_y}{\Sigma U} &= \frac{(U_1 + U_4) - (U_2 + U_3)}{U_1 + U_2 + U_3 + U_4} \end{aligned} \quad (5)$$

The ratio calculated by the induced voltages in horizontal and vertical plane is shown in equation 6 and 7. With the help of these equation it is possible to calculate the ratio in horizontal and vertical plane with the Rogowski coil parameters (a and R) and the beam position (x_0 and y_0).

$$\begin{aligned} \frac{\Delta U_x}{\Sigma U} &= \frac{x_0}{\pi\sqrt{R^2 - a^2}} \\ &+ \frac{a^2 x_0 y_0}{2\pi(R^2 - a^2)^{3/2}(R - \sqrt{R^2 - a^2})} \\ &- \frac{a^2 R (x_0^3 - 3y_0^2 x_0)}{6\pi(R^2 - a^2)^{5/2}(R - \sqrt{R^2 - a^2})} \\ &+ \frac{a^2 R (4R^2 + 3a^2) (x_0^5 - 10y_0^2 x_0^3 + 5y_0^4 x_0)}{40\pi(R^2 - a^2)^{9/2}(R - \sqrt{R^2 - a^2})} \end{aligned} \quad (6)$$

$$\begin{aligned} \frac{\Delta U_y}{\Sigma U} &= \frac{y_0}{\pi\sqrt{R^2 - a^2}} \\ &+ \frac{a^2 x_0 y_0}{2\pi(R^2 - a^2)^{3/2}(R - \sqrt{R^2 - a^2})} \\ &- \frac{a^2 R (y_0^3 - 3x_0 y_0^2)}{6\pi(R^2 - a^2)^{5/2}(R - \sqrt{R^2 - a^2})} \\ &+ \frac{a^2 R (4R^2 + 3a^2) (y_0^5 - 10x_0^2 y_0^3 + 5x_0^4 y_0)}{40\pi(R^2 - a^2)^{9/2}(R - \sqrt{R^2 - a^2})} \end{aligned} \quad (7)$$

For the simulation a Rogowski coil with a radius R of 40 mm and a torus radius a of 5 mm is simulated. In the simulation the beam is moved to different positions and the induced fluxes of each segment of the coil is calculated and stored. The scheme of the applied beam position is presented in figure 2. Each red dot represents an applied beam position. The step-size is 0.5 mm. The magnetic fluxes are simulated for different positions in a range of 10 mm for the horizontal and vertical plane.

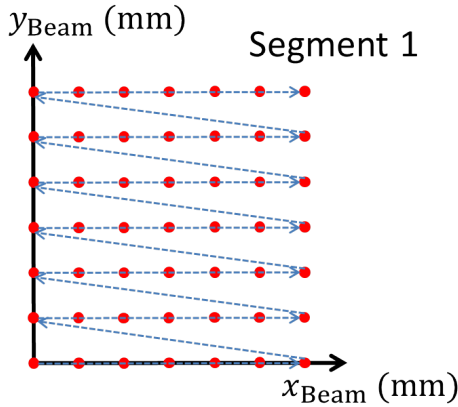


Fig. 2: Sketch of the applied simulated beam positions. Each red dot represent a simulated beam position. The step-size between each point is 0.5 mm. The magnetic fluxes are simulated for different positions in a range of 10 mm for the horizontal and vertical plane.

For the given beam positions the theoretical ratios in horizontal and vertical plane are calculated with the equations 6 and 7. Also the ratios of the simulated fluxes are calculated with the help of equation 5. Both ratios are compared

with each other. The comparison of simulation and theoretical prediction is presented in figure 3. The blue dots marks the ratio of the simulation and the red dots represent the ratio of the theoretical prediction. On the x-axis the ratio for the horizontal and on the y-axis for vertical plane is shown. The theoretical prediction is in a very good agreement with the simulated data. With such a precise model it is possible to improve the accuracy of a beam position determination for a real Rogowski coil BPM.

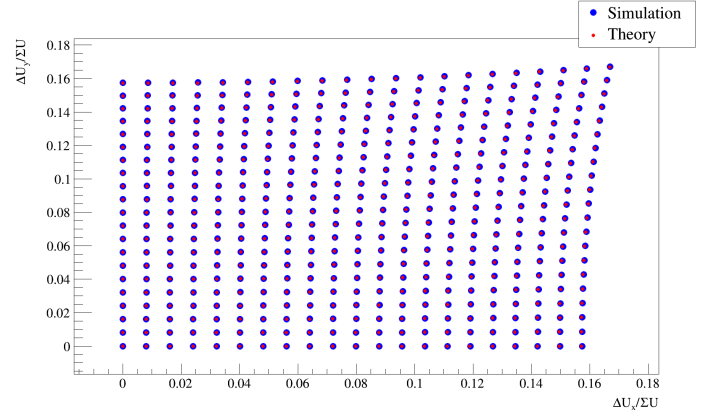


Fig. 3: Comparison of the simulated ratios and theoretical predicted ratios for the horizontal and vertical plane. The blue dots marks the ratio of the simulation and the red dot represents the ratio of the theoretical prediction. The theoretical prediction is in a very good agreement with the simulated data.

^a Institute for Nuclear Physics, FZ Jülich, Germany

^b Physics Institute III B, RWTH Aachen University, Germany

^c Zentralinstitut für Engineering, Elektronik und Analytik-1, FZ Jülich, Germany

References:

- [1] Slim, D. Heberling, Towards a High-Accuracy RF Wien Filter for Spin Manipulation at COSY Jülich, in: XVIth International Workshop in Polarized Sources, Targets, and Polarimetry, 2015, p. PoS(PSTP2015)033

Elastic $d^{12}C$ scattering within the Glauber approach

Yu. N. Uzikov¹ for the JEDI collaboration.

Due to intensive spin-orbit interaction in $d^{12}C$ system the vector analyzing power A_y of the process $d+^{12}C \rightarrow d+^{12}C$ is rather large at energies of the deuteron beam energy about $T_d = 200 - 300$ MeV [1]. For this reason the $d^{12}C$ elastic scattering will be used for polarimetry measurements in search for EDM of the deuteron in storage rings [2]. In theory the unpolarized differential cross section of this process measured at energy 270 MeV in Ref.[1] was studied only within the optical model with phenomenological complex interaction potential of the $d-^{12}C$ system. On the other hand, the spin observables of this process were studied within the DWBA approximation using as input elastic Nd -scattering amplitudes obtained by solving the Faddeev equations for three-nucleon problem [1]. A good agreement was obtained between this theory and data [1].

Another approach to this problem is to apply the Glauber theory of multistep diffraction scattering. The point is that the maximum values of the $A_y(\theta)$ and $d\sigma(\theta)/d\Omega$ in the $d^{12}C$ scattering are observed in the forward direction corresponding to the c.m.s. angles θ less than $40 - 50^\circ$. Furthermore, the deuteron beam energy 270 MeV corresponds to the proton beam with 135 MeV. As was shown recently [4], at this energy the unpolarized differential cross section and spin observables of the pd elastic scattering are well described by the Glauber theory with all spin-effects included [5]. Instead of the Nd elastic scattering, used in [1], the amplitudes of the $N^{12}C$ elastic scattering can be used as elementary on-shell amplitudes for $d^{12}C$ scattering. In this case the full amplitude of the $d^{12}C$ elastic scattering can be obtained from the general Glauber formalism of the pd scattering [5] as a particular case. In order to construct the $N^{12}C$ elastic scattering amplitudes one can use also the Glauber theory. However, at the first step we use here [3] a more simple model, that is the optical model of $N^{12}C$ scattering. In case of success this simple approach can be applied to extend the beam energy region and also to use other nuclei targets in dA scattering with the aim to find an optimal values of the figure of merit, i.e. $A_y^2 d\sigma/d\Omega$.

The results of our calculations of the differential cross section of the $d^{12}C$ scattering at 270 MeV in comparison with the data [1] in Fig.1. The contribution of single scattering (SS) mechanism and double scattering (DS) are shown separately. The Coulomb interaction is included into the SS amplitude. One can see from Fig. 1, that the SS mechanism alone is not sufficient to explain the absolute value of the cross section and only the coherent sum SS+DS allows us to get agreement with data in the forward hemisphere at scattering angles $< 25^\circ$. The $N^{12}C$ amplitude was taken from optical model using the code from [6]. This code allows to fit only the data on the unpolarized differential cross section of the $p^{12}C$ - scattering which were taken from [7] at 135 MeV. However, it was not possible to fit A_y for the $p^{12}C$ - scattering and, therefore, only qualitative agreement was obtained with the data on with A_y . As a result the results of our calculation for A_y in $d^{12}C$ scattering are only in qualitative agreement with the data [1] (see details in [3]). One may hope that more accurate fit the $p^{12}C$ data in respect of description of the

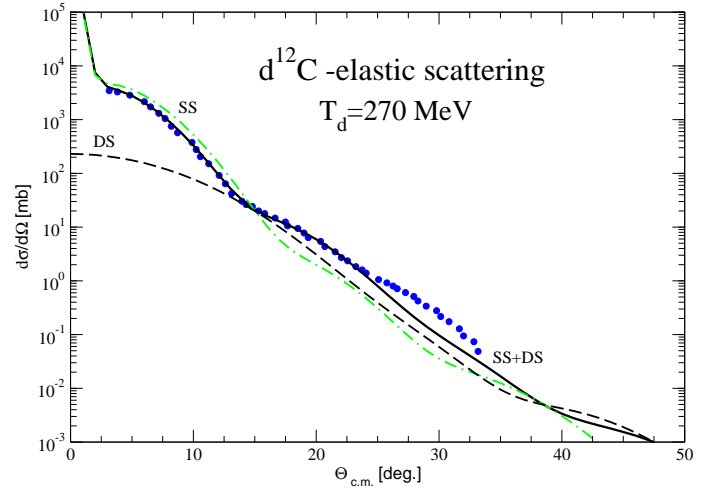


Fig. 1: The differential cross section of the elastic scattering of the deuteron off the carbon ^{12}C at the deuteron beam energy 270 MeV. The results of calculation performed within the Glauber model as described in the text, are shown for different mechanisms: SS (dashed-dotted line), DS (dashed), total SS+DS (full). The experimental data (points) are taken from Ref.[1].

A_y will provide a better agreement with the $d^{12}C$ data. For this aim one should use the spin-dependent Glauber model for $N^{12}C$ scattering.

References:

- [1] Y. Satou et al. Phys. Lett. B 549 (2002) 307.
- [2] N.P.M. Brantjes, V. Dzordhadze, R. Gebel et al. , Nucl. Inst. Meth. A 664 (2012) 49.
- [3] In Proc.: GGSWHP "Spin Physics, Symmetries and Applications", (29 August – 2 September, 2016, Tbilisi, Georgia); <http://collaborations.fz-juelich.de/ikp/cgswhp/cgswhp16/program/program.shtml>
- [4] A.A. Temerbayev, Yu.N. Uzikov, Yad. Fiz. 78 (2015) 38 [Phys. At. Nucl. 78 (2015) 35].
- [5] M.N. Platonova, V.I. Kukulin, Phys. Rev. C 81 (2010) 014004 [Phys. Rev. C 94 (2016) 069902(E)].
- [6] V. Karpov, A.S. Denikin, A.P. Alekseev et al., Yad. Fiz. 79 (2016) 520 [Phys. At. Nucl. 79 (2016) 749].
- [7] J.R. Comfort et al. Phys. Rev. C 21 (1980) 2162.

1 JINR, 141980 Dubna, Russia

Measurement of the spatial and energy loss resolution for the STT flash ADC readout for the PANDA experiment

S.Vejdani

PANDA, one of the pillars of the FAIR facility currently in construction in Darmstadt, is a next-generation particle detector that will study collisions of antiprotons with momenta from 1.5 to 15 GeV/c on a fixed proton or nuclear target. The Straw Tube Tracker (STT) is the main tracking detector for charged particles and part of the PANDA target spectrometer. The tasks of the STT are to determine the momenta of charged particles, via a precise spatial reconstruction of particle tracks in combination with a solenoid magnetic field, and to perform particle identification (PID) by a measurement of the specific energy loss (dE/dx). The PID information of the STT is necessary to separate protons, kaons and pions in the momentum region below 1 GeV/c. To achieve the high resolutions the development of the electronic readout system for the STT is required.

In April 2016, the first test was carried out in the COSY-TOF beam area. A proton beam with four different momenta (0.550 GeV/c, 0.750 GeV/c, 1.00 GeV/c and 2.95 GeV/c) was used. Figure 1 shows the straw tube prototype setup in the COSY - TOF beam area.

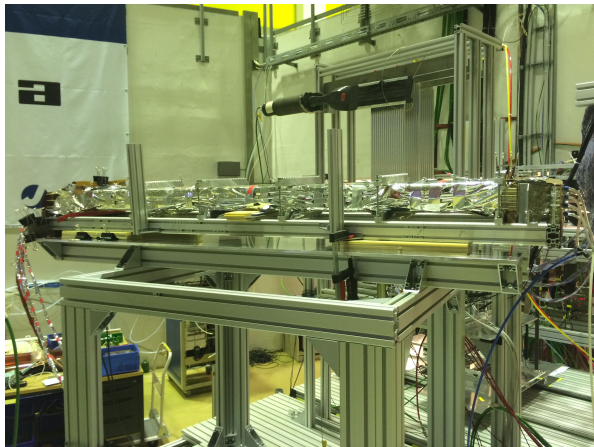


Fig. 1: The straw prototype setup in the COSY-TOF beam area.

In November 2016, the second test was carried out in the COSY-TOF beam area with a deuteron beam with three different momenta (0.60 GeV/c,

0.75 GeV/c and 1.5 GeV/c). In both tests, several data runs were taken for each momentum and for a wide range of operational settings such as high voltages and intensities.

The test setup consists of 128 PANDA tubes which are arranged in eight layers of 16 tubes. The electronic readout of the straw signals consists of front-end transresistance amplifiers with about 8 ns rise time and a gain factor of about 360, and Flash-Analog to Digital Converters (FADC) which sample the analog signal amplitude with a frequency of 240 MHz. FPGAs (Field Programmable Gate Array) controlling the readout of an FADC module are programmed for high flexibility.[1]

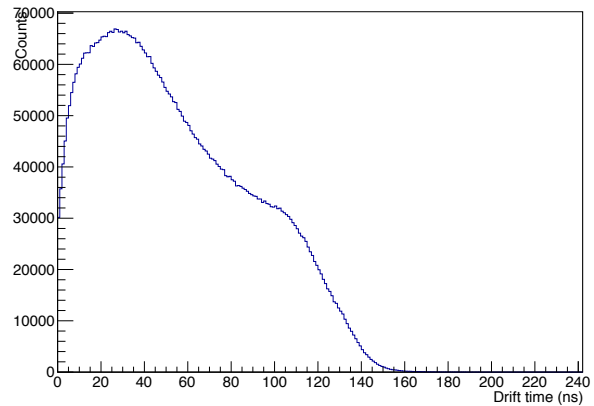


Fig. 2: Drift time spectrum of the selected straws for the 2.95 GeV/c proton beam.

The signals are sampled and recorded with the 240 MHz FADCs. The first step in the analysis method (Signal shape analysis) is done by base line determination, signal onset, pileup identification, rising edge slope calculation, zero crossing time, charge integration and tail cancellation. The next step in the analysis is the calibration, calculation of radius-drift time (calibration curve) and track reconstruction.

Figure 2 shows an example of the measured straw drift time after the calibration for the 2.95 GeV/c proton beam. After the track reconstruction, residuals calculated from the distance between the reconstructed track and the isochrons. Figure 3

shows the residual distribution for the 0.550 GeV/c proton beam. The spatial resolution obtained is of the order of 146 μm .

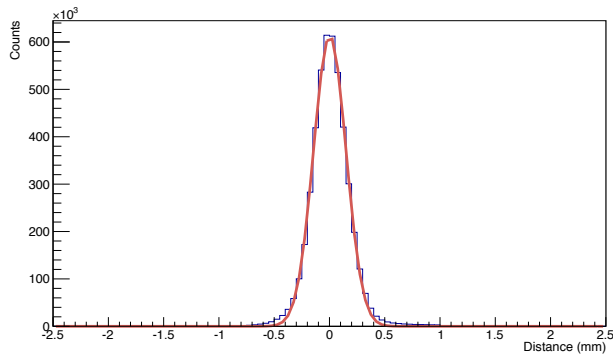


Fig.3 :The residual distribution for the 0.550 GeV/c proton beam. The spatial resolution obtained is of the order of 146 μm .

The amplified signals are fed into the FADCs with a sampling time interval of 4.17 ns (240MHz). An example of the recorded straw signals is shown in Figure 4.

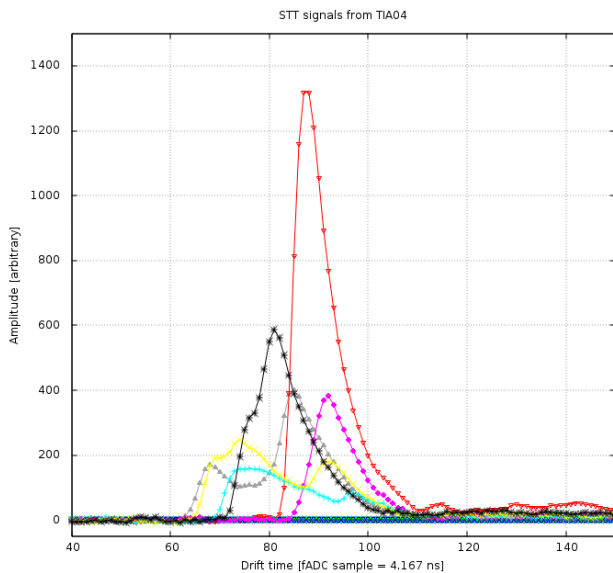


Fig. 4 : Analog signals from the straw tubes as recorded by the 240 MHz FADC.

For the energy loss measurement, the charge integration is done over the samples and it's normalized to the path length. As the next step cuts are applied on the largest energy losses per track, it's selective measurement of the energy losses with truncation mean method. An example

of the energy loss is shown in Figure 5. The best achieved energy resolution ($\sigma_{(dE/dx)}$) for the re-

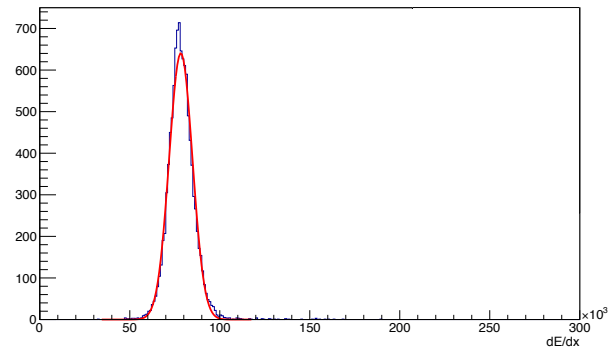


Fig.5 : The achieved energy resolution for the reconstructed tracks of 16 hits for the 0.550 GeV/c proton momentum.

constructed tracks of 16 hits for the 0.550 GeV/c proton momentum is 8.2% . Figure 6 shows the achieved energy resolution for three different

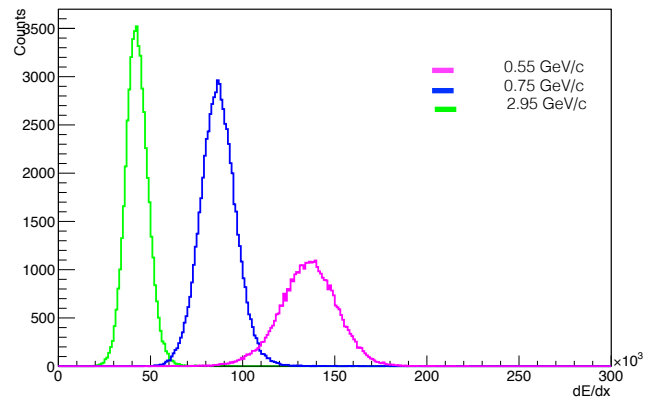


Fig.6 : The achieved energy resolution for the reconstructed tracks of 16 hits for three proton momenta (0.550 GeV/c, 0.750 GeV/c and 2.95 GeV/c)

proton momentum. The results of the spatial and energy resolutions look good and promising. The next step is to analyze the data taken with deuteron beam. There will be a good opportunity to compare the separation power of the STT prototype between deuterons and protons.

References:

[1] Technical Design Report for the PANDA Straw Tube Tracker, PANDA collaboration.

Simulation for the FToF detector in Panda experiment

D. Veretennikov

FToF detector for PANDA PID. Particle identification (PID) in the Forward Spectrometer in the PANDA experiment is realized with the help of the (Forward Time-of-Flight) FToF wall and forward RICH detectors. While the forward RICH provides effective hadron separation for momenta above 2 GeV/c for pions and above 4 GeV/c for protons, the FToF detector could provide hadron ID at particle momenta below 4 GeV/c.

The time-of-flights between the target and the scintillation wall for pions, kaons, protons and charged leptons are shown in Fig.1. The values of ToF ranges from 53.1 ns for proton momentum of 0.5 GeV to 25 ns for relativistic particles.

Besides the forward low momentum hadrons PID, the important function of the FToF wall is that it provides information on the event time stamp in a scintillation block. For a relativistic particle (for hadrons with momenta larger than 3-4 GeV/c) this information helps to reconstruct the event start time in the IP with a precision of a few ns. Provided the particle is identified either as a hadron or a charged lepton (muon or electron), this precision could be improved to some 100 ps which is the planned time resolution of the FToF detector.

The particle mass is reconstructed using the following equation:

$$m = p \sqrt{\frac{t^2}{t_c^2} - 1} \quad (1)$$

Here p is the particle momentum, $t_c = L/c$, L is the length of the particle track starting from the IP (start point), or from a decay vertex, to the hit position of a FToF counter, c is the speed of light, t is the measured time of flight, i.e., $t/t_c = 1/v$, where v is the particle velocity. The fractional uncertainty of the calculated mass can be estimated as

$$\frac{\delta m}{m} = \sqrt{\left(\frac{\delta p}{p}\right)^2 + \gamma^4 \left(\frac{\sigma_{ToF}}{t}\right)^2} \quad (2)$$

where $\gamma = 1/\sqrt{1-v^2}$. Due to the relativistic γ factor, the time-of-flight resolution of 50 (or 100) ps gives the main contribution to the mass smearing for the particles with momenta $p \geq 1$ GeV, while the momentum resolution of 1% has a much smaller effect. However, at $p < 1$ GeV the momentum uncertainty starts to dominate. An uncertainty of track reconstruction at the level of $\delta L/L \approx 0.001$ translates to $\delta\sigma_{ToF}$ of about 25 ps for relativistic particles.

The result of calculations for the hadron mass reconstruction (Eq.1) evaluated for the case of the maximal \bar{p} beam momentum (15 GeV) is presented in Fig.2. As can be seen the time-of-flight information obtained with the help of the FToF wall provides a reliable pion and kaon identification up to the secondary particle momentum of 2.5 GeV/c at $\sigma_{ToF} = 100$ ps proton (antiproton) identification up to 4 GeV/c for $\sigma_{ToF} = 100$ ps. Note that at momenta smaller than 0.5 GeV/c the proton time-of-flight increases very sharply with momentum decrease which results in deteriorates the mass reconstruction at very small momenta.

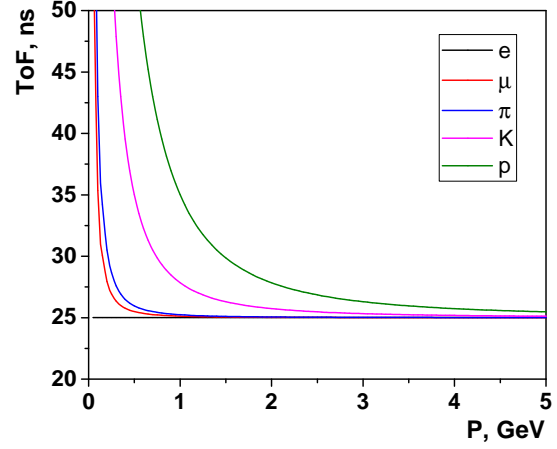


Fig. 1: Time-of-flight of hadrons, muons and electrons between the target and the FToF detector versus particle momentum

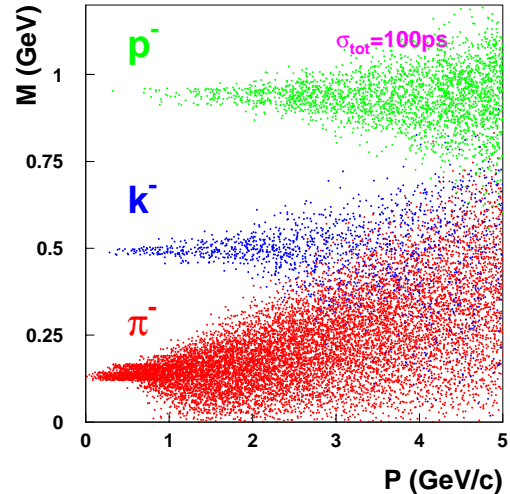


Fig. 2: Hadron masses reconstructed using the time-of-flight information with the ToF resolution of $\sigma = 100$ ps

Inclusive $\bar{\Lambda}$ production. One of the benchmark reaction shows efficiency of the FToF detector is inclusive $\bar{\Lambda}$ production. As seen from Table 1 the efficiency to detect both \bar{p} and π^+ from $\bar{\Lambda}$ decay in inclusive hyperon production ($\bar{p} + p \rightarrow \bar{\Lambda} + X, \bar{\Lambda} \rightarrow \bar{p} + \pi^+$) is about 20%.

Table 1: Generated and detected with FToF $\bar{\Lambda}$ and Λ events in inclusive $\Lambda, \bar{\Lambda}$ hyperon production with DPM generator

	Generated	Detected with FToF wall	Detection efficiency
$\bar{\Lambda}$	19874	3840	0.193
Λ	19518	100	0.005

Efficiency of the FToF detector for this benchmark reaction can be demonstrated as follow. All combinations of hadron pairs with opposite charges which were produced in a generated event and produced hits in the FToF detector were selected. The tracking system gives a 3-momentum of the hadron. Missing is the hadron mass. If the hadrons comes from $\bar{\Lambda}$ decay the negative hadron should have proton mass while positive hadron must be a pion. The time-of-flight is calculated for both hadrons in a selected pair using the hypothesis for hadrons masses, their momenta and track lengths. If the calculated time-of-flight is not in the windows of 100 ps from MC hit time ($|t_{ToF} - t_{MC}| < 100$ ps) and this combination is rejected. This is equivalent to the PID using the time-of-flight criterion in the real experiment. As shows in Fig.3 this criterion resulted in very strong suppression of the combinatorial background.

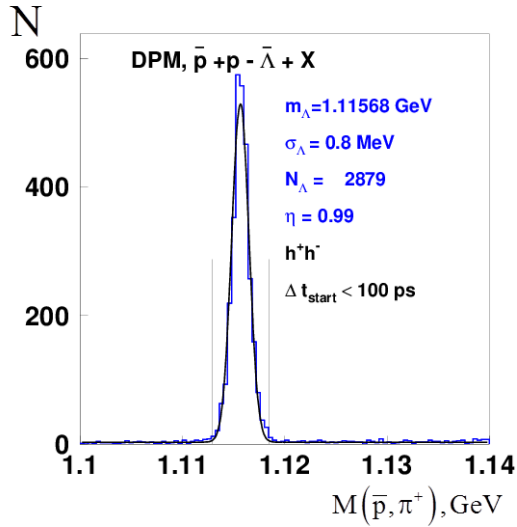


Fig. 3: Invariant mass distribution for $\bar{\Lambda}$

PID and T_0 determination. In the case when event start time T_0 is known (event base simulation) PID can be done using particles separation by their velocity $\beta = v/c$. For each track velocity can be calculated as

$$\beta = \frac{v}{c} = \frac{1}{c} \frac{L}{t_{ToF}} \quad (3)$$

where L is track length given by tracking system and t_{ToF}

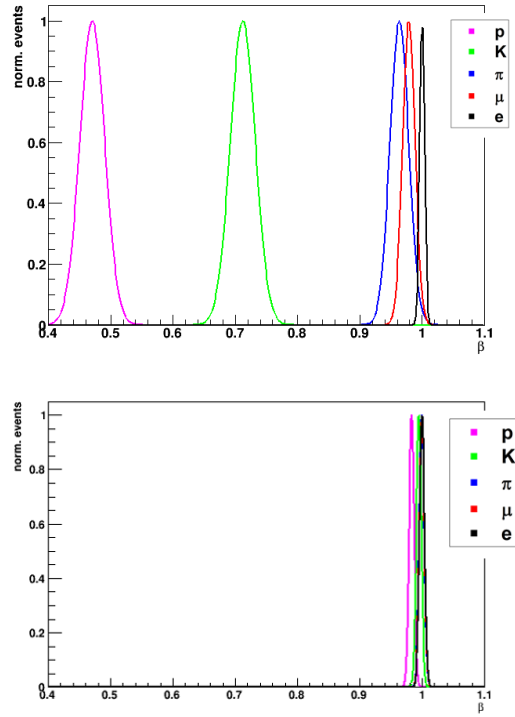


Fig. 4: Probability density functions for particles with momenta 0.5 GeV/c (upper panel) and 5 GeV/c (bottom panel)

is time-of-flight given by FToF detector. Then this velocity used to calculate probability for different particle species. Probability density functions (p.d.f.) for each particle is calculated using PANDAROOT MonteCarlo and showing on Fig.4. These p.d.f. are functions of momentum, given by tracking system and velocity, which is calculated using time-of-flight. In ideal case, when time-of-flight, track length and momentum resolutions are zero, all p.d.f. are just delta-function. In reality it is smeared and for particle with momentum above 5 GeV/c probability for each species are approximately same.

In case of unknown T_0 (time base simulation) PID and additionally event start time can be calculated using loop through all possible combination of particle for given number of hits. This procedure work only in case when number of hits are $n > 2$ or more. For N number of hits one can write system of N equations:

$$\begin{aligned} t_1^{ToF} &= T_0 + \frac{L_1}{c} \frac{\sqrt{p_1^2 + m_1^2}}{p_1} \\ t_2^{ToF} &= T_0 + \frac{L_2}{c} \frac{\sqrt{p_2^2 + m_2^2}}{p_2} \\ &\dots\dots\dots \\ t_N^{ToF} &= T_0 + \frac{L_N}{c} \frac{\sqrt{p_N^2 + m_N^2}}{p_N} \end{aligned} \quad (4)$$

Here we have $N + 1$ unknown variables m_1, \dots, m_N, T_0 and N equations. This system can be solved by loop through all

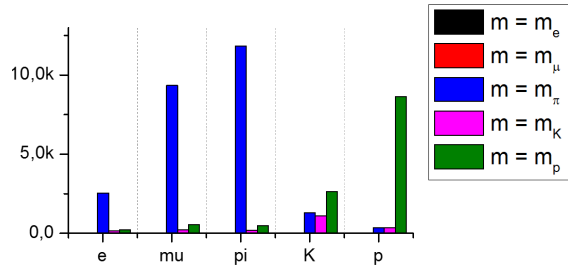


Fig. 5: PID with loop algorithm in PANDAROOT, bar color correspond to Monte Carlo particle type and horizontal axes is reconstructed type

combination of $m_i = [m_e, m_\mu, m_\pi, m_K, m_p]$. For each variant of mass combination T_0 is calculated for all equation and combination when T_0 same for all equations are chooses. Number of combinations for N number of hits are equal 5^N , so this analyze can be done only offline.

Testing of PID algorithm was done using PANDAROOT MC with 1M generated events using DPM generator. Events with number of hits $N < 3$ and particle momentum $p > 4$ GeV/c were rejected. Result of PID algorithm is shown on Fig.5. One can see that is not possible to separate muons and pions due to masses of these particles are close, but pions, kaons and protons are well separated with mismatch probability about 15%.

Calibration of linear optics of COSY using LOCO analysis

C. Weidemann

In order to calibrate and correct linear optics of COSY and thereby overcome present disagreements between the COSY model and the machine a technique called Linear Optics from Closed Orbit (LOCO) [1], originally used at light sources, is favored. For the use at COSY, a hadron storage ring that also operates at non-relativistic energies, the LOCO algorithm was implemented in a newly developed C++ program, which uses MAD-X for optics calculation and ROOT for data analysis and illustration.

The program makes use of the recently implemented automated orbit response matrix (ORM) measurement [2]. The measured ORM is compared to a calculated one, which is based on the existing COSY model and derived using the MAD-X accelerator optics program (see Fig. 1). A typical ORM at COSY contains about 2400 entries, representing the orbit deviations caused by a change in the deflection strength of each of the approximately 40 correction-dipole magnets measured with about 60 beam position monitors (BPMs) (30 horizontal, 30 vertical) along the ring.

A χ^2 -minimization is performed by adjusting different model parameters until both ORMs are equal. The χ^2 is defined as the squared sum of the differences between the model and the measured ORM entries ($M_{\text{mod}}, M_{\text{meas}}$), weighted with the inverse of their measurement errors squared ($\sigma_{M_{\text{meas},ij}}$):

$$\chi^2 = \sum_{i,j} \frac{(M_{\text{mod},ij} - M_{\text{meas},ij})^2}{\sigma_{M_{\text{meas},ij}}^2} = \sum_{k=i,j} E_k^2. \quad (1)$$

The indices i and j denote the BPM and the steerer magnet, respectively. The model parameters under investigation so far are listed in Tab. 1. More detailed information about the LOCO algorithm can be found in [3].

The program was carefully benchmarked with regard to the reconstruction of the listed machine parameters and its sensitivity to different boundary conditions, such as for instance

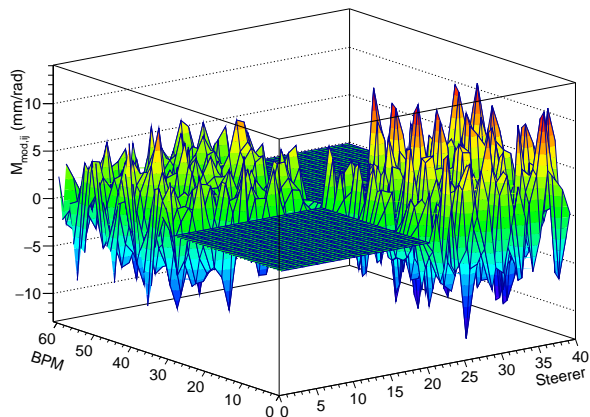


Fig. 1: Calculated orbit response matrix of COSY. Horizontal steerer magnets (0-20) cause orbit responses in the horizontal plane (BPMs 30-60) but not in the vertical plane (BPMs 0-30). The opposite is true for the vertical steerer magnets (20-40). Consequently, this idealized case does not comprise phase space coupling.

Table 1: Machine parameters under investigation.

Parameter name	Number
BPM calibration	60
BPM roll (ψ), shift (s)	2 · 60
Steerer calibration	40
Steerer roll (ψ), position (s)	2 · 40
Deflection angle (offset)	40
Gradient of quadrupole families	14
Gradient of individual quadrupoles	56
Quadrupole rotations (ϕ , θ , ψ) and misalignments (x , y , s)	6 · 56
Dipole rotations (ϕ , θ , ψ) and misalignments (x , y , s)	6 · 24
Quadrupole coefficient of dipoles (K1)	24
Sextupole coefficient of dipoles (K2)	24
Sextupole coefficient of quadrupoles (K2)	56

the BPM resolution and the sequence of reconstruction [3]. The benchmarking made use of reference ORMs, which have been derived based on randomly generated machine parameters.

After completion of the benchmarking procedure the program was tested with measured data. Therefore, a set of orbit response matrices, with only changed quadrupole gradients, was recorded in a dedicated beam time in November 2015. In addition, the dispersion and the working points were measured. The goal of the LOCO analysis is the detection of the applied quadrupole gradient changes and subsequently an improved reconstruction of the betatron tunes, which so far had to be calibrated empirically.

The analyzed data set contains two ORMs, where the only difference is the gradient of quadrupole family number three in the straight section (MQT3), which was modified by 4%. Firstly, the data was analyzed multiple times with regard to the BPM and steerer calibration factors. The averaged result for the beam position monitors is displayed in Figure 2. The corresponding errors are derived from the fluctuation of the results of the individual analyses. A brief look already

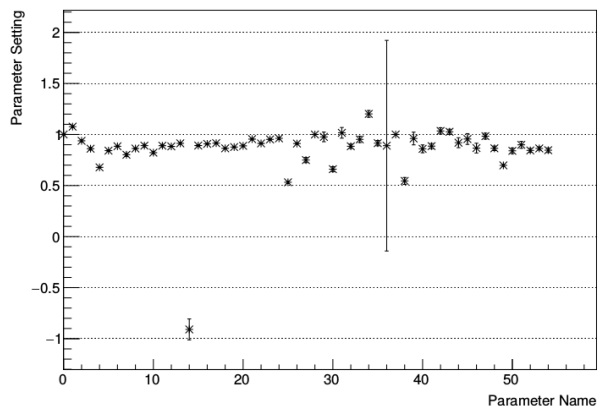


Fig. 2: Reconstruction of BPM gain factors including the detection of a wrongly cabled BPM (number 14).

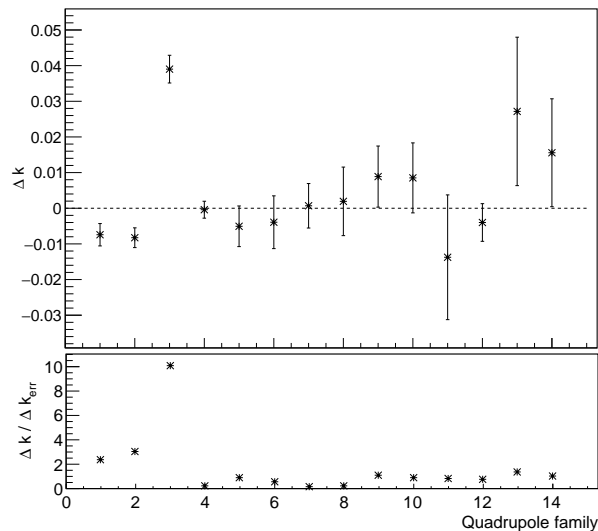


Fig. 3: Change of the quadrupole gradient Δk for all 14 quadrupole families (top panel). The ratio of the determined Δk and it's uncertainty is plotted in the lower panel to allow for an improved judgment of significant changes. As visible, the gradient of family 3 (MQT3) was changed by 4%.

allows the detection of a wrongly oriented BPM (number 14) distinguishable by a calibration factor of -1. The top panel of Figure 3 shows the determined gradient change Δk and the corresponding uncertainty for all 14 quadrupole families. As visible, family number 3 (MQT3) shows a difference of $(4 \pm 0.15)\%$, as expected. Significant deviations from zero can also be observed for family 13 and 14. Considering the large error bars the values are still in agreement with zero. An explanation for these comparably large differences and errors is a degeneracy effect, which allows to compensate changes of one quadrupole gradient by another one. Executing the LOCO analysis several times thus results in different parameter settings for these families and consequently large errors. Dividing the detected gradient change by the corresponding uncertainty (lower plot in Fig. 3) enables a clear identification of significant changes. This is only the case for MQT3 and thus agrees with the applied modifications.

Finally, the machine parameters determined by LOCO are used to calibrate the model, which is then again utilized to calculate the working point. In Fig. 4 the working point calculated by the initial model Q_{model} (red dot) is in clear discrepancy from the measured tune Q_{measured} (green dot). After applying the corrections to the mentioned machine parameters in the model, the measured working points of the initial setting and the two modified ones ($dk_{QT3} = -20$, $dk_{QT3} = +20$) is perfectly reconstructed (black stars). Current investigations are addressing misalignments of dipole and quadrupole magnets. A recent survey measurement indicated misalignments of up to several mm for a small number of elements. Whether the LOCO program is capable of detecting these misalignments is an exciting question. It might also help to judge by how much an improved beam position measurement or a larger number of measurement points can improve the determination of these parameters.

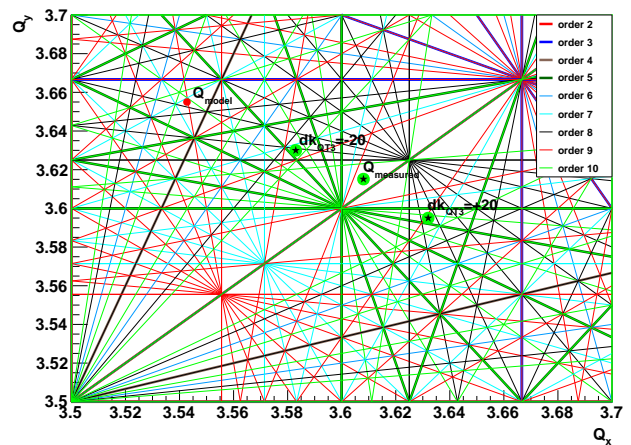


Fig. 4: Reconstruction of the measured working points Q_{measured} (green) for three different quadrupole settings using the LOCO algorithm. In red the working point of the uncorrected model Q_{model} is shown and the black stars indicate the tunes after applying the parameter adjustments determined by LOCO.

References:

- [1] J. Safranek, Nucl. Instrum. Meth. A **388**, 27 (1997).
- [2] F. Hinder *et al.* Annual report 2015: "Automation of the Orbit Response Matrix Measurement at COSY".
- [3] C. Weidemann, M. Bai, F. Hinder and B. Lorentz, doi:10.18429/JACoW-IPAC2016-THPMB009